# CHAPTER 3

## Update on Global Ozone: Past, Present, and Future

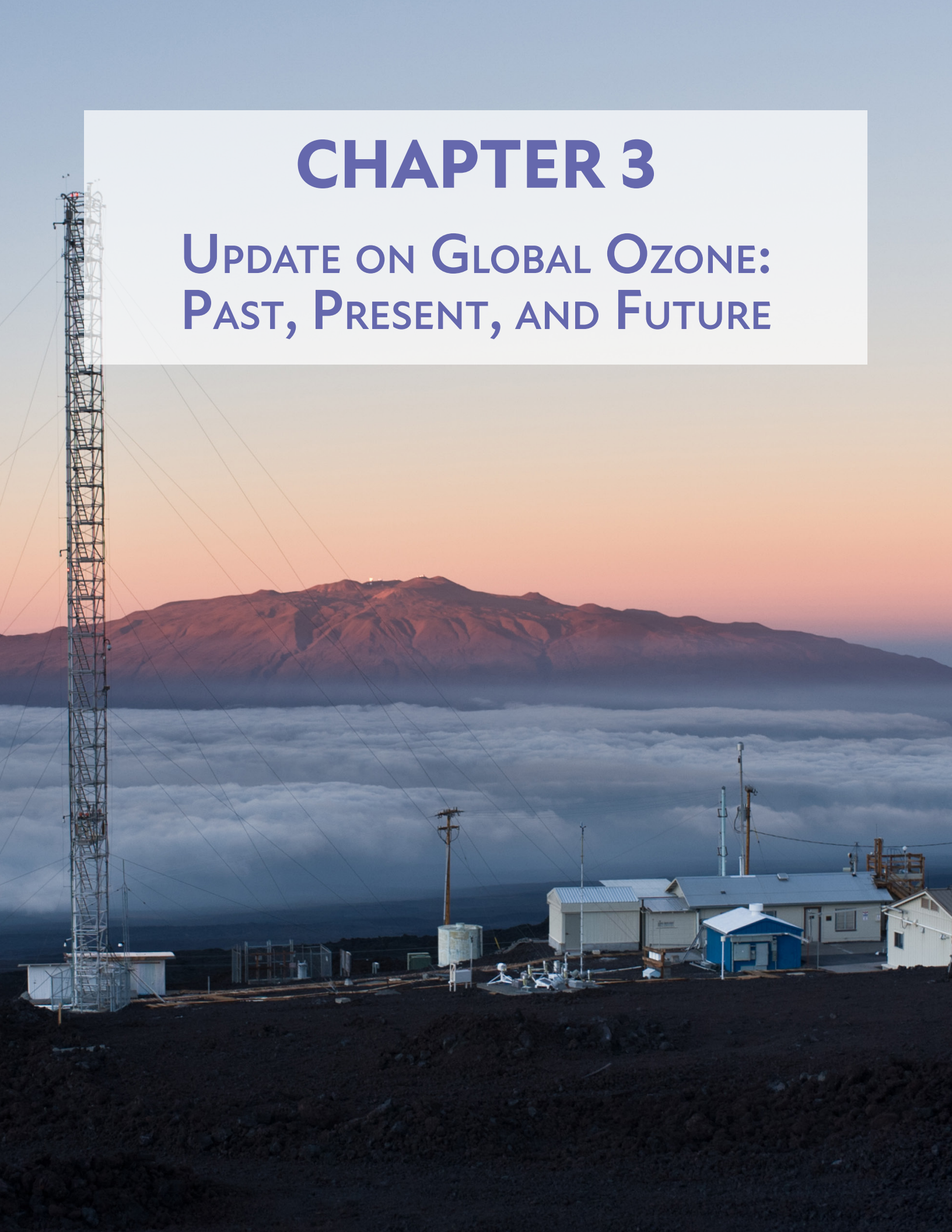

*About the cover image:*
*The Mauna Loa Observatory in Hawai'i is a principal remote site for monitoring changes in atmospheric composition that affect both ozone depletion and climate change.*

*Photo credit: Jonathan Kingston*

# CHAPTER 3

## Update on Global Ozone: Past, Present, and Future


**Lead Authors :** Birgit Hassler
Paul J. Young

**Coauthors :** William T. Ball
Robert Damadeo
James Keeble
Elaine Maillard Barras
Viktoria Sofieva
Guang Zeng

**Contributing Authors :** Matt Amos
Niramson Azouz
Melanie Coldewey-Egbers
Lawrence Coy
Simone Dietmüller
Sandip S. Dhomse
Sophie Godin-Beekman
Daan Hubert
Mahesh Kovilakam
Paul A. Newman
Clara Orbe
Irina Petropavlovskikh
William J. Randel
Wolfgang Steinbrecht
Monika E. Szeląg
Kleareti Tourpali
Corinne Vigouroux
Mark Weber

**Review Editors :** Jessica Neu
Wolfgang Steinbrecht

## Errata (February 2023)

### Chapter 3, Appendix 3A, Table 3A-3:

- The entry for SBUV NASA (MOD) was corrected from S-NPP OMPS NP NOAA v2.8 to S-NPP OMPS NP NASA v2.8.
- The entry for SBUV NOAA (COH) was corrected from S-NPP OMPS NP NASA v2.6 to S-NPP OMPS NP NOAA v3r2.

# CONTENTS

## Chapter 3: Update on Global Ozone: Past, Present, and Future

# SCIENTIFIC SUMMARY

*This chapter presents our current understanding of global ozone outside of the polar regions. The increase of ozone-depleting substance (ODS) concentrations caused the large ozone decline observed from the early satellite era (circa 1980) to the mid-1990s. Since the late 1990s, concentrations of ODSs have been declining due to the successful implementation of the Montreal Protocol and its Amendments and adjustments. Since the last Assessment, the longer observational records show a small increase in near-global total column ozone (TCO) with reduced uncertainty, but this trend is not yet statistically significant. A small increase in TCO is seen in the Southern Hemisphere (SH) mid-latitudes but not yet in the Northern Hemisphere (NH) mid-latitudes or tropics. Different processes operating at different altitudes complicate the attribution of the overall total column trend. However, a significant increase in upper-stratospheric ozone noted in the previous Assessment continues, driven by declines in ozone-depleting substances and increases in greenhouse gases (GHGs). Model simulations support our overall understanding of these trends.*

*Over this century, we expect an increase in global stratospheric ozone as the concentrations of ODSs decline. The future evolution for different latitudes and vertical levels depends on the future concentrations of GHGs and precursors of tropospheric ozone. These other influences may lead to TCO levels that remain below 1980 values in some regions, even after concentrations of ODSs have declined to pre-1980 levels.*

## Changes to date in total column ozone

- **Aggregated ground- and space-based observations indicate an increase of 0.3% decade$^{-1}$ (with a 2-sigma uncertainty of at least ±0.3% decade$^{-1}$) in near-global (60°S–60°N) TCO over the 1996–2020 period.** This trend is consistent with model simulations and our scientific understanding of the processes controlling ozone.
- Over the same 1996–2020 period, the TCO trends in broad latitude bands are as follows:
  - SH mid-latitude (60–35°S) TCO has increased (0.8 ± 0.7% decade$^{-1}$).
  - NH mid-latitude (35–60°N) TCO trends are negligible (0.0 ± 0.7% decade$^{-1}$).
  - Tropical (20°S–20°N) TCO shows no clear trend (0.2 ± 0.3% decade$^{-1}$), likely because stratospheric ozone is decreasing while tropospheric ozone is increasing, both unrelated to changes in ODSs.

  The latitudinal pattern of these TCO trends is largely consistent with our scientific understanding and is reproduced in the latest set of chemistry-climate models (CCMs).
- Present-day (2017–2020) TCO as measured from space-based and ground-based observations remains lower than the 1964–1980 average by
  - about 2% for the near-global average (60°S–60°N),
  - about 4% in the NH mid-latitudes (35–60°N),
  - about 5% in the SH mid-latitudes (35–60°S), and
  - about 1% in the tropics (20°S–20°N).

  Within uncertainties associated with natural variability and instrumental accuracy, these values are essentially the same as given in the previous Assessment for the 2014–2017 average.

## Changes to date in vertically resolved ozone

*Vertically resolved trends are very similar to those given in the last Assessment. However, with longer records and updated merged datasets, recovery trends are now statistically significant in more locations.*

- **Measurements show unambiguous increases in upper-stratospheric ozone for 2000–2020.** Positive trends have a range of ~1.5–2.2% decade$^{-1}$ at mid-latitudes in both the Northern and Southern Hemispheres and ~1–1.5% decade$^{-1}$ in the tropics.
- **Upper stratospheric ozone increases are due to a combination of decreases in ODSs and decreases in stratospheric temperature driven by increases in carbon dioxide ($CO_2$).** New CCM simulations affirm this finding from the last Assessment.
- **There are multiple lines of evidence from both observations and models for a small though uncertain decrease (1–2% decade$^{-1}$, with uncertainty up to ±5% decade$^{-1}$) in tropical lower stratospheric ozone over 2000–2020.** This decrease is consistent with climate change–driven acceleration of the large-scale circulation and has a small impact on TCO. Chemical ozone loss from chlorine and bromine is comparatively minor in the tropical lower stratosphere.
- **Observations suggest small decreases in lower stratospheric ozone in the mid-latitudes of both hemispheres for 2000–2020, while chemistry-climate model simulations suggest small increases.** Ozone in mid-latitudes has large year-to-year variability; thus, trends have large uncertainties, and they are not robust across all datasets and models. The observed decrease is more evident in the Northern Hemisphere.
- **Attribution of TCO trends during the period of slow ODS decline requires knowledge of changes in ozone in both the troposphere and stratosphere.** For instance, there is evidence that the lack of a change in TCO in the tropics reflects an increase in tropospheric ozone that compensates for the ozone decrease in the tropical lower stratosphere. This decrease, due to a climate change–driven acceleration of the large-scale circulation, is expected based on modeling studies. Depletion due to ODSs, on the other hand, is very minor in the tropical lower stratosphere. Nevertheless, analyses of

these changes using different observational datasets indicate significant remaining uncertainty.

## Future ozone changes

*Projections of future stratospheric ozone are available from new model simulations that follow new emissions scenarios: the shared socioeconomic pathways (SSPs). These scenarios all assume compliance with the Montreal Protocol and its Amendments and adjustments for ODSs but span a wider range in future GHG and pollutant emissions pathways than the scenarios used in the previous Assessment, although there are fewer models from which to draw results. As in the last Assessment, the key drivers of future stratospheric ozone levels continue to be declining ODS concentrations coupled with $CO_2$-driven cooling in the upper stratosphere and a strengthening of the Brewer-Dobson circulation. TCO will also be affected by changes in the tropospheric ozone burden.*

- **New estimates for the year of return of near-global TCO to its 1980 value are broadly consistent with the last Assessment. Also similar to the last Assessment, these modeled return dates vary considerably depending on the assumed future scenario.** TCO returns to its 1980 value sooner for scenarios that assume larger emissions of GHGs than scenarios with smaller GHG emissions. The return dates for a middle-of-the-road (SSP2-4.5) scenario are:
  - around 2040 for near global mean (60°S–60°N) annually averaged column ozone;
  - around 2045 for SH (60–35°S) annually averaged column ozone; and
  - around 2035 for NH (35–60°N) annually averaged column ozone.
- **For scenarios that assume strong reductions in the emission of tropospheric ozone precursors, the resulting reductions in tropospheric ozone can be important for TCO trends.** Under such scenarios, TCO in the tropics is projected to remain below the 1980 values until at least 2100. As discussed in the last Assessment, tropical TCO under high GHG scenarios will be below 1980 values at 2100 due to circulation-driven changes affecting lower stratospheric ozone.
- **Future ozone recovery and the expected strengthening of the Brewer–Dobson circulation will most likely increase the proportion of ozone of stratospheric origin in the troposphere.** A new analysis has quantified the contribution of stratosphere-to-troposphere transport of ozone in models under scenarios with limited GHG mitigation (RCP6.0 and RCP8.5). While stratosphere-to-troposphere transport remains highly variable between models and is strongly scenario-dependent, the projected increase is robust, suggesting increases of stratospheric ozone in the troposphere of 10–50% over the 21st century, depending on the model and scenario. Nonetheless, in situ chemistry involving air pollutants remains the largest production term for the simulated tropospheric ozone budget.
- The unreported production of CFC-11 over 2012–2019 (see *Chapter 1*) is estimated to delay global TCO recovery to 1980 levels by ~1 year.

## Emerging Issues

- **Exceptional events can temporarily perturb chemical and dynamical processes that affect stratospheric ozone amounts.** Since the last Assessment, these include the 2019/2020 wildfires in Australia, the eruption of the Hunga Tonga-Hunga Ha'apai volcano, and disruptions to the quasi-biennial oscillation of the tropical winds. In particular, intense wildfires have become more frequent. Their potential impacts on the stratosphere are not yet well quantified and are a subject of active research.
- **The impending loss of vertically resolved, global space-borne measurements of ozone-related atmospheric constituents (e.g., reactive chlorine, water vapor, and long-lived transport tracers) will impede the ability to monitor and explain changes in the stratospheric ozone layer in the future**

## 3.1 INTRODUCTION

This chapter assesses our current knowledge and understanding of past and potential future changes in near-global (60°S–60°N) ozone, updating the corresponding chapter from the previous Assessment (Braesicke, Neu et al., 2018). Our current state of knowledge regarding past-to-present ozone changes and trends is assessed, including attribution, confidence, and uncertainty regarding the drivers of the changes and trends, both from statistical modeling approaches and comprehensive chemistry-climate models (CCMs). The chapter also describes how ozone is expected to change in the future, given scenarios for emissions of greenhouse gases (GHGs), air pollutants and ozone-depleting substances (ODSs), which will affect the composition, chemistry, and climate of the atmosphere. As in past assessments, the key benchmark is ozone's return to its mean value at the reference time of 1980, near the beginning of observed ozone loss.

### 3.1.1 Summary of Findings from the Previous Ozone Assessment

The 2018 Assessment (Braesicke, Neu et al., 2018) examined the evidence for ozone recovery, drawing on updated statistical methods with more rigorous treatment of uncertainties. Evidence for significant ozone increases of 1–3% decade$^{-1}$ was reported for the upper stratosphere (35–45 km), with the most robust trends in the Northern Hemisphere mid-latitudes. Simulations from CCMs attributed approximately half of this trend to the reductions in emissions of ODSs under the Montreal Protocol, with the other half coming from slowing of gas-phase chemistry caused by GHG-induced cooling. A reported decrease in lower-stratospheric ozone, particularly in the tropics, was found to be sensitive to the ozone dataset analyzed and the start and end years of the analyzed period. CCM simulations supported the hypothesis that any apparent trend was linked to dynamical variability. Small increases (0.3–1.2% decade$^{-1}$) in the near-global total ozone column were reported, although these were not statistically significant, given the uncertainties in the data and the large year-to-year dynamical variability (up to 5%). The importance of accurately quantifying tropospheric ozone changes was highlighted because they can be important for the total column ozone (TCO) trend and they are necessary to establish consistency between total column and profile data.

CCM projections of ozone recovery showed that for a baseline scenario with weak climate change mitigation (RCP6.0), global and Southern Hemisphere (SH) mid-latitude ozone should recover by the middle of the century, while the Northern Hemisphere (NH) mid-latitude ozone would do so by around 2035. With negligible halogen-driven ozone destruction, future projections of the ozone layer were found to be most sensitive to the greenhouse gas scenario: elevated GHG concentrations strengthen the stratospheric overturning circulation and impact ozone chemical loss through stratospheric cooling (see *Chapter 5*). Furthermore, the projected strengthening of the circulation results in scenario-dependent stratospheric ozone decreases in the tropics, while the overall column change also depends on the tropospheric ozone trends. Outside of long-term trends, the last Assessment also described how the slow decline of ODSs means that stratospheric injection of sulfate aerosols (e.g., from a large volcanic eruption) could still result in substantial near-term ozone losses.

### 3.1.2 Major New Developments Since 2018

As with past Assessments, an extended observational record facilitates revisiting the evidence for positive ozone trends, as well as their attribution to declining levels of halogenated ODSs controlled by the Montreal Protocol. In addition to the extended records, several merged, vertically resolved datasets have been updated and/or improved, and new ones developed (*Section 3.1.3* and *Appendix 3A*). Moreover, new statistical approaches have been developed and new model simulations have been conducted, both of which provide new insight on the drivers of recent trends.

The Long-term Ozone Trends and Uncertainties in the Stratosphere (LOTUS) initiative (SPARC/IO3C/GAW, 2019) has left a legacy of robust methods for trend detection and uncertainty calculation, from which this chapter draws heavily. New developments since the last Assessment include extending the methodology to diagnose trends by season, as well as demonstrating the utility of dynamic linear models (DLMs) in detecting trends and quantifying uncertainties. The growing use of advanced data science techniques, such as DLMs, is surveyed in **Box 3-1**. Moreover, new longitudinally resolved datasets of total column and vertically resolved ozone trends facilitate new comparisons and validations of ground-based and remotely sensed measurement data.

New simulations and analyses of CCMs have proceeded along two fronts: 1) coordinated multi-model experiments for hindcasts and future projections and 2) detailed investigations of specific issues, often with a single model. For the former, this chapter mostly makes use of simulations from Phase 6 of the Coupled Model Intercomparison Project (CMIP6; Eyring et al., 2016), covering 1850–2100 and including several future scenarios. However, compared to the Chemistry-Climate Model Initiative Phase 1 (CCMI-1) simulations (Morgenstern et al., 2017) used in the previous Assessment, the CMIP6 experiment does not mandate archiving the same degree of ozone-relevant model output and, moreover, includes fewer models that have a sophisticated treatment of atmospheric chemistry processes. For the more detailed studies, this chapter particularly benefits from new investigations into ozone trends in the upper troposphere and lower stratosphere, which, together with extended observations, enable better understanding of the drivers of the trends in this important region. Finally, several models have performed simulations targeted at quantifying the impact of recent unregulated CFC-11 emissions on the current state and future recovery of the ozone layer (WMO, 2021).

### 3.1.3 Data Sources, Quality, and Methods

The analyses and results presented in this Assessment rely on essentially the same ground-based and satellite ozone datasets as were used for the 2018 Assessment. The data records have been extended, and some of them have been partly or fully revised or reprocessed. An overview of the different data sources with more details about specific updates and revision efforts are given in *Appendix 3A*. Since the last Assessment, two new space-based instruments that measure ozone have been deployed, both launched in 2017: SAGE III on the International Space Station (ISS) and TROPOMI on the Sentinel 5 Precursor. SAGE III/ISS provides vertically resolved profiles using solar and lunar occultation (Szatkowski et al., 1999; Cisewski et al., 2014), while TROPOMI is

## *Box 3-1. Emerging Data Science Methods for Stratospheric Ozone Analysis*

"Data science" is a broad term applied to the "principled extraction of information and knowledge from data" (Provost and Fawcett, 2013) and is a phrase whose use in the environmental sciences has been growing in recent years (e.g., Blair et al., 2019). While data science could be a label to describe statistical methods that have long been a staple for ozone analysis, the term is also used more particularly to refer to the adoption and development of more advanced approaches, including artificial intelligence (AI) and machine learning (ML). These have only recently been exploited in this field, thanks to increasing computational power and the wider availability of codes from the statistical and computer science research communities.

Many of the new approaches employ Bayesian inference. In contrast to frequentist approaches, where probabilities are derived from long-run frequency distributions, Bayesian approaches start with a prior hypothesis, such as for model parameters, whose probabilities are updated as additional information becomes available. This forms the basis of, for instance, dynamic linear modeling (DLM) methods, which have been used to understand ozone trends (*Section 3.2.2*). Bayesian approaches are well suited to data-sparse situations, although as data volume increases, inferences from frequentist and Bayesian analyses tend to converge (**Figure 3-5**).

This box briefly highlights some relevant emerging data science advances in three key areas: 1) creating new merged datasets, 2) emulating complex models, and 3) making better use of model output.

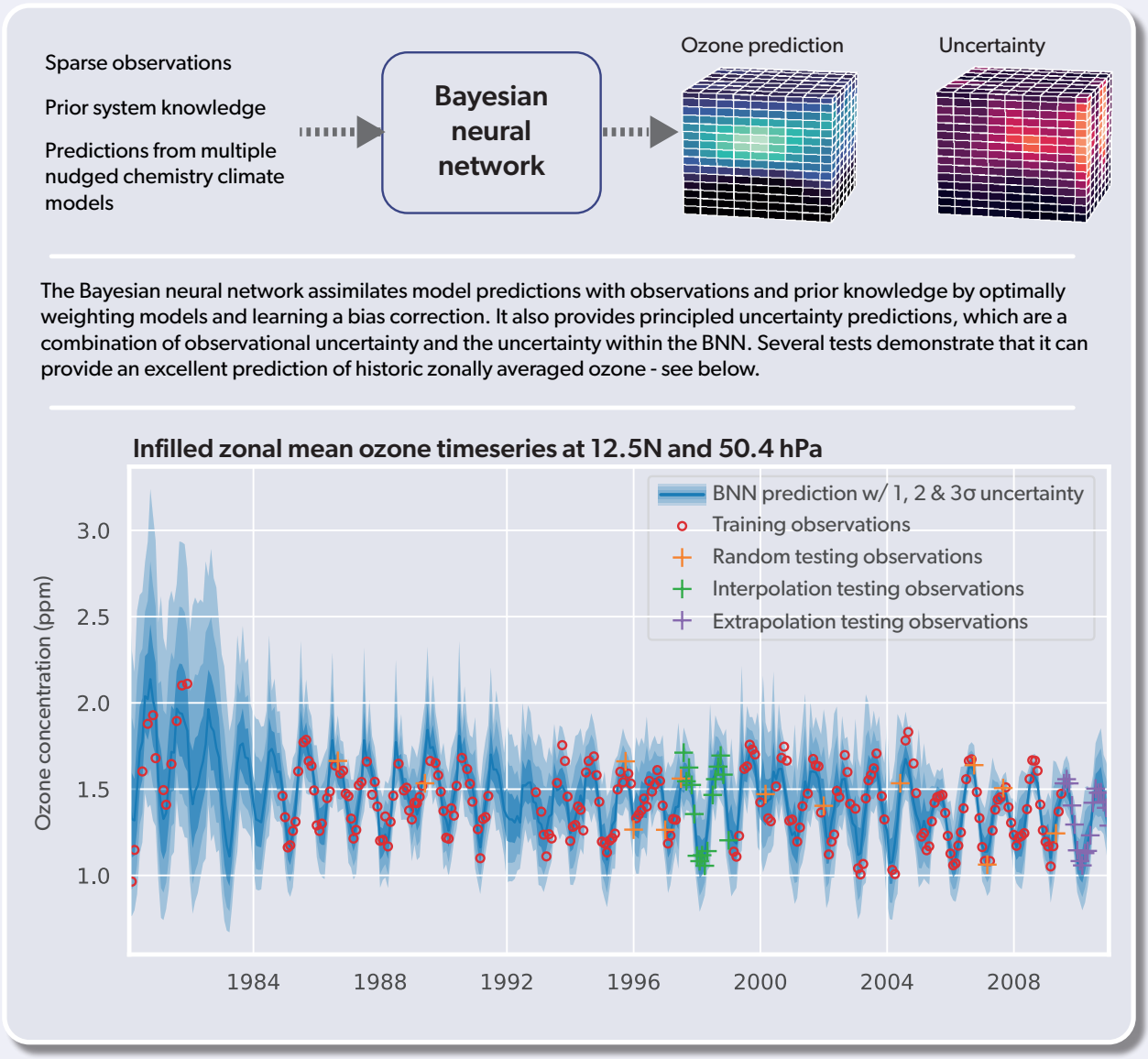


**Box 3.1 Figure 1.** Schematic of the Bayesian neural network (BNN). [Based on Sengupta et al., 2020.]

### *Creating New Datasets: Model-Measurement Fusion*

Statistical techniques have long been employed to join different instrumental records into a complete time series, as well as to spatially and temporally infill sparse datasets, often using multiple linear regression (MLR)-based approaches (e.g., Bodeker et al., 2013; Davis et al., 2016), and now also with more advanced techniques (Loyola and Coldewey-Egbers, 2012; Ball et al., 2017; Bodeker et al., 2020; Dhomse et al., 2021). One different approach is the Bayesian neural network (BNN), which can be used to fuse data from chemistry-climate models (CCMs) and observations (Sengupta et al., 2020). A BNN can learn which weighted combination of CCM data is appropriate to use for a given location and time (rather than using fixed weights) and provide a principled treatment of uncertainty. A schematic of the BNN is given in the **Box 3.1 Figure 1**.

### *Complex Model Emulation*

CCMs are computationally expensive and time consuming to run, which places practical limits on the number of simulations that can be completed. This limits both our exploration of model uncertainty, such as through alternative parameter choices to simulate chemical and physical processes, and the investigation of a wider range of possible future scenarios. One way to address this is to emulate the complex model with a sophisticated but computationally cheaper statistical approach. Approaches include building an emulator by fitting Gaussian processes to a set of carefully chosen calibration simulations, which can then be exploited to explore what would be simulated by the complex model across a multidimensional parameter space (e.g., Revell et al., 2018; Wild et al., 2020). Other studies have emulated CCM output using a variety of ML approaches, which have been used to explore a wide range of future scenarios (Keeble et al., 2021b), or they have proposed the adoption of ML-based algorithms within a CCM to replace more computationally expensive chemistry solvers (Nowack et al., 2018). Nevertheless, application of these newer approaches to stratospheric ozone research is still in its infancy, and CCMs in their current form remain our best tools for analyzing past ozone trends and generating future projections.

#### *Approaches to Make Better Use of Model Output*

Given the same input scenarios for greenhouse gases and ozone-depleting substances, different CCMs simulate a wide range of outputs. While some of this model spread represents irreducible uncertainty due to the chaotic nature of the climate system (which can be approximated as "weather noise"), different models will have varying levels of skill in reproducing reality. Moreover, this variation in simulation skill will likely be a function of, e.g., geographical region and season, atmospheric composition, and the prevailing climate. Different models are also seldom independent (e.g., Knutti et al., 2013). This varying model skill and intermodel commonality means that the commonly used multi-model mean does not provide the best estimate of the past, current, or future state of the atmosphere. Recent approaches have sought to improve on this by providing weighted multi-model means, where model weighting is based on a measure of model independence and the performance of the model when compared to observations (Amos et al., 2020; Sengupta et al., 2020). In the broader climate literature, other studies have developed and exploited "causal networks" for a novel process-based model evaluation (Runge et al., 2019; Nowack et al., 2020). This is a sophisticated data science approach to identify causal links through spatiotemporal correlations in observational data. These can then be examined to produce metrics to evaluate models and understand model-observation and model-model differences.

a nadir sounder that provides total and tropospheric column information as well as vertical profiles (Veefkind et al., 2012). Early validation efforts for both SAGE III/ISS (Wang et al., 2020) and TROPOMI (Hubert et al., 2021; Mettig et al., 2021) suggest the data are well suited to provide valuable information about long-term changes, and these data are already being incorporated into commonly used merged datasets.

Several currently operational spaceborne instruments are well beyond their design lifetimes, and some are scheduled to be decommissioned in the next few years. Instruments whose data have been used as part of this Assessment (see **Tables 3A-3** and **3A-4**) or previous Assessments (see Table 3A-1 of WMO (2014)) that will likely cease operations by the end of the 2026 Ozone Assessment process include the Aura Microwave Limb Sounder (MLS), the SciSat Atmospheric Chemistry Experiment Fourier Transform Spectrometer (ACE-FTS), the Odin Optical Spectrograph and Infrared Imager System (OSIRIS), and the Odin Sub-Millimetre Radiometer (SMR). With the loss of current limb-viewing capabilities, vertically resolved global measurements of many trace gases relevant for stratospheric chemistry and dynamics will no longer be available. These trace gases include reactive (chlorine monoxide, ClO) and reservoir (hydrochloric acid, HCl; chlorine nitrate, $ClONO_2$) chlorine species, water vapor, nitric acid ($HNO_3$), and long-lived transport tracers (e.g., nitrous oxide, $N_2O$; methane, $CH_4$; carbon monoxide, CO; methyl chloride, $CH_3Cl$). The recent Report of the Ozone Research Managers of the Parties to the Vienna Convention (ORM, 2021) identifies the need to "continue limb emission and infrared solar occultation observations from space" that are "necessary for global vertical profiles of many ozone- and climate-related trace gases" as one of the "key systematic observations recommendations." Indeed, the impending cessation of these measurements, many of which have been taken continuously over the last several decades, will hamper the ability to reduce key uncertainties that remain in understanding stratospheric ozone depletion, including the lack of emergence of a clear signature of recovery in the Arctic, the potential influence of volcanic and wildfire emissions, the role of very short-lived substances (VSLSs), and the impact of strengthening of the Brewer-Dobson circulation, among others.

In addition to the multiple merged datasets that were the

basis for most of the long-term, zonally averaged variability and trends discussed in the last Assessment, an additional dataset was created recently: SAGE II-SCIAMACHY-OMPS (Arosio et al., 2019). This includes a slightly different combination of satellite measurements than in previous merged datasets; however, since different merged datasets share underlying data sources, trends calculated using these datasets are not independent. Also, since the last Assessment the community has created new (gridded) latitudinally, longitudinally, and vertically resolved ozone datasets: an expanded version of the SAGE II-SCIAMACHY-OMPS dataset (Arosio et al., 2019) and MEGRIDOP (Sofieva et al., 2021). So far, only a few merged datasets provide gridded ozone profiles, which allow more detailed analyses of spatially and vertically resolved trends.

Data quality remains one of the key drivers of trend uncertainties, and specific topics, such as instrument drifts, biases, and sampling, were discussed in detail in the last Assessment. Considerable effort has since been made to improve individual instrument records as well as merged datasets. For example, ground-based vertical profile records were improved through homogenization of ozone soundings in the framework of the Tropospheric Ozone Assessment Report Phase 2 (TOAR II) project, homogenization of Umkehr and lidar records, and reprocessing of Dobson, Brewer, and FTIR records (see *Appendix 3A*). Satellite measurements have been improved by updating retrieval algorithms and by enhancing the consistency and stability between individual datasets. These advances in data quality, and the additional four years of data, have led to a more consistent picture of trends derived from ground-based and satellite measurements since the last Assessment. In addition to data quality, the methodology used to determine trends can also affect the resulting uncertainties. Not much has changed with respect to the most commonly applied multi-linear regression models for trend detection since the last Assessment, but alternative statistical models (e.g., dynamic linear models) are seeing greater use by the community and provide a robust alternative method of trend detection.

With the publication of the SPARC Reanalysis Intercomparison Project Report (SPARC, 2022), a comprehensive evaluation and intercomparison of meteorological reanalyses is now available, complete with recommendations on how to best use reanalysis data for long-term trend and variability analyses. For this reason, **Box 3-2** provides a discussion about the usability of reanalyses to calculate reliable ozone trends. However, the recommended practices have not yet been widely adopted by the community, and therefore trend studies based on reanalysis data are again not highlighted in this Assessment.

## 3.2 NATURAL VARIATION AND TREND MODELS

Ozone varies on seasonal, interannual, and decadal timescales as a result of both natural and anthropogenic forcing. Careful determination of long-term trends requires accurately attributing the other major sources of variability. The most common method of quantifying the trends is through statistical techniques involving linear regression (WMO, 2018; SPARC/IO3C/GAW, 2019, and references therein). Various regression techniques adopt different statistical approaches to evaluate trends and their uncertainties. Two common approaches in ozone analysis are multiple linear regression (MLR) and dynamic linear models (DLMs). The application of these linear regression techniques assumes that ozone is linearly dependent on predictor time series (or proxies) that dictate how it varies with time. The following sections present the different sources of variability and their proxies (*Section 3.2.1*), the different methodologies applied to calculate long-term ozone trends (*Section 3.2.2*), and (briefly) how significance is assigned to the calculated trends (*Section 3.2.3*).

### 3.2.1 Natural Variability

The primary influences on the global distribution of ozone are sunlight, chemistry, and transport of either ozone itself or any reactive species important for ozone chemistry. The proxies that describe these sources of variability are often empirical, rather than having a simple functional form, and are often not completely independent, as the processes can interact with each other or simply have similarities in their temporal dependence. This lack of

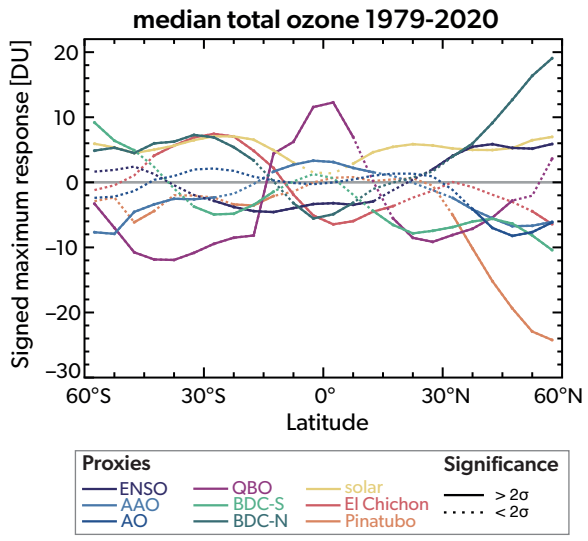


**Figure 3-1.** Maximum contribution of different sources of natural variability (as proxies) in a multiple linear regression analysis applied to the median of five TCO datasets as a function of latitude (Weber et al., 2022). Each colored line shows the response (i.e., deviation in Dobson units, or DU) of ozone resulting from a different proxy in the regression (see legend), with the sign indicating whether the ozone response is positively or negatively correlated with the proxy. A solid line indicates that the response to a given proxy is significant at the 5% level, whereas a dashed line indicates that it is not significant at the 5% level. [Adapted from Weber et al., 2022.]

## *Box 3-2. Can Reanalyses Be Used to Calculate Robust Ozone Trends?*

Diverse methods are used to create ozone datasets from different sources or to fill gaps in existing datasets, including merging observations with simulated data. One of the goals is to provide ozone datasets suitable for trend analyses. Merging techniques are updated and further developed. Lately, machine learning techniques have also been applied to datasets with sporadic coverage (see **Box 3-1**). Reanalysis, which integrates physics-based prognostic meteorological models with observational data in an iterative way, is another approach. Both one-directional coupling (meteorology modifying prognostic ozone fields) and bi-directional coupling (ozone fields also modifying meteorological fields via radiation) are applied in reanalyses. As such, ozone estimates from reanalyses depend on both continued high-quality observations and the skill and accuracy of the underlying forecasting model.

In almost all current reanalysis systems, ozone is included as a prognostic variable. How well the ozone fields and their variability are represented in the different reanalyses depends on the assimilated observations and the chemical and microphysical model parametrizations. Primarily, total column ozone observations or measurements of broad vertically weighted averages are assimilated, but more recent reanalyses also assimilate observations with a higher vertical resolution (Davis et al., 2017). Problems for ozone trend analyses based on reanalysis data occur when the different assimilated data contain internal drifts or steplike changes (Wargan et al., 2020) and/or biases between the datasets (Wargan et al., 2018). Approaches to account for internal drifts and biases exist (van der A et al., 2010, 2015) but have so far not been widely applied. Additionally, assimilation of radiances and other parameters might introduce step changes in stratospheric temperatures and wind fields that directly influence the estimated ozone distribution (Stauffer et al., 2019), and inhomogeneities and discontinuities can be introduced by a changing number of assimilated datasets over time (Sterl, 2004; Simmons et al., 2014; Shangguan et al., 2019).

For these reasons, there has been reluctance to use ozone from reanalysis datasets for trend studies despite successful use in ozone-related process studies (e.g., Banerjee et al., 2020; Orr et al., 2021). Recent developments in data assimilation methodology do seek to address the continuity issues outlined above. Some reanalyses currently include bias correction or ozone data homogenization algorithms (van der A et al., 2010, 2015; Hersbach et al., 2020; Wargan et al., 2020). Additionally, several recently developed reanalysis products focus specifically on atmospheric composition and use sophisticated chemistry models that help correctly propagate observational data in space and time by providing stable priors for data assimilation (Flemming et al., 2017; Errera et al., 2019; Inness et al., 2019a, 2019b; Huijnen et al., 2020).

There is, therefore, a tension between some clear advantages that reanalyses provide for studies of long-term trends and variability, and current limitations. The SPARC Reanalysis Intercomparison Project (S-RIP) has made substantial progress in providing advice to users and feedback to reanalysis centers. The S-RIP report (SPARC, 2022) provides a comprehensive evaluation and intercomparison of 12 major meteorological reanalyses with a focus on the representation of stratospheric processes and assimilated fields, including ozone. An overview of the skill level demonstrated in different reanalysis datasets for different metrics of ozone trends and variability, as analyzed with S-RIP, is shown in **Box 3-2 Figure 1**. Several recommendations emerged from this evaluation: 1) trends from reanalyses should be treated with caution; 2) an understanding of the reanalysis systems is necessary for interpretation; 3) studies should use multiple reanalyses and, where possible, other data to help assess result robustness and estimate uncertainties; and 4) the use of several specific, now-outdated reanalyses is discouraged.

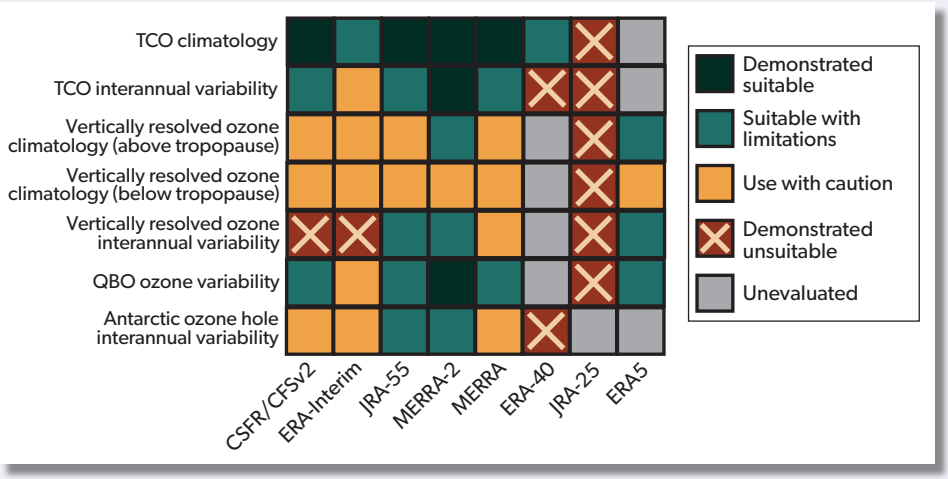


**Box 3.2 Figure 1.** Overview of analyzed ozone diagnostics with a variety of recent and commonly used meteorological reanalysis data, with recommendations on where the data can be used most appropriately. [Adapted from Davis, Hegglin et al., 2021, in SPARC, 2022.]

orthogonality between the proxies can sometimes make it difficult to attribute variability in ozone directly to one source or another. Furthermore, since the 2018 Assessment, new behavior has been observed that raises questions about the suitability of some of the proxies that are typically used, with concerns regarding how well they represent the actual variability of ozone. **Table 3A-1** lists the sources of data for different proxies, while **Figure 3-1** illustrates a comparison of the relative impact that some of the different sources of variability described here have on total column ozone (TCO) as a function of latitude.

### *3.2.1.1 The Quasi-Biennial Oscillation (QBO)*

The Quasi-Biennial Oscillation (QBO) is a pattern of alternating zonal winds in the tropical stratosphere that affects ozone through transport and chemistry. It is characterized by an oscillating pattern of easterly and westerly winds in the stratosphere, with a variable (24–32 month) period over which it progressively descends through the stratosphere (**Figure 3-2a**). These oscillating wind shear patterns induce oscillating vertical motions in both the tropics and extratropics that are opposite in direction to each other along with corresponding meridional transport in between (Baldwin et al., 2001). The response of ozone to the QBO is strongest in the tropical lower stratosphere, with secondary maxima in the middle stratosphere in both the tropics and low-latitude (<40°) extratropics (Zawodny and McCormick, 1991).

The QBO is the dominant source of variability of stratospheric ozone in the tropics, particularly in the lower stratosphere, and it is a modulator of variability at higher latitudes (Anstey and Shepherd, 2014). It is vital that its influence be accurately represented in trend analyses. The vertical and meridional transport and chemical influence of the QBO on ozone are represented using tropical zonal wind data as a proxy. This usually takes one of two forms: a pair of time series of zonal wind measurements from two different pressure levels that are roughly out of phase from each other, or the leading two empirical orthogonal functions (EOFs) derived from this data (Wallace et al., 1993; Randel and Wu, 1996). The latter is preferable since EOFs are explicitly constructed to better represent the variability present in all of the source data. The proxies typically represent over 90% of the QBO's variability but are limited in their ability to fully represent the effect of the QBO on ozone. For example, the seasonal cycle modulates the QBO at higher latitudes (Tung and Yang, 1994), creating a nonlinear effect that must be adequately captured in regression analyses, such as by using seasonal cross-terms in the regression (Randel and Wu, 1996; Damadeo et al., 2014). Not accounting for this can make trend analyses particularly sensitive to the endpoints (Ball et al., 2019a).

The typical pattern of the QBO has been fairly stable and repeatable over the first six decades of observations of tropical zonal winds, which started in the early 1950s. The last Assessment highlighted the first-ever disruption to the QBO in 2015/16 (Newman et al., 2016; Osprey et al., 2016; Tweedy et al., 2017), and since then another disruption happened in 2019/20 (Saunders et al., 2020; Anstey et al., 2021), as illustrated in **Figure 3-2a**. In both cases, large horizontal momentum fluxes originating from the extratropics propagated to the tropics, where they interfered with the normal momentum transfer associated with the QBO (Coy et al., 2017; Lin et al., 2019; Saunders et al., 2020; Anstey et al., 2021). This resulted in the introduction of westward winds at around 40 hPa (~35 km) during the eastward phase and lifting of the eastward winds. The changing wind shear patterns associated with these disruptions drove correlated changes in stratospheric ozone resulting from changes in upwelling. While the impacts were similar in the two cases, the origin of each disruption was different. The 2015/16 disruption was caused by the coincidence of a particularly strong El Niño event in the Northern Hemisphere (Coy et al., 2017; Lin et al., 2019), while the 2019/20 event was the result of strong wave forcing from the Southern Hemisphere in the absence of any El Niño event (Saunders et al., 2020; Anstey et al., 2021).

These disruptions present an additional challenge as to the representativeness of the QBO proxies used in regression analyses. During such disruptions, the amount of QBO variance explained by the two leading EOFs is substantially reduced and higher-order EOFs are necessary to fully capture the variability (**Figure 3-2b**). It has not yet been determined if these higher-order EOFs can adequately capture the correlated variability in ozone during the disruptions. In addition, while these were unprecedented in the observational record, they may not be isolated incidents. Accounting for QBO disruptions may become necessary for both current and future trend analyses.

### *3.2.1.2 El Niño-Southern Oscillation (ENSO)*

The El Niño-Southern Oscillation (ENSO) is a pattern of alternating warm and cold sea surface temperatures (SSTs) of the tropical eastern and western Pacific Ocean, which influence tropospheric circulation and stratosphere-troposphere exchange. Warmer El Niño phases increase tropical upwelling, resulting in negative ozone anomalies in the tropical upper troposphere/lower stratosphere (UTLS), whereas colder La Niña phases decrease tropical upwelling and result in positive ozone anomalies (Domeisen et al., 2019); ozone anomalies also occur at mid-latitudes, which may differ separately by hemisphere with the ENSO phase (Ziemke et al., 2010; Oman et al., 2013). Ultimately, ENSO can substantially affect stratospheric circulation as a whole by influencing other transport mechanisms such as the QBO or the Brewer-Dobson circulation (BDC; Domeisen et al., 2019, and references therein). For example, the QBO propagates downward more rapidly during an El Niño phase, and El Niño leads to a strengthened BDC associated with tropical stratospheric cooling, warmer poles (Randel et al., 2009), and weaker stratospheric polar vortex (Ermakova et al., 2019). These interconnections make ENSO an important process controlling the interannual variations of stratospheric ozone but complicate any regression analyses that assume all proxies are orthogonal to each other.

The ENSO-related proxies used for long-term trend analyses are computed as an index that is derived from a number of possible oceanic and/or atmospheric parameters (Domeisen et al., 2019). Among them are the Niño 3.4 Index, which derives directly from a time series of Pacific SST anomalies over a region in the tropical Pacific (Huang et al., 2017), and the multivariate ENSO index (MEI), computed from a principal component analysis of SSTs, surface air temperatures, sea level pressures, surface winds, and radiation over the tropical Pacific (Wolter and Timlin, 1998). These simple indices may capture the general ENSO pattern that correlates with ozone variability but do not account for the more subtle impacts of ENSO on circulation patterns. Stratospheric ozone anomalies and large SST anomalies are found not only during El Niño and La Niña but also during the transition phases (Lin and Qian, 2019). However, sometimes SST anomalies are not

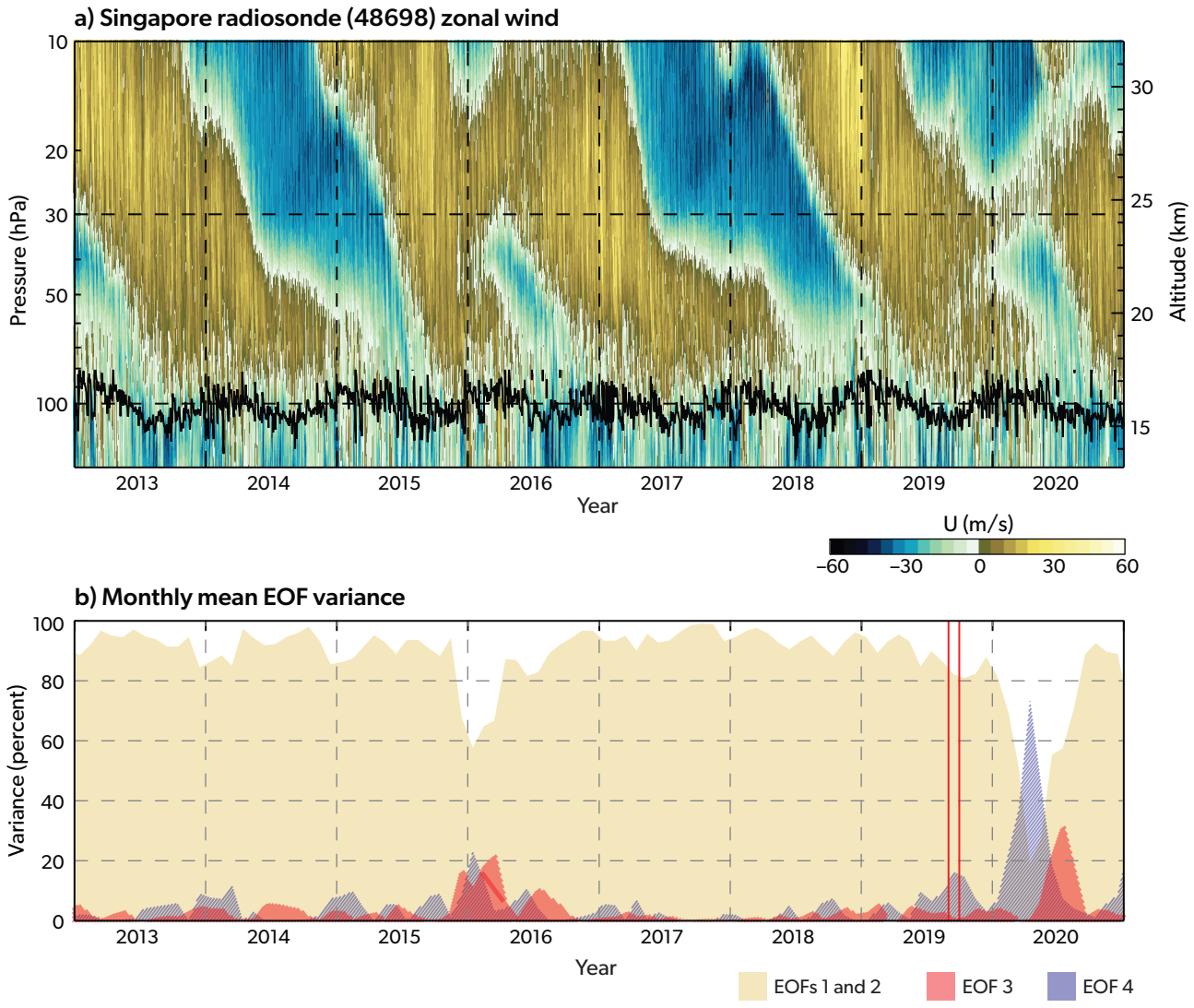


**Figure 3-2.** (a) Zonal winds observed from radiosondes at Singapore (blue to gold shading) and the lapse-rate tropopause (black line). Disruptions in the zonal winds are noticeable by the ascending gold shading above 40 hPa in 2016 and 2020 that breaks the descending blue shading. (b) Amount of variance explained over time by the first two EOFs (light orange shading), the third EOF (dark orange), and the fourth EOF (blue), computed from the Singapore wind data excluding the two disruptions. Typically, 80% or more of the QBO variability can be represented by the leading two EOFs, but the disruptions illustrate that additional EOFs are required to adequately capture the variability during these time periods. The two vertical red lines bracket September 2019. [Adapted from Anstey et al., 2021.]

accompanied by corresponding atmospheric anomalies; these events are called uncoupled El Niño warming (Hu et al., 2020).

The potential disconnect between an ENSO proxy and ozone anomalies exists in part because ENSO's influence is the by-product of the propagation of highly regionalized effects to the rest of the atmosphere. Moreover, the remote impacts depend on the location and intensity of ENSO events. The SST anomalies are not always simply warm or cold in the eastern Pacific ("canonical ENSO") but are sometimes warm in the Central Pacific ("ENSO Modoki"; Ashok et al., 2007) or even double-peaked with warm centers in both regions (Shin et al., 2021). These subtle differences can result in noticeable changes in stratospheric ozone. For example, the warm phase of canonical ENSO has been found to be associated with negative ozone anomalies in the SH lower stratosphere and positive ozone anomalies in the NH lower stratosphere, while the warm phase of ENSO Modoki results in the opposite (Lu et al., 2019).

Both the simplicity of the ENSO proxy and the way it is implemented can affect long-term trend analyses. ENSO indices are a single time series, meaning they cannot alone account for any lag in the response. The response of stratospheric ozone to the phase of an ENSO index derived from tropospheric data is often delayed by several months, with the strongest anomaly appearing in the NH winter one year after El Niño (Lin and Qian, 2019). Another aspect of trend analysis implementation is the spatial coordinate system of the ozone data. For instance, when ozone is gridded

with respect to the location of the subtropical jet, its variability in the UTLS shows a stronger correlation with ENSO variability than if it was analyzed in the usual latitude/longitude/altitude coordinate system, although this is still an active area of study (Olsen et al., 2019). Including the QBO in the analysis shows that ENSO generally dominates ozone variability around the subtropical jet, while the magnitudes of the QBO and ENSO impacts are more comparable at mid-latitudes.

### 3.2.1.3 Aerosols

The term "aerosols," which is strictly defined as fine particles suspended in a gas, is essentially a catch-all term for everything in the atmosphere that is not a gas or cloud, although the focus is generally on the particle component. Aerosols exhibit many different compositions and originate from a variety of natural and anthropogenic sources (Kremser et al., 2016, and references therein), but the most common form of aerosol in the stratosphere is an aqueous suspension of sulfuric acid (Junge et al., 1961). The last Assessment went into detail regarding the sources and impacts of aerosols on ozone. In brief, aerosols affect ozone through two main mechanisms. The first is by offering a surface for heterogeneous chemistry that leads to denitrification and primarily leads to ozone destruction/enhancement in the presence/absence of chlorine. The second is by cooling the Earth's surface and heating the stratosphere, which both alters chemical reaction rates and modifies circulation. The first mechanism is influential at the location of the aerosol, while the second mechanism can have impacts beyond that. (See *Chapter 6* for the potential ozone impacts of stratospheric aerosol from climate interventions.)

Stratospheric aerosol proxies for use with long-term ozone trend analyses are derived from long-term aerosol data records (e.g., Chouza et al., 2020; Kovilakam et al., 2020), which are composed of individual satellite- and ground-based measurements. Since the last Assessment, several of these instrument records have been improved, including OMPS (Chen et al., 2018), OSIRIS (Rieger et al., 2019), and CALIPSO (Kar et al., 2019); a new instrument, SAGE III/ISS (Chen et al., 2020; Wang et al., 2020), has also been deployed, as mentioned in *Section 3.1.3*. These updated and new datasets have been used to generate a more consistent long-term multi-instrument stratospheric aerosol record with version 2.0 of the GloSSAC (Kovilakam et al., 2020). As an improvement over version 1.0 (Thomason et al., 2018), version 2.0 uses the new SAGE III/ISS data to recalibrate the bias correction of OSIRIS and CALIPSO data so that they better align with the native aerosol extinction measurement of SAGE II and SAGE III/ISS for a more consistent multi-decadal record.

While sulfate makes up the majority of stratospheric aerosol, and volcanic eruptions are the primary source, some other sources of stratospheric aerosol include black and brown/organic carbon components, which will impact the properties of the injected aerosol. Normally, carbonaceous aerosols do not make it into the stratosphere in appreciable levels, but the time since the last Assessment has seen the two largest fire-fueled thunderstorms (pyroCbs; see also *Chapter 6*) ever recorded, and both resulted in smoke injection into the stratosphere. These fires were in Canada in 2017 (Bourassa et al., 2019; Kloss et al., 2019; Yu et al., 2019) and Australia in 2020 (Kablick et al., 2020; Khaykin et al., 2020; Schwartz et al., 2020; Yu et al., 2021). Smoke aerosols are typically larger than stratospheric sulfate particles, so they have more surface area to facilitate chemical processes. They also heat the stratosphere more efficiently, particularly black carbon, through absorption of both outgoing infrared and incoming solar radiation. The 2020 Australian wildfires resulted in denoxification typically seen with volcanic eruptions (Solomon et al., 2022) and unprecedented chlorine partitioning (Santee et al., 2022) that cannot be explained by existing sulfate aerosol-based modelling (Strahan et al., 2022), as well as the first major impact to global lower-stratospheric temperature (>0.5 °C) since the 1991 Mount Pinatubo eruption (Rieger et al., 2021; see *Chapters 5* and *6*). At the same time, stratospheric ozone was reduced by 0.1–0.2 ppm throughout the SH mid-latitudes starting several months after the fires, an amount comparable to the impact of the 2015 Calbuco eruption (**Figure 3-3**). However, as a relatively recent occurrence with few published studies, there is still some debate as to how much of this observed low ozone was a result of the smoke injected into the stratosphere (Rieger et al., 2021; Solomon et al., 2022; Bernath et al., 2022) versus expected as a result of transport from unperturbed natural variability (Santee et al., 2022; Strahan et al., 2022).

Differences in the type of aerosol contributing to stratospheric aerosol perturbations can have implications for the nature of the aerosol proxy that is used and how it relates to changes in ozone. For example, aerosol surface area density would correlate quite well to chemistry, but smoke aerosol and sulfate aerosol of the same size would have substantially different radiative impacts. Similarly, smoke and sulfate aerosol can have appreciably different particle size distributions and thus similar aerosol optical depth at one wavelength but very different at another. For ozone trend analyses across periods where smoke aerosol becomes the dominant aerosol influence, this may pose a problem for the usefulness of aerosol proxies that assume stratospheric aerosol is dominated by sulfate. However, the different impact of wildfires may be a problem only when an aerosol proxy is applied to data after the mid- to late 1990s, as the large ozone response to the Mount Pinatubo eruption in late 1991 will dominate any potential erroneous response to much smaller stratospheric aerosol injections that occurred after the early 2000s.

Another example of an atypical stratospheric aerosol injection event are the January 2022 eruptions of the Hunga Tonga-Hunga Ha'apai volcano. These eruptions injected large amounts of water vapor into the stratosphere and are a topic of ongoing research but are expected to have some impact on stratospheric ozone, perhaps unlike that of previous eruptions of similar size (see **Box 5-1**).

### 3.2.1.4 Solar Radiation

Variations in the sun's irradiance affect ozone through photochemical processes in the upper and middle stratosphere, as well as through possible associated dynamical feedbacks (Haigh, 1994; Hood and Soukharev, 2003). Solar fluxes as a function of wavelength (spectral solar irradiance [SSI]) are needed to describe this forcing. Ultraviolet (UV) wavelengths shorter than 242 nm are particularly important as they drive the primary production of ozone from oxygen photolysis. However, direct, stable, long-term UV observations are not available due to the short lifetime of observing satellites and in-flight instrument degradation, making an accurate representation of solar UV changes on decadal timescales a challenge. Solar UV variability is highly correlated with solar radio fluxes in the 10.7 and 30 cm ranges. While both are used, recent analyses indicate that in the context of attribution

studies, the 30 cm radio flux is a better representative of solar UV variability than the 10.7 cm flux (Dudok de Wit et al., 2014; Dudok de Wit and Bruinsma, 2017). Solar energetic particles are also important for stratospheric ozone, and these are discussed in *Chapter 4*.

In the last Assessment, consistency in the estimated effects of solar forcing on ozone over the past decade was low. This was due to different derived responses of ozone to solar variability between different ozone datasets, as well as surprising observations of the 11-year solar cycle, which indicated much larger variability for some UV wavelengths compared to previous observations. Progress has been made in these areas.

Since the previous Assessment, new analyses and corrected ozone datasets have led to closer agreement on the magnitude and location of the ozone response to the solar cycle. The last Assessment reported that the observed ozone/solar cycle response had reduced to ~1% in the upper stratosphere (Dhomse et al., 2016; Maycock et al., 2016), with estimates from SBUV MOD v8.6 mixing ratio data showing a smaller signal than the SAGE II v7.0 number density data. While it was further noted that estimates from number density data (**Figure 3-4a**) were more robust (Ball et al., 2019b), unexplained differences remained. More recent studies now suggest the smaller solar-ozone response from SBUV data is likely a result of a satellite drift (Li et al., 2016; Ball et al., 2019b). Accounting for this, new SBUV and SAGE II-based composites agree that the magnitude of the maximum solar response in the tropics is ~2% (2σ uncertainty of 1%) and occurs at ~7 hPa (35 km; **Figure 3-4b**), although the peak is vertically broad (5–10 hPa or ~32–38 km). This is a lower altitude than in some earlier studies (Soukharev and Hood, 2006; Dhomse et al., 2016; **Figure 3-4a**).

While these results include data from the Aura MLS satellite (operational since 2004), they are also in broad agreement with a recent study that used Aura MLS data alone (Dhomse et al., 2022), factoring in the magnitude of the solar cycle and associated uncertainties. This recent study covers a period (2005–2020) of monotonic changes in equivalent effective stratospheric chlorine (EESC) and few volcanic eruptions that could substantially influence the stratosphere (see *Section 3.2.1.3*). It found an ozone response of ~3% with a single broad peak at ~5 hPa (~38 km) in the tropical stratosphere. A secondary ozone peak in the tropical lower stratosphere, discussed in the previous Assessment and thought to be a dynamical response to the solar cycle, was found to be notably smaller than in previous estimates when considering Aura MLS data alone (Dhomse et al., 2022). These results are robust across several multiple linear regression approaches (see *Section 3.2.2*).

The previous Assessment also reported that, at the time, the latest measurements showed much larger variability across solar cycles for some UV wavelengths than previous observations.

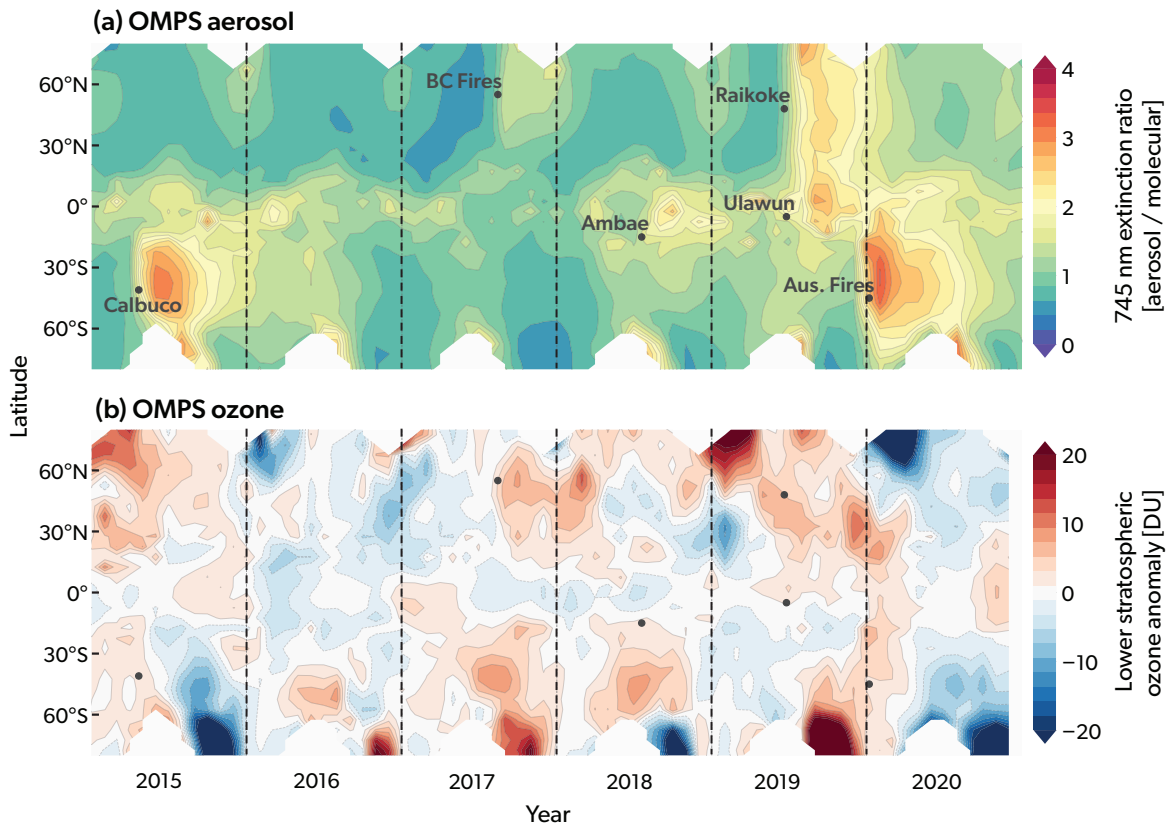


**Figure 3-3.** (a) Ratio of OMPS-LP lower-stratospheric aerosol extinction at 745 nm to molecular scattering, an indicator of the presence of aerosols. Major sources of stratospheric aerosol during 2015–2020 are indicated. (b) Deseasonalized lower-stratospheric ozone anomaly from OMPS-LP. [Adapted from Rieger et al., 2021.]

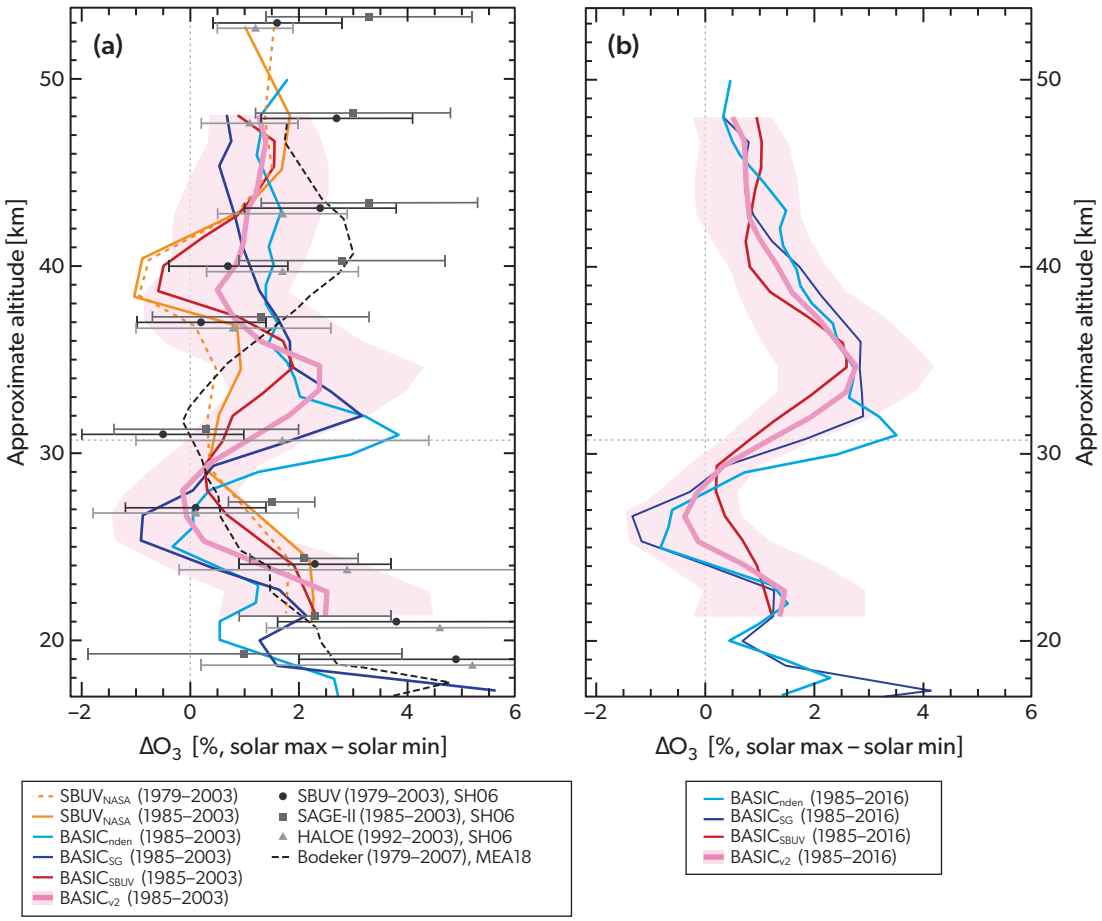


**Figure 3-4.** The response in upper-stratospheric tropical (25°S–25°N) ozone due to solar cycle forcing (solar maximum minus solar minimum) for different datasets and time periods. (a) Analyses performed over different periods (between 1979 and 2007) by Maycock et al. (2018) ("MEA18"; dashed), using ozone data from Bodeker Scientific ("Bodeker"; Bodeker et al., 2013); Soukharev and Hood (2006) ("SH06"), using ozone data from SBUV (black circles), SAGE-II (dark gray squares), and HALOE (light-gray triangles); and sensitivity analyses for periods that end in 2003 using the SBUV NASA (MOD) data only (orange, solid/dashed) and using different versions of the BASIC dataset (Ball et al., 2017, 2019b; light blue, blue, red, pink). (b) Analyses performed with the SBUV and BASIC ozone datasets for the full analysis period, 1985–2016 (colors in legend represent the same datasets as in the legend in [a]). [Adapted from Ball et al., 2019b.]

However, observed and reconstructed SSI datasets driven by analysis of new SSI observations from the SORCE satellite mission are now converging, reducing uncertainties in the attribution of ozone variability to SSI variability. Variability in UV fluxes in cycle 24 (1996–2008) reported early in the SORCE mission was larger than previous estimates (Harder et al., 2009) and has been regularly revised down. In cycle 25 (2008–2019), SORCE observations showed relatively lower variability, in better agreement with that of the two main SSI reconstructions (Krivova et al., 2010; Yeo et al., 2014; Coddington et al., 2016). These reconstructions have been merged to form the climate model forcing data for the latest generation of multi-model experiments (e.g., CMIP6; see **Box 3-4**; Matthes et al., 2017). Moreover, retrievals from TSIS, SORCE's successor, also display similar behavior to these solar irradiance reconstructions, albeit only within uncertainties and for a short overlap period (Mauceri et al., 2020).

Finally, since the previous Assessment, there have been additional chemistry-climate model (CCM) simulations of the solar-ozone response in the tropical lower stratosphere. The response in ozone was as high as 6% in earlier analyses (Austin et al., 2008); in the new simulations, the response is smaller, ~2%, and more consistent across CCMs (Maycock et al., 2018). However, some differences in the solar response remain in CCMs, attributable to remaining uncertainties in solar cycle SSI changes and structural uncertainty in the models (Kunze et al., 2020).

### *3.2.1.5 Other Dynamical Influence Factors*

Patterns of atmospheric circulation and transport have a marked effect on the distribution of ozone around the globe. In addition to sources of transport already discussed as part of other natural variability proxies, some of the largest influences on ozone variability are the BDC, atmospheric jets and waves, and the direct exchange of air between the lower stratosphere and upper troposphere. Some of the more influential examples of these different mechanisms are discussed here.

The BDC describes the global-scale meridional circulation in the stratosphere. It largely dictates the distribution of stratospheric ozone through transport and chemistry and is driven by atmospheric waves originating in the troposphere (e.g., Butchart, 2014). While long-term trends in the BDC (*Chapter 5*) will impact long-term ozone trends, variability at shorter timescales is also important. For example, ozone trends calculated in BDC-sensitive locations (such as the tropics at ~35 km) vary considerably depending on the time period analyzed, and this has been attributed to sub-decadal variation in the strength of the BDC (Arosio et al., 2019; Galytska et al., 2019). At multi-decadal timescales, BDC strength may be coupled to the Interdecadal Pacific Oscillation (IPO; e.g., Henley et al., 2015). Model simulations suggest that the IPO could explain up to 50% of the decadal variability in tropical mid-stratosphere ozone (Iglesias-Suarez et al., 2021).

Year-to-year variability of the polar vortex strength also influences the ozone distribution not only in polar regions but also at mid-latitudes. This is especially important for the Northern Hemisphere, where the polar vortex is often disturbed by planetary wave activity. In particular, the anticipated ozone recovery in late winter has been shown to be sensitive not only to ODS decline but also to the polar vortex changes, and late-winter ozone recovery could be substantially delayed in some regions of the NH extratropics due to trends in the polar vortex driven by climate change (Zhang et al., 2018; von der Gathen et al., 2021; see also *Chapter 4*).

Another source of ozone variability in the lower stratosphere are intrusions of tropospheric air. The uplift of tropospheric air occurs along the ascending warm conveyor belt of the cyclonic structure (Stohl, 2001). Most tropospheric intrusions do not reach high altitudes, predominantly staying within the UTLS layer, where their impact on ozone concentrations is comparatively small. However, deep intrusions can even lead to the formation of intermittent ozone "mini-holes" (Reutter et al., 2015; Sofiev et al., 2020). A recent example of tropospheric influence is the persistent smoke-charged vortex generated by the 2019/20 Australian wildfires, which caused an ozone mini-hole (Khaykin et al., 2020). Currently, tropospheric intrusions do not have a noticeable impact on ozone trends, but the impact could increase if such events became more frequent in the future (see also *Section 3.2.1.3*).

The previous Assessment detailed dynamical proxies that can be used in the ozone trend analysis-eddy heat flux (EHF), tropopause pressure, the Arctic Oscillation (AO), the North Atlantic Oscillation (NAO), the Antarctic Oscillation (AAO), and an index for the upper branch of the BDC (UBDC)—with more recent studies also using proxies related to the Indian Ocean Dipole (Krzyścin, 2017; Thompson et al., 2021; **Table 3A-1**). Using dynamical proxies can improve the regression fit in some regions, but they can only partly explain the complicated and intermittent structure of dynamical variability. Moreover, since changes in dynamics can also be a response to a long-term driver, the use of these proxies requires care in interpreting what is driving and what is responding to long-term perturbations. However, at least for the middle and upper stratosphere, zonally averaged ozone trends outside of the polar regions are not very sensitive to the inclusion of EHF, NAO/AO, and AAO indices. (SPARC/IO3C/GAW, 2019; see also *Section 3.2.2*).

### 3.2.2 Long-Term Trends and Trend Models

In addition to proxies for natural variability, regression model approaches for understanding changes in ozone also include a long-term trend component (Laine et al., 2014; Weber et al., 2018; SPARC/IO3C/GAW, 2019). This component does not necessarily have a well-defined form or cause. Obvious candidates are long-term changes in ODSs or temperature, but any long-term changes in transport mechanisms or concentrations of non-halide species involved in regular ozone chemistry can play a role.

The statistical approach to modeling ozone determines how the long-term changes are captured. In multiple linear regression (MLR; e.g., see WMO, 2018), the form of long-term changes is prescribed, usually being either linear or chemistry based. Linear forms, such as the piecewise linear trend (PWLT; Newchurch et al., 2003) and independent linear trend (ILT; WMO, 2014; Weber et al., 2018; SPARC/IO3C/GAW, 2019), allow for the possibility of a turnaround in the trend but will not follow the curvature of ODS-related changes. Chemistry based forms, such as the EESC proxy (Newman et al., 2007) or EOFs based on it (Damadeo et al., 2014), assume a turnaround in the long-term trend related to the mean age-of-air, which itself may be variable over time (Li et al., 2018). However, these will be ineffective (single proxy) or less effective (2 x EOF proxy) in representing monotonic trends. On the other hand, dynamic linear model (DLM; Laine et al., 2014; Ball et al., 2018; Alsing, 2019) or ensemble empirical model decomposition (EEMD; Bai et al., 2017; Boleti et al., 2020) approaches can estimate a smoothly varying background trend without assuming its shape. These trend models allow the freedom to accurately represent the nonlinearity of long-term changes, whether they have a turnaround or are monotonic. However, the curvature near the beginning or end of the analysis period is less constrained and subject to larger influence from interannual variability, especially when this is not well represented by the proxies, although such

**Table 3-1.** Comparison of five different trend models for ozone. Abbreviations are defined as follows (see also *Section 3.2.2*): piecewise linear trend (PWLT), independent linear trend (ILT), effective equivalent stratospheric chlorine (EESC), EESC empirical orthogonal functions (EESC EOFs), and dynamic linear model (DLM).

| | PWLT | ILT | EESC | EESC EOFs | DLM |
|---|---|---|---|---|---|
| Allows for a variable turnaround date | No | Yes | No | Yes | Yes |
| Allows for monotonic trends | Yes | Yes | No | Yes | Yes |
| Can follow nonlinearity of chemical changes | No | No | Yes | Yes / Not as well when monotonic | Yes |
| Local trend affected by end data (relative comparison between methods) | Middle | Middle | Smallest | High | Highest |
| Comparative computational cost | Low | Low | Low | Low | High |

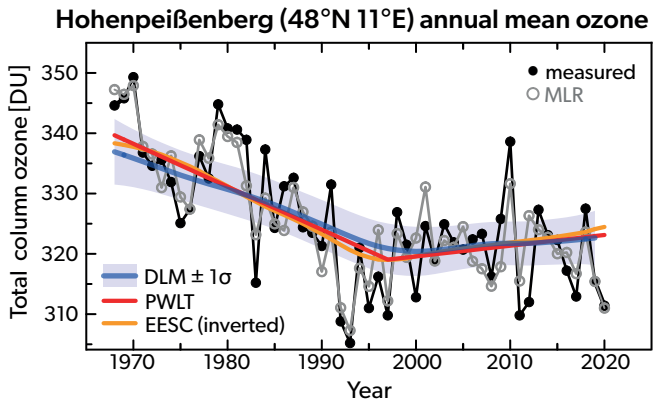


**Figure 3-5.** Example comparison between different trend models fitted to annual mean TCO at Hohenpeißenberg. Observations (solid black circles) are fitted with an MLR regression model including a PWLT and proxies for the QBO, solar cycle, Arctic Oscillation, and stratospheric aerosol with chlorine weighting (open gray circles). Also shown are different trends: an MLR-based trend result using a PWLT (red line), a single EESC-based trend (orange line), and a DLM-based trend (blue line) with its 1σ-uncertainties (blue shading). Despite differences over shorter timescales in the representation of the nonlinearity of changes in the data, the overall trends are similar among the three trend models. [Adapted and updated from Steinbrecht et al., 2011.]

influence is encompassed by larger uncertainties during these periods. The pros and cons of the different trend models are outlined in **Table 3-1**, but it is important to note that when applied to decades of data, trends are usually well represented by all of the models (**Figure 3-5**), with varying levels of uncertainty.

While the choice of trend model is important, the methodology of the applied analysis is equally, if not more, important. Trend analyses rely on widely accepted statistical regression techniques that are becoming increasingly sophisticated (e.g., more aspects of variability, more detailed uncertainty analysis). The most commonly applied technique is MLR, but DLM-like techniques have become increasingly popular, especially with the availability of pre-written code (Alsing, 2019), and are being explored in community-wide efforts like LOTUS (SPARC/IO3C/GAW, 2019). Current implementations of both MLR and DLMs are similar in their underlying construction and assumption of a linear dependence of the regressed data on proxies. However, they differ fundamentally in their underlying statistical principles (Bayesian versus frequentist; see **Box 3-1**) and in how they model the time evolution of the data.

DLMs are underpinned by a Kalman filter framework and have advantages over traditional MLR approaches (Alsing, 2019): they allow 1) a flexible, time-varying background trend, 2) seasonal and regressor variables to modulate in time, 3) a better treatment of auto-regressive processes, and 4) a better treatment of time-varying errors. While many of these can be incorporated into ever-more complex MLR models, it is the smoothly varying trend, with no assumption of when or how many inflection points might occur, that has the most obvious advantage over MLR (**Figure 3-5**). For this reason, DLM approaches are more flexible and provide more information about how ozone evolves over time, particularly for the seasonal and trend components.

Ultimately, both techniques are useful for long-term trend analyses, with each having its own benefits and caveats. Although increasing the complexity of statistical models comes at the cost of a substantial increase in the required computing power (especially for DLMs or similar), these more complex models can be applied to gain more insightful and robust results.

### 3.2.3 Trend Significance

No value carries substantial meaning without an associated uncertainty. It is important to know whether the result is different from zero by greater than some margin of uncertainty (known as statistical significance). Statistical significance offers a convenient way to display in a single figure both the magnitude of trends and their "importance." The most commonly used metric of significance is the 95% confidence interval, assuming a Gaussian distribution (2σ for most statistical applications), but the choice is somewhat arbitrary. Results that are significant at the 90% (or lower) confidence interval, for instance, may still be valid and worthy of discussion. Moreover, multiple significance tests (e.g., trends at different grid points) alter the calculation of significance (Wilks, 2006). Note that studies that take a Bayesian perspective on data analysis will quote "credible intervals"; while these require a slightly different interpretation, they can be regarded in a similar way (**Box 3-1**).

For the sake of comparison with previous Assessments, uncertainties shown throughout this chapter are the 2σ uncertainties, unless otherwise stated. However, it is important to note that trend results displayed where uncertainties encompass zero may still be indicative of meaningful change and may be worth discussing. Finally, unless otherwise stated, uncertainties reported here are random statistical uncertainties and do not consider the potential influence of data quality complications (e.g., sampling biases or instrumental drifts; see *Section 3.1*) as these are generally not included or quantified in the referenced studies.

## 3.3 PAST OZONE

Investigating past changes in ozone in observations and in models is critical to both understanding the impacts of natural and anthropogenic forces on ozone in Earth's atmosphere and evaluating the efficacy of the Montreal Protocol. Analysis of past ozone is performed on two representations of ozone: total column ozone (TCO) and vertical profiles. Total column measurements encompass all ozone from the surface to the top of the atmosphere and are useful because they best represent changes in how much damaging solar UV radiation reaches Earth's surface. To fully understand why these changes occur requires knowledge of the vertical distribution of ozone, provided by vertical profile measurements or partial columns. Analysis of profile observations is focused primarily on the stratosphere, where the ozone layer is located and where global satellite observations are of highest quality.

Analyses of long-term stratospheric ozone trends have traditionally been broken down into two periods: before and after the late-1990s/early-2000s. As reported in previous Assessments, ozone exhibits a noticeable decrease in the stratosphere at almost every altitude and latitude from the time when global observations started in the late 1970s until the late 1990s, after which it appears to flatten out or even increase (see also *Section 3.3.2.1*). While the magnitude of the pre-1990s decrease varies by location, the primary contributor to the decrease was the increase of ozone-depleting substances (ODSs) in the stratosphere, the concentration of which peaked in the late 1990s (*Chapter 1*). The results of trend analyses on this "pre-turnaround" period have been extensively discussed in prior Assessments and have not changed appreciably, even with the addition of new analysis techniques. As such, the discussion here mainly focuses on the period after the peak of ODSs in the stratosphere.

This section assesses changes in TCO (*Section 3.3.1*) and the vertical distribution of ozone (*Section 3.3.2*). In addition, special focus is given to the upper troposphere/lower stratosphere (UTLS) region, where a large fraction of atmospheric ozone resides, where the dynamical variability is largest, and where there has been considerable uncertainty in the ozone trends and discrepancies with models (*Section 3.3.3*). Finally, attention is also given to model simulations of past ozone changes and their use in attributing different drivers of ozone trends (*Section 3.3.4*). Information on the measurement datasets can be found in *Appendix 3A* and the associated tables (**Tables 3A-2 to 3A-5**).

## 3.3.1 Changes in Total Column Ozone

### *3.3.1.1 Interannual Variability*

Since the mid-1990s, there has been only a small long-term trend in TCO, with substantial year-to-year variability. The time series of annual mean TCO are shown in **Figure 3-6** for the near-global average (60°S–60°N) and three selected broad-latitude bands (35–60°N, 20°S–20°N, 60–35°S; Weber et al.,

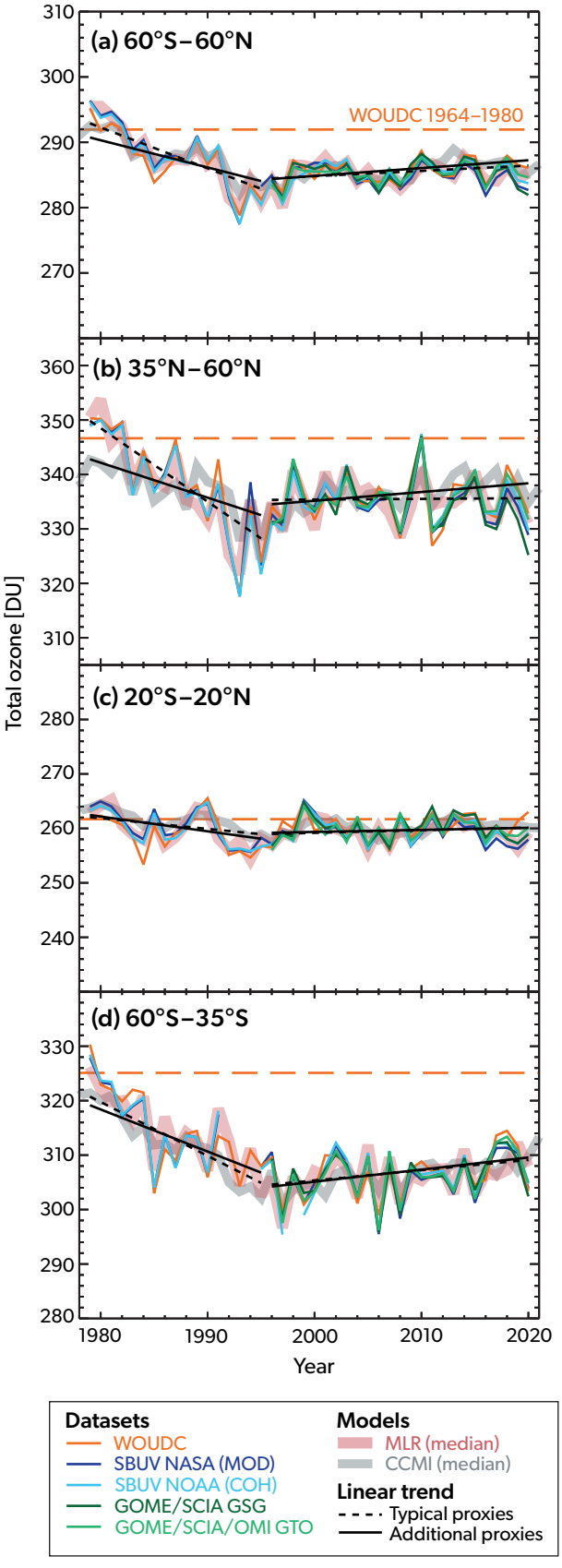


**Figure 3-6.** Time series of annual mean TCO (in DU), for 1979–2020, and linear trends, for 1979–1995 and 1996–2020, in four zonal bands: near global (60°S–60°N), NH mid-latitudes (35–60°N), tropics (20°S–20°N), and SH mid-latitudes (60–35°S). Data are from WOUDC ground-based measurements combining Brewer, Dobson, SAOZ, and filter spectrometer (orange); the BUV/SBUV/SBUV2 v8.7/OMPS merged products from NASA (MOD v8.7, dark blue) and NOAA (COH, light blue); the GOME/SCIAMACHY/GOME-2 products from University of Bremen (GSG; dark green); and the GOME/SCIAMACHY/GOME-2/OMI products from ESA/DLR (GTO; light green). See *Appendix 3A* for the references associated with these datasets. All five datasets have been bias-corrected by subtracting averages for the reference period 1998–2008 and adding back the mean of these averages. The dashed lines in each panel show the average ozone level for 1964–1980 calculated from the WOUDC data. The thick red lines show the median of MLR models. The black dashed lines are the linear trend as calculated with an MLR trend model using typical proxies, whereas the solid black lines are the linear trends as calculated with an MLR with additional dynamical proxies (see *Section 3.3.1.2*). [Adapted from Weber et al., 2022.]

2022). On average, the current (2017–2020) TCO is about 2.3% below the 1964–1980 mean (reference mean) in the near-global average, about 1.1% below the reference mean in the tropics, and about 3.6% and about 4.7% below the reference mean in the NH and SH mid-latitudes, respectively (**Figure 3-6**).

Most of the anomaly pattern in the annually averaged ozone in years since the previous Assessment is well understood and can be explained with varying combinations of dynamical influences (Matthes et al., 2010; Domeisen et al., 2019; Coldewey-Egbers et al., 2020; Section 3.2). For example, the influence of the Quasi-Biennial Oscillation (QBO) on ozone can be seen in the 2018 anomalies. Compared to the annual means observed in the last decade, NH and SH mid-latitude TCO values were high and the tropical values were low, all associated with the easterly phase of the QBO at 50 hPa. Moreover, an assessment of the impact of major sources of natural variability on recent ozone interannual variability is consistent with established correlations in ozone anomalies with the QBO at 30 hPa, El Niño-Southern Oscillation (ENSO), and solar cycle signals (Coldewey-Egbers et al., 2020).

In 2019, the SH mid-latitude TCO anomalies remained high. A persistent, weak polar vortex (perturbed by a SH stratospheric warming event; *Chapter 4*) associated with a strong hemispheric Brewer-Dobson circulation (BDC) led to more ozone being transported into SH mid-latitudes (Weber et al., 2020). The 2020 annual near-global mean and the annual mid-latitude mean in both hemispheres are below the decadal average of 1998–2008 (Weber et al., 2022). This negative anomaly, which is still within the variability observed in recent years, is due to a combination of very low polar ozone during the Arctic winter/spring (Weber et al., 2022), a large and stable Antarctic ozone hole during that year (see *Chapter 4*), and potentially the impact of the Australian wildfires on the stratosphere (*Section 3.2.1.3*).

The disruption of the downward propagation of the QBO westerly phase in 2019/20 is similar in many aspects to the one observed in 2016 (WMO, 2018; SPARC/IO3C/GAW, 2019, and references therein) but was initiated by horizontal momentum transport from the Southern Hemisphere (see *Section 3.2.1.1*). Some influence of this event might have contributed to the observed 2020 TCO anomalies, which are similar to 2016 and are consistent with our understanding of QBO-induced air mass transport (Weber et al., 2022). Overall, with four more years of data, our understanding of interannual TCO variability remains robust and unchanged compared to the previous Assessment.

### *3.3.1.2 Trends*

The TCO trend estimates for the time series shown in **Figure 3-6** are based on a multiple linear regression (MLR) method (fit shown as black lines) that uses the typical proxies (see *Section 3.2.1*

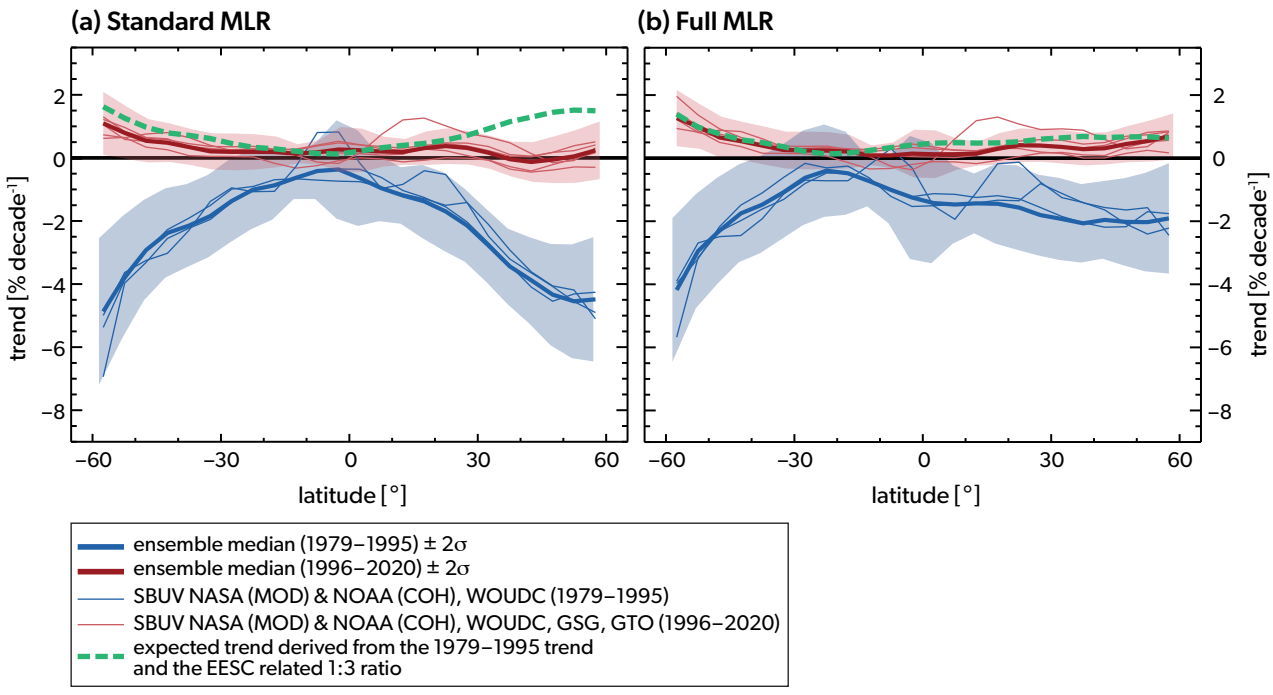


**Figure 3-7.** TCO linear trend in % decade$^{-1}$ as a function of latitude for 1979–1995 (blue) and 1996–2020 (red), estimated using SBUV NASA (MOD), SBUV NOAA (COH), GTO, GSG, and WOUDC datasets, with (a) an MLR model that includes typical proxies and (b) an MLR model that includes additional dynamical proxies (see *Section 3.3.1.2*). Trends shown are the linear trend (% decade$^{-1}$) of the ensemble median (thick blue and red lines), as well as the 2σ uncertainty (blue and red shading) from the regression. Overlayed thin lines show trends from individual datasets without their uncertainties. Also shown (dashed green line) is the expected trend from changes in ODSs alone. This is derived from the 1979–1995 ODS trend, as represented by EESC, and by applying a scaling to account for the rate of change in EESC post-1996 relative to pre-1996 (i.e., "EESC-related 1:3 ratio"). [From Weber et al., 2022.]

and **Table 3A-1**) and the independent linear trend (ILT) model (**Table 3-1**) (Weber et al., 2022). Trend estimates are derived for the near-global (60°S–60°N) annual mean and for annual mean zonal-mean data in the same three latitude bands considered for the TCO year-to-year variability. Near-global 1996–2020 trends are on the verge of a significant increase (+0.3 ± 0.3% decade$^{-1}$; Weber et al., 2022), whereas trends in different latitude bands do not show a uniform picture. In the SH mid-latitudes, the trend is significant at the 2σ level (+0.8 ± 0.7% decade$^{-1}$), while the trend in NH mid-latitudes is negligible and not significant (+0.0 ± 0.7% decade$^{-1}$), and there is only a small non-significant trend after 1996 in the tropics (+0.2 ± 0.3% decade$^{-1}$). Similar trend values were reported in the last Assessment (see also SPARC/IO3C/GAW, 2019), although with four more years of data and an updated trend model, the near-global mean and SH mid-latitude trend become significant. The apparent discrepancy in the significance of near-global and latitudinally resolved trends is a result of different causes for variability in the three latitude bands, which can compensate for each other when aggregated globally (see also Coldewey-Egbers et al., 2014; Steinbrecht et al., 2018; Weber et al., 2018).

Latitude-dependent TCO trends are shown in **Figure 3-7a** in 5° latitude bins for the 1979–1995 and 1996–2020 periods. The pre-1996 decreases, which have been discussed extensively in previous Assessments, show a latitudinal dependence, with values ranging from nearly zero in the tropics to statistically significant negative trends at mid-latitudes in both hemispheres. The latitude-dependent trends after 1996 are largely consistent with the results for the broader zonal bands and with those given in the last Assessment (see also Weber et al., 2018), even with an additional four years of data. There are small (<1% decade$^{-1}$), mostly positive trends in the SH mid-latitudes and near zero (<0.5% decade$^{-1}$) trends in the tropics and NH mid-latitudes. Almost all the trends are statistically insignificant.

While computing trends in TCO is important, understanding what causes these trends is equally so. An attempt at isolating trends from ODS-induced changes only is shown in **Figure 3-7b**. The trends shown in **Figure 3-7** are derived from nearly identical MLR analyses (Weber et al., 2022), with both incorporating explanatory variables for natural variability (i.e., QBO, ENSO, solar, and aerosol) and ILT-proxy trends, but differing in that **Figure 3-7b** also includes AO (Arctic Oscillation), AAO (Antarctic Oscillation), and BDC proxies (**Table 3A-1**). These additional dynamical proxies have a trend themselves, meaning the resulting trend from the regression is no longer representative of all long-term changes in TCO. An independent estimate of the "expected" ODS-related post-1996 changes, which is based on equivalent effective stratospheric chlorine (EESC), is shown as dashed green lines in **Figure 3-7**. ODS concentrations, as represented by EESC, are expected to decrease at about one-third of the rate they increased before the 1990s (Dhomse et al., 2006; Weber et al., 2018), and so the magenta lines are simply the pre-1996 trends multiplied by –⅓, illustrating what the post-1996 trends would look like assuming they were purely driven by ODS changes. The derived post-1996 trends in both the Northern and Southern Hemisphere are in much better, though not complete, agreement with the estimated ODS-based trends when the additional explanatory variables (**Figure 3-7b**) are used in the regression. This suggests that the linear trends from **Figures 3-6** and **3-7b** are to a large part attributable to ODS changes only, demonstrating the success of the Montreal Protocol and its Amendments and adjustments at protecting stratospheric ozone. It also implies that the additional proxies are useful in capturing important components of dynamical variability, including how possible trends in dynamics impact long-term changes in ozone. The difference between the derived post-1996 trends in **Figures 3-7a** and **3-7b** suggests that the long-term changes in dynamics, as captured by the AO, AAO, and BDC proxies, are contributing to negative trends of up to 0.5% decade$^{-1}$ in TCO, offsetting the positive ODS related trends, particularly in NH mid-latitudes.

When the MLR, including the additional dynamical proxies, is applied to the data for the broad-latitude bands (**Figure 3-6**, black solid line), trends and significance for the latitude bands change compared to the results of the MLR without these proxies. Trends for the near-global (+0.4 ± 0.2% decade$^{-1}$) and SH mid-latitude (+0.7 ± 0.6% decade$^{-1}$) TCO are significant (Weber et al., 2022), and the NH mid-latitude trends are on the verge of significance (+0.5 ± 0.5% decade$^{-1}$), but the tropical trends are still not significant, even with the additional proxies considered.

Besides the differences in latitudinally resolved trends, TCO trends, derived from the period 1997–2020, also show a longitudinal dependence. Trends derived from a recently updated dataset based on GOME-type (GTO) satellite measurements (Coldewey-Egbers et al., 2022), with a MLR trend model where dynamical proxies for the AO and AAO are included, are positive in most parts of the globe (**Figure 3-8**) and statistically non-significant (at 0.3 ± 0.6% decade$^{-1}$) in the tropics but significant (at 1.0 ± 0.9 % decade$^{-1}$) for some regions of the SH mid-latitudes. The largest positive trends of about 1.5% ± 1.0% decade$^{-1}$ are found in in the NH in the northwestern part of Europe and in the North Atlantic region and in the SH higher latitudes (up to 2.8 ± 2.6 % decade$^{-1}$) in the region of the Southern Ocean, while non-significant trends are estimated above Eurasia (–1.0 ± 1.0 % decade$^{-1}$). GTO-derived trends are consistent with the latitude band picture given by WOUDC and SBUV datasets (see **Figure 3-7**), where TCO trends during the recovery period are only significant in the SH mid-latitudes (Coldewey-Egbers et al., 2022).

In a different study, zonally asymmetric TCO trends estimated using principal component analysis on a dataset combining TOMS, GOME, SBUV, and OMI for the 1997–2015 period are reported as negative and significant over the North Pacific and positive and significant over northwestern North America in February (Zhang et al., 2019). This asymmetric behavior is attributable to a polar vortex shift, which causes not only interannual variability of regional TCO but also a significant reduction of TCO over the central Eurasian continent (**Figure 3-8**). This effect is opposite to the expected increase in ozone due to reduced atmospheric ODS concentrations and is an example of how dynamical changes could affect the timing of TCO recovery in different regions (Zhang et al., 2018).

Ground-based FTIR measurements provide total column ozone and ozone partial columns for the period 2000–2020. Post-2000 TCO trends estimated from five different FTIR measurement sites are consistent, within their uncertainties, with trends estimated from the WOUDC and SBUV datasets as determined by MLR with the typical proxies (see **Figure 3-7**). TCO trends over 2000–2020 at FTIR stations within the NH mid-latitudes and in the tropics are slightly negative but non-significant, while the trend at a station in the SH mid-latitudes is positive and significant at 1.1 ± 0.9% decade$^{-1}$ (updated from Vigouroux et al., 2015).

Seasonally resolved post-1997 TCO trends have also been derived from the GTO 5° × 5° gridded dataset. The seasonality in the trend is not very pronounced, and most of the regions show trends that are not significant at the 95% confidence level. In the Northern Hemisphere, a strong trend over the North Atlantic is significant and positive for all seasons and varies in intensity, and a negative trend over Eurasia is significant except in winter (December to February). In the Southern Hemisphere, regions of significant positive trends are reported throughout the year in the extratropics but are stronger between March and May in the mid-latitudes (the Pacific region, south of Africa, and south of Australia; Coldewey-Egbers et al., 2022).

## 3.3.2 Changes in the Vertical Distribution of Ozone

### *3.3.2.1 Time Series*

The ozone decline in the 1980s and 1990s, caused by increasing atmospheric concentrations of ODSs, has now transitioned to a slow ozone increase in both hemispheres (SPARC/IO3C/GAW, 2019). This is consistent among the ground- and satellite-based measurements and model simulations from the Chemistry-Climate Model Initiative (CCMI-1; REF-C2 experiment: see Morgenstern et al., 2017) for all latitude bands and in the middle and upper stratosphere, despite the larger variability of the ground-based measurements. This is apparent in the evolution of observed and modeled annual mean deseasonalized ozone anomalies, relative to the 1998–2008 climatology of each individual plotted dataset, in the upper stratosphere (42 km or 2 hPa) and in the lower stratosphere (19 km or 70 hPa), as shown in **Figure 3-9**. A direct comparison of individual years between the CCMI-1 output and measured anomalies is not possible as natural forcings and variability in the REF-C2 simulations used in this comparison are either absent or are not as observed (e.g., volcanoes, QBO).

Ozone anomalies over 2017–2020 in the upper stratosphere from most datasets are positive relative to the 1998–2008 average, consistent with expectations from the CCMI-1 simulations. This is true for the NH and SH mid-latitudes and to a lesser extent for the tropics. In contrast, lower-stratospheric ozone anomalies over 2017–2020 continue to be about the same as for the 1998–2008 average. In 2019 and 2020, stratospheric ozone values were lower than in previous years and below the level expected from model simulations (Weber et al., 2020). The particularly low 2020 annual mean is the result of a very weak BDC and a large and stable Antarctic ozone hole (Klekociuk et al., 2021; Weber et al., 2021). Such large variability, driven by variations in meteorology and transport (Chipperfield et al., 2018), is typical for the lower stratosphere and impedes drawing definite conclusions about long-term trends, especially for the mid-latitudes (30°–60°) in both hemispheres (see *Section 3.3.3*).

### *3.3.2.2 Trends as a Function of Latitude*

Estimates of vertically resolved trends as a function of latitude are possible from seven merged satellite ozone datasets, which include the six datasets used in the last Assessment and by LOTUS (SPARC/IO3C/GAW, 2019) alongside the new SAGE II-SCIAMACHY-OMPS dataset (Godin-Beekmann et al., 2022). Altitude-latitude cross sections of ozone trends for 2000–2020 (**Figure 3-10**) are similar to those reported in the last Assessment, with the new SAGE II-SCIAMACHY-OMPS dataset yielding results that are similar to those from the other SAGE-containing datasets. All the datasets show positive and statistically significant trends for the post-2000 period in the upper stratosphere, in the range of about 2–7% decade$^{-1}$, with more pronounced trends at mid-latitudes than in the tropics in both hemispheres. Except for SBUV MOD, all results indicate positive tropical trends in the upper stratosphere (above ~40 km), although the trends are somewhat smaller and not always statistically significant. Trends in the middle stratosphere (25–40 km) are slightly positive (0–3% decade$^{-1}$) in most datasets at SH mid-latitudes and slightly negative (−2–0% decade$^{-1}$) at NH mid-latitudes and in the tropics, although these are typically not statistically significant. Estimated trends in the lower stratosphere (tropopause to 25 km) are mostly negative but are also rarely statistically significant. The trends were determined using the ILT regression model (*Section 3.2.2*), which was applied to the full available observational period (1984–2020).

Profiles of ozone trends in broad-latitude bands for the same seven datasets (**Figure 3-11**) all show significant positive ozone trends in the upper stratosphere at mid-latitudes in both hemispheres (60–35°S and 35–60°N), in the range of 1–3% decade$^{-1}$ (mean ~1.9% decade$^{-1}$ in the Southern Hemisphere and ~2.2% decade$^{-1}$ in the Northern Hemisphere) for the post-2000 period. In the tropical (20°S–20°N) upper stratosphere, the trends

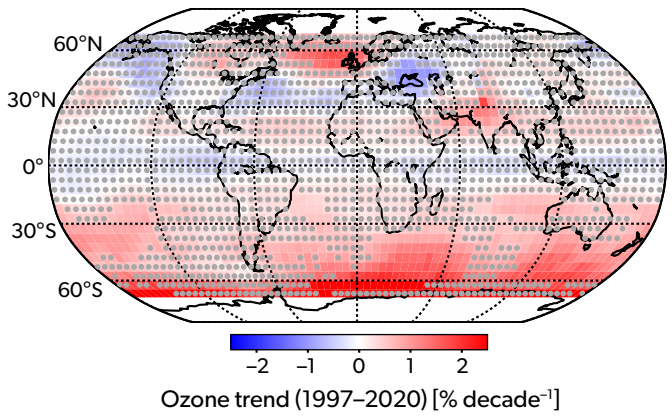


**Figure 3-8.** Latitude- and longitude-dependent TCO trends (5° × 5° resolution) derived using MLR (including AAO/AO but not the BDC) for the 1997–2020 period, in % decade$^{-1}$. Trends are from GOME-type satellites (GTO), which include measurements from GOME, SCIAMACHY, OMI, and TROPOMI. Gray dots denote locations where the trends are not significant at the 95% confidence level. [Figure from Coldewey-Egbers et al., 2022].

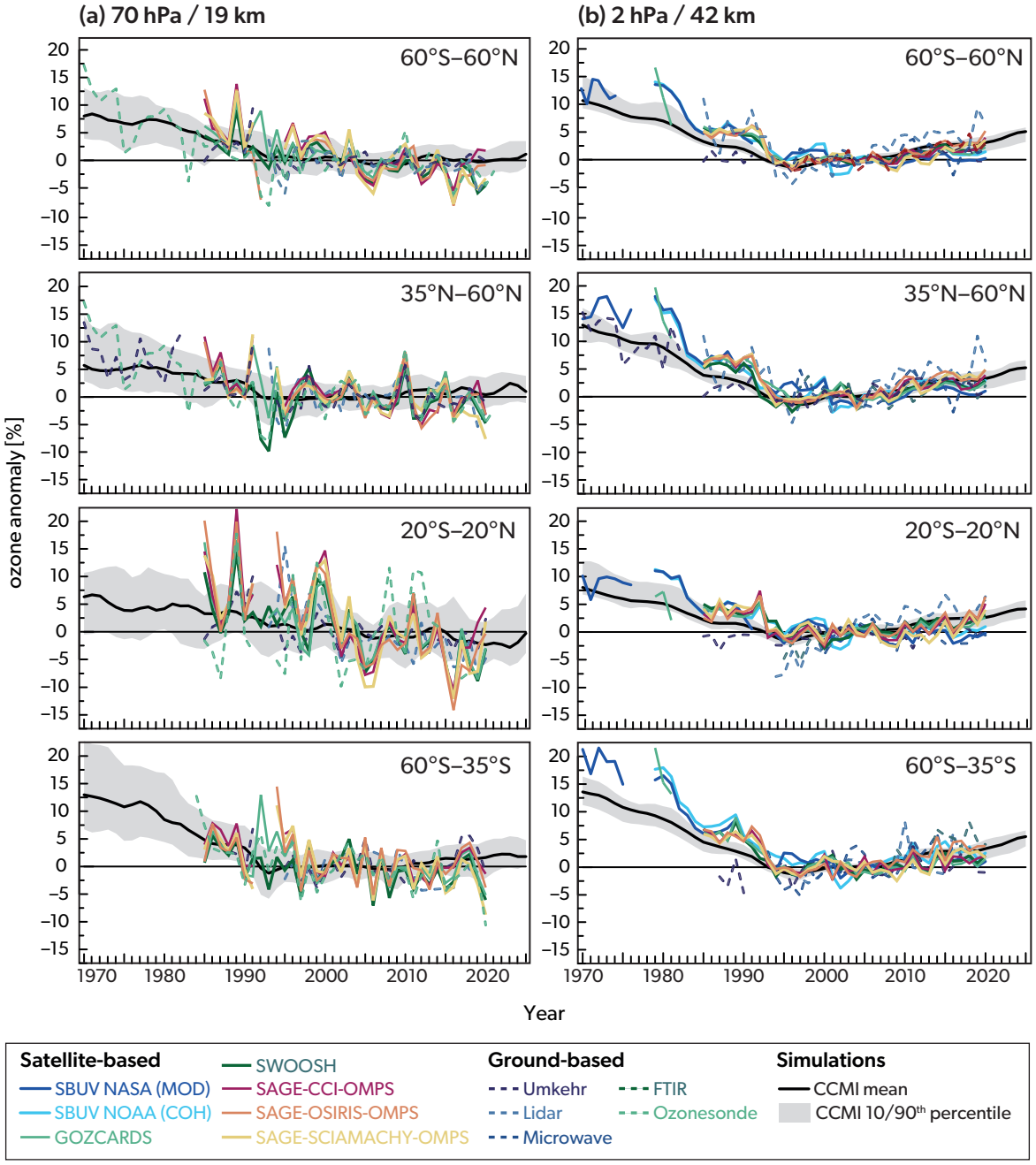


**Figure 3-9.** Annual mean anomalies of ozone in (a) the lower stratosphere, near 19 km altitude (70 hPa pressure) and (b) the upper stratosphere, near 42 km (2 hPa), for four latitude bands: 60°S–60°N, 35–60°N, 20°S–20°N (tropics), and 60–35°S. Anomalies are referenced to a 1998–2008 baseline. Colored lines are long-term records obtained by merging data from different nadir (SBUV NASA (MOD) and SBUV NOAA (COH)) or limb-viewing (GOZCARDS, SWOOSH, SAGE-CCI-OMPS, SAGE-OSIRIS-OMPS, SAGE-SCIAMACHY-OMPS) satellite instruments. Dashed colored lines are long-term records from ground-based observations (Umkehr, lidar, microwave, FTIR and ozonesondes); see Steinbrecht et al. (2017), WMO (2018), and Arosio et al. (2018) for details on the various datasets. The gray shaded areas show the range (10th and 90th percentiles) of 16 CCM simulations performed as part of the CCMI-1 REF-C2 experiment (see Morgenstern et al., 2017) with the black line indicating the median. [Adapted from SPARC/IO3/GAW, 2019, and updated from the last Assessment.]

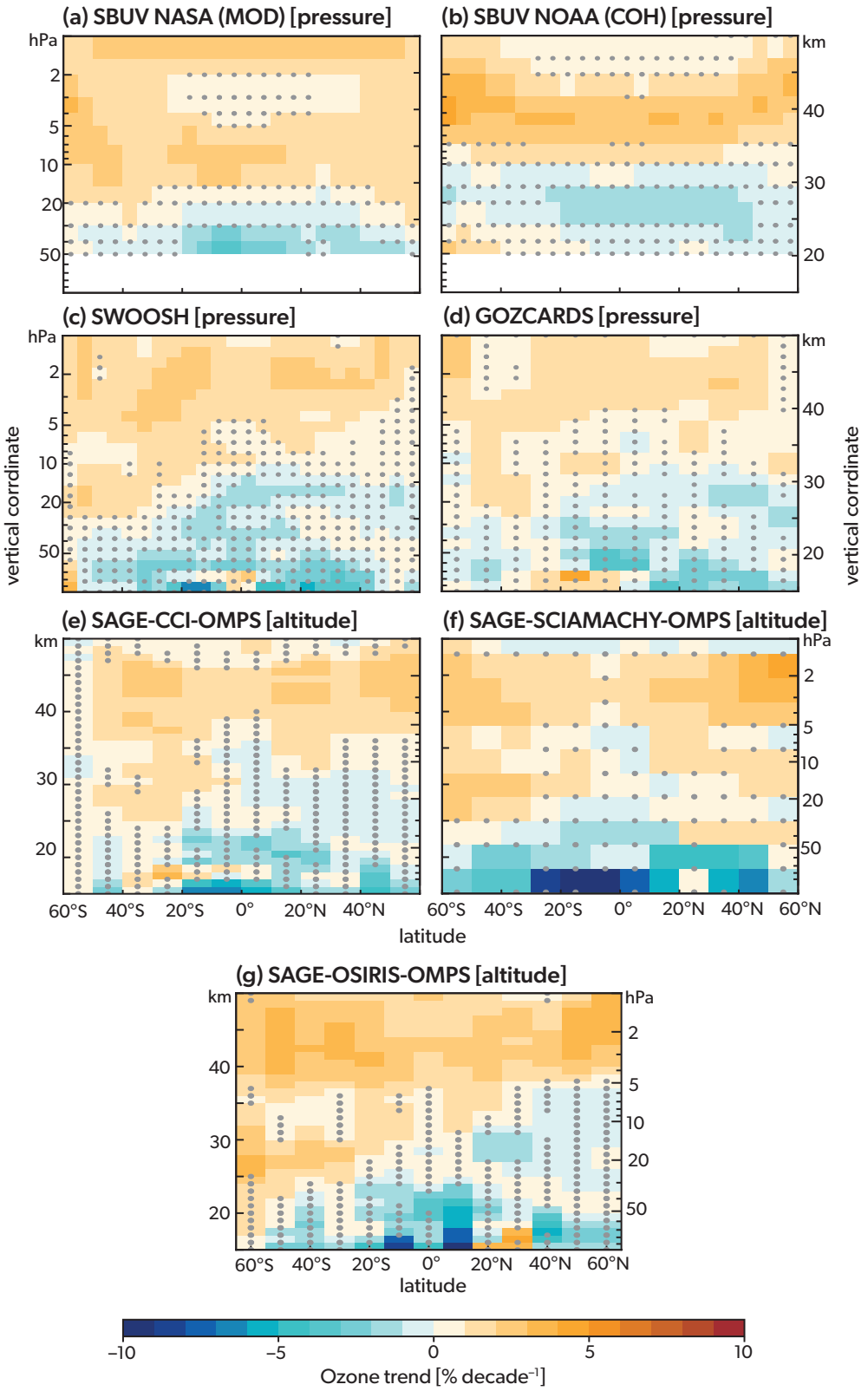


**Figure 3-10.** Ozone trends (% decade$^{-1}$) for the period 2000–2020 estimated from seven merged satellite data records using an independent linear trend model. Trends are shown for the (a) SBUV NASA (MOD), (b) SBUV NOAA (COH), (c) SWOOSH, (d) GOZCARDS, (e) SAGE-CCI-OMPS, (f) SAGE-SCIAMACHY-OMPS, and (g) SAGE-OSIRIS-OMPS datasets. Gray stippling denotes results that are not significant at the 2σ level. Data are presented on the vertical coordinates (lefthand axis; square brackets in title) and latitudinal grid associated with each dataset. [Adapted from Godin-Beekmann et al., 2022.]

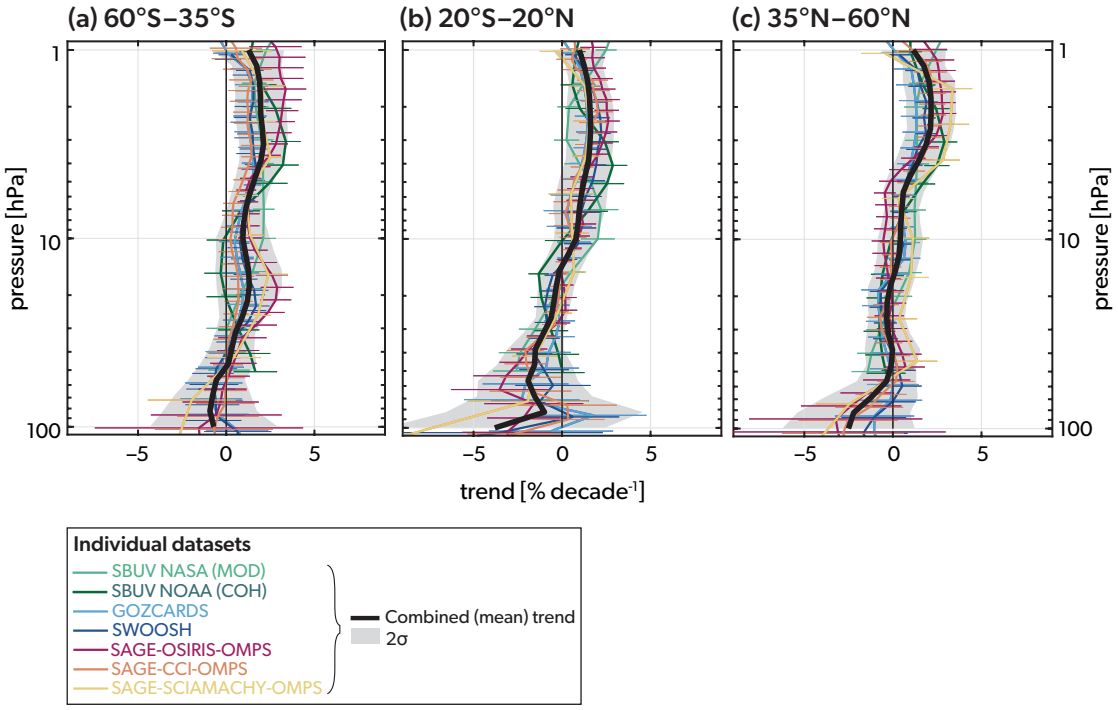


**Figure 3-11.** Ozone profile trends with 2σ uncertainties for the period 2000–2020 for latitude bands 35–60°S *(left panel)*, 20°S–20°N *(center panel)*, and 35–60°N *(right panel)*. Colored lines are the trend estimates from seven individual merged datasets on their original vertical grid (SBUV NASA (MOD), SBUV NOAA (COH), GOZCARDS, SWOOSH, SAGE-OSIRIS-OMPS, SAGE-CCI-OMPS, and SAGE-SCIAMACHY-OMPS). Black lines represent the mean (combined) trends and gray shading indicates the 2σ uncertainty intervals for the combined trends, estimated using the method for combining trends from different observational datasets outlined in SPARC/IO3C/GAW (2019). [Adapted from Godin-Beekmann et al., 2022.]

are also positive but smaller (~1–2% decade$^{-1}$; mean ~1.5% decade$^{-1}$) and are statistically significant for all merged datasets except SBUV MOD. Most datasets indicate negative trends in the lower stratosphere, but all trend estimates, either from individual merged datasets or combined trends, have large uncertainties and therefore are not statistically significant. The estimated trends in these profiles from individual merged satellite datasets agree better with each other than reported in the previous Assessment, resulting in a more robust assessment of vertically resolved trends. Note that the mean trend shown in **Figure 3-11** is a combination of the individually derived satellite trends and is shown with its 2σ uncertainty, estimated in the same way as reported in the last Assessment (see SPARC/IO3C/GAW, 2019). In brief, these uncertainties include both a simple error propagation, which captures uncertainties associated with trend estimates from individual merged datasets, and the standard error of the mean, which captures the spread of trend estimates due to systematic uncertainties, such as those induced by possible drift in some datasets used in the combined products (see *Section 3A.3*).

Comparing the 2000–2020 trend profiles with the 2000–2016 trends from the previous Assessment (from SPARC/IO3C/GAW, 2019), the overall trends are almost identical (**Figure 3-12**). The uncertainties of the mean trend estimates, however, are now smaller at most altitudes. This reduction is mainly due to the additional four years of data available from observations and the fact that the trend estimates from individual merged datasets are now more consistent, as noted above. In addition, the updated trend is based on trends from seven, rather than six, merged satellite data products (Godin-Beekmann et al., 2022).

Multi-model mean trends estimated from the CCMI-1 simulations are very similar to the satellite mean ozone trends in the upper stratosphere (**Figure 3-12**). In the lower stratosphere, the models and observations agree on negative ozone trends in the tropics; in the mid-latitudes, however, the multi-model mean suggests positive ozone trends, whereas the satellite observations indicate negative trends (**Figure 3-12**). However, none of the trends in the lower stratosphere are statistically significant. For more details on the ozone trends in the UTLS, see *Section 3.3.3*. Note that individual model trends are estimated using the ILT regression method and using the same approach as for the satellite data, with the necessary proxies either being calculated directly from the individual model simulations (e.g., QBO, ENSO) or taken from the external forcings provided to the models before they are combined into a multi-model mean.

### *3.3.2.3 Regional and Longitudinally Resolved Trends*

Since the last Assessment, a new development has been to investigate ozone trends at finer spatial and temporal resolutions. In particular, two studies have focused on longitude- and latitude-dependent trends in ozone profiles to obtain a finer

regional perspective. These studies used the longitudinally resolved merged datasets SAGE II-SCIAMACHY-OMPS (Arosio et al., 2019) and MEGRIDOP (Sofieva et al., 2021) and evaluated the trends using the MLR method for the period 2003–2018. Both studies consistently show a strong longitudinal dependence to ozone trends at high and mid-latitudes in the Northern Hemisphere, with a dipole pattern of increasing trends over Scandinavia and decreasing trends over Siberia below 40 km and stronger increasing trends over Scandinavia at 40 and 45 km (**Figure 3-13**). This spatial feature is thought to be related to changes in dynamical processes that are associated with the BDC (see Arosio et al., 2019, and references therein), but this hypothesis has yet to be fully confirmed.

When longitudinally resolved trends are derived from gridded satellite datasets, their magnitude and significance vary with longitude and differ spatially compared to latitude band trends derived from the same datasets (Arosio et al., 2019; Sofieva et al., 2021). This fact calls into question the common practice of using latitude band data to estimate the agreement between vertically resolved trends from satellite data and ground-based records (SPARC/IO3C/GAW, 2019). When compared to their corresponding SBUV zonal means, lidar monthly mean data at different stations show correlations of 0.1 to 0.6 (Zerefos et al., 2018). The trends estimated at individual ground-based stations may not be representative of their respective large latitude bands and may be relevant only on a regional, longitudinally resolved scale in the mid- and lower stratosphere.

Different ground-based observation methods vary in their measurement record length, vertical and temporal sampling, and the spatial distribution of station locations. Trends estimated from these different ground-based records may be more sensitive to regional atmospheric conditions (SPARC/IO3C/GAW, 2019). This can lead to a high variability in trends from ground-based measurements. Disagreements between the trends estimated from collocated measurements can be used to reveal the presence of uncorrected drift in the ground-based records. Consideration of data uncertainties and inhomogeneities in the regression model can affect the resulting trends and improve their consistency, as has been demonstrated for collocated lidar and microwave radiometer measurements (Bernet et al., 2020). If the measurement times are at regular intervals, temporal sampling can be excluded from the factors responsible for trend discrepancies, as has been demonstrated with microwave radiometers (Maillard Barras et al., 2020).

Post-2000 trend profiles derived using MLR (SPARC/IO3C/GAW, 2019) at three selected Network for the Detection of Atmospheric Composition Change (NDACC) locations from different latitude regions are shown in **Figure 3-14**. The selected locations provide measurements from several ground-based instruments at the same station or multiple measurements at nearby stations (Godin-Beekmann et al., 2022). The European "site" combines measurements from the Alpine stations Haute Provence (France; OHP, 43.9°N, 5.7°E), Hohenpeißenberg (Germany; HOH, 47.8°N, 11.0°E), and Arosa (Switzerland; ARO,

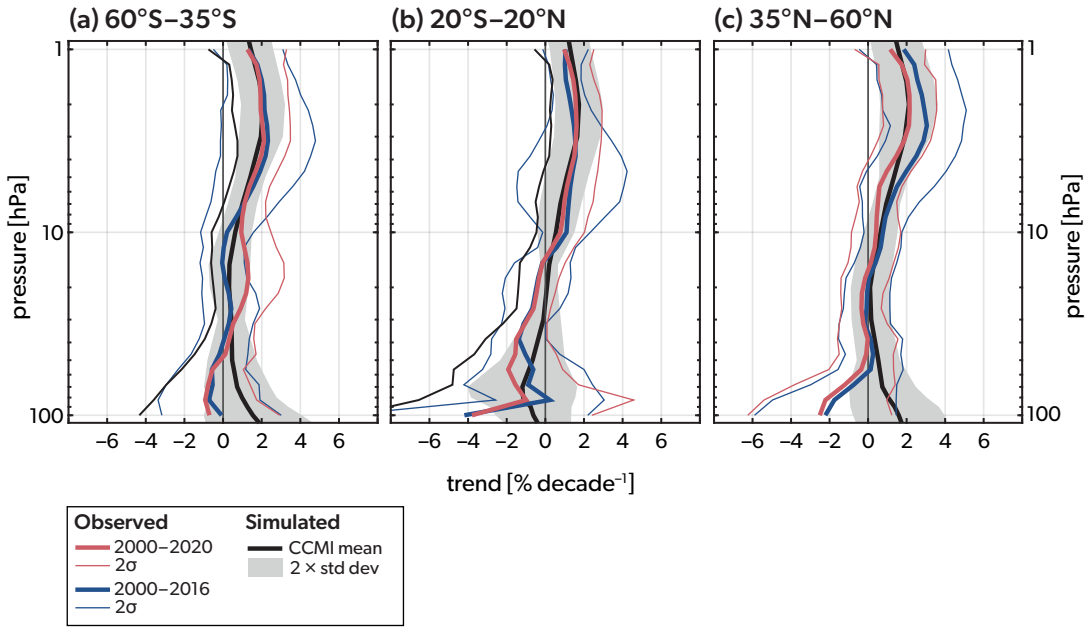


**Figure 3-12.** Comparison of simulated and observed post-2000 ozone trend profiles for the latitude bands 35–60°S *(left panel)*, 20°S–20°N *(center panel)*, and 35–60°N *(right panel)*. Observed trends from the last Assessment (the period 2000–2016) are shown in blue, and results for the updated period 2000–2020 are shown in red, with the trend values based on combining different merged satellite datasets and their 2σ uncertainties, all estimated using the method outlined by SPARC/IO3C/GAW (2019) and as also shown in **Figure 3-11**. The black line is the multi-model mean trend calculated from 16 CCMI-1 REF-C2 simulations (Morgenstern et al., 2017), with the spread of the individual model trends (±2 standard deviations) indicated by the gray shading. [Adapted from Godin-Beekmann et al., 2022.]

46.8°N, 6.9°E). All three stations are located within a single grid cell in the MEGRIDOP, SBUV MOD, and SWOOSH satellite-based datasets. Mauna Loa (Hawai'i, USA; 19.5°N, 155.6°W) and Lauder (New Zealand; 45.0°S, 169.7°E) are single-station sites located in the tropics and the SH mid-latitudes, respectively. For the three locations, the agreement with trends estimated from the gridded satellite datasets is good, taking into account that the SBUV MOD and SWOOSH cells are larger (in longitude) than the MEGRIDOP cells.

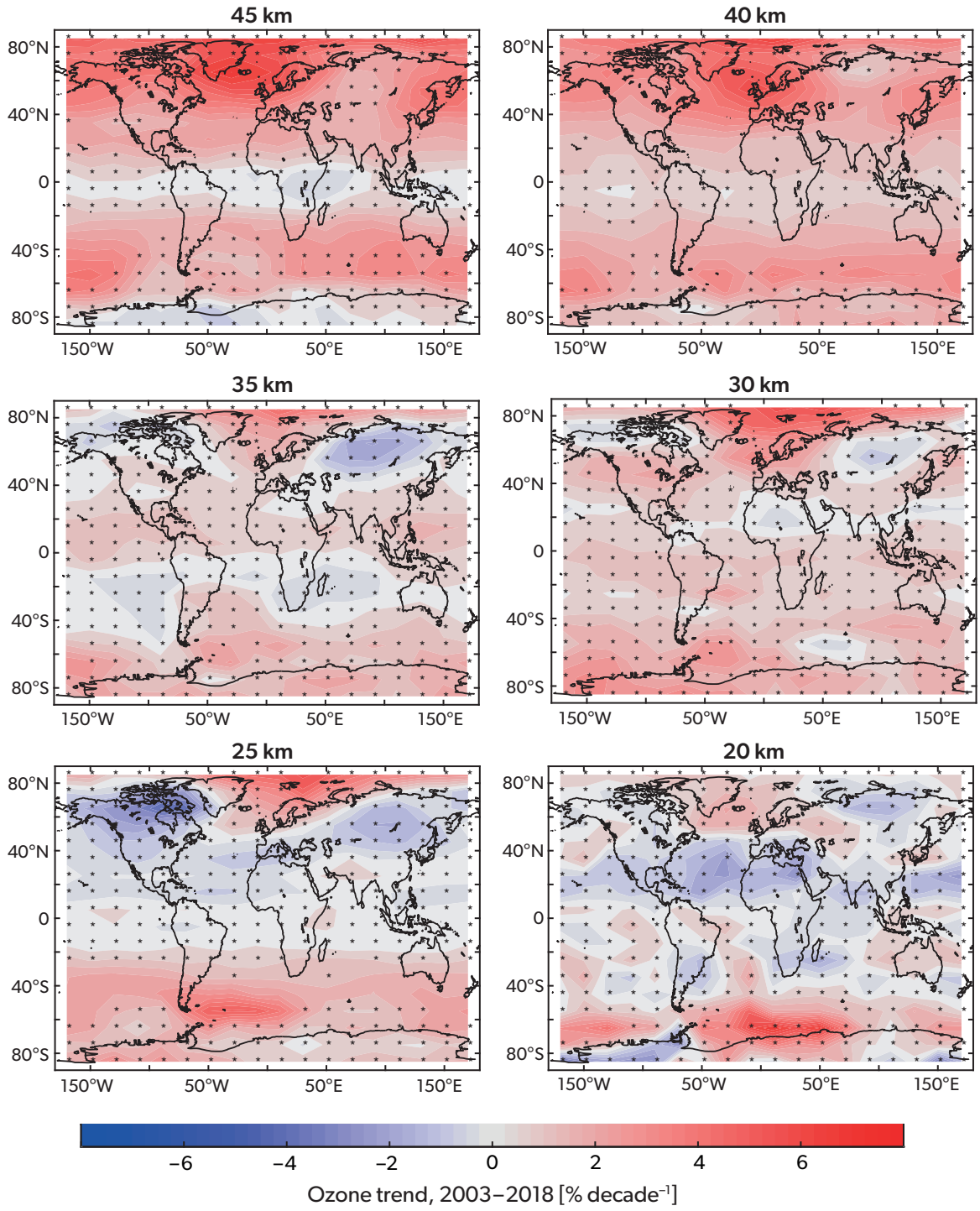


**Figure 3-13.** Latitude- and longitude-dependent ozone trends (% decade$^{-1}$) derived for the period 2003–2018 for six different altitude levels, based on the MEGRIDOP dataset (Sofieva et al., 2021). Gray stars indicate regions where the trends are not statistically significant at the 2σ level. [Adapted from Sofieva et al., 2021.]

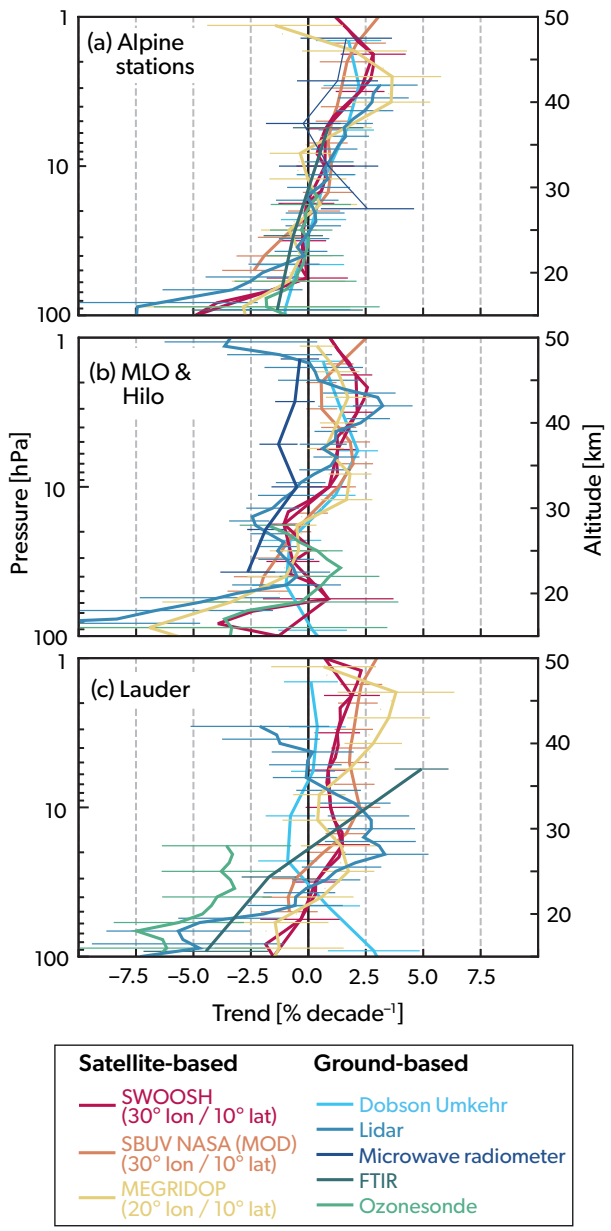


**Figure 3-14.** Ozone trend profiles (% decade$^{-1}$) for 2000–2020 at selected NDACC locations: (a) a European "site" that combines measurements from the Alpine stations Haute Provence (France), Hohenpeißenberg and Zugspitze (Germany), and Jungfraujoch, Payerne and Arosa (Switzerland); (b) a site that combines Mauna Loa (Hawaii, USA; MLO) and Hilo (Japan; just ozonesonde data); and (c) Lauder (New Zealand). Trend profiles are shown for Dobson Umkehrs (light blue), ground-based lidars (medium blue), microwave radiometers (dark blue), FTIR (dark green), and ozonesondes (light green), although not all measurements appear at all locations. Also shown are trend profiles estimated from the SWOOSH (red), SBUV NASA (MOD) (orange), and MEGRIDOP (yellow) gridded satellite products, using the nearest grid boxes. Error bars represent the 95% confidence intervals. [Adapted from Godin-Beekmann et al., 2022.]

The ground-based trend profiles are in general agreement with the gridded satellite trends, within their respective uncertainties (**Figure 3-14**). Disagreements likely reflect inhomogeneities in the different measurement time series that are not properly considered or the need for data curation, which is currently in process. Significant positive trends are found in the upper stratosphere for nearly all datasets, except for four that show negative and non-significant trends. The lower-stratospheric picture is not as clear but is representative of the actual state of our knowledge within that vertical range (see *Section 3.3.3*). Since the last Assessment, the European ozonesondes have been homogenized under the framework of the Tropospheric Ozone Assessment Report Phase 2 (TOAR II) project (*Section 3A.2*), and, within uncertainties, their trends show agreement with the trend of the gridded satellites and the collocated ground-based instruments (**Figure 3-14**). Although the comparison of ground-based trends at the three selected NDACC locations and longitudinally resolved satellite trends is made at a more appropriate spatial resolution than with broad zonal-mean bands derived from satellite data, the overall conclusion is the same for both comparisons: trend profiles from ground-based measurements and satellite data agree within the limits given by the different spatial representations and the homogeneity problems of the datasets.

The seasonal dependence of ozone trends in the stratosphere has been examined in a new study using four long-term merged satellite datasets in three broad-latitude bands (60–30°S, 10°S–10°N, 30–60°N; Szeląg et al., 2020). All four datasets show qualitatively similar trends, although there are some minor differences, mostly in trend magnitude (**Figure 3-15**). In the upper stratosphere, the 2000–2018 trends are positive throughout all seasons and most latitudes. The largest upper-stratospheric ozone trends are observed in the mid-latitudes during local winter in the Northern Hemisphere (up to 6% decade$^{-1}$) and at the equinoxes in the Southern Hemisphere (up to 3% decade$^{-1}$). In the equatorial region, there is a very strong seasonal dependence of ozone trends at all altitudes: the trends are negative in the upper stratosphere during boreal winter (−1 to −2% decade$^{-1}$) and in the lower stratosphere during boreal spring (−2 to −4% decade$^{-1}$), while the mid-stratosphere (30–35 km) has positive trends in boreal spring (2 to 3% decade$^{-1}$) and negative trends (–0.5 to –2% decade$^{-1}$) in boreal fall. The tropical trends below 25 km are negative and maximize during summer (up to −2% decade$^{-1}$) and spring (up to −3% decade$^{-1}$). There is a hemispheric asymmetry in the mid-latitude lower stratosphere (Szeląg et al., 2020): during local summers and equinoxes, positive trends are observed in the Southern Hemisphere (1–2% decade$^{-1}$), while negative trends are observed in the Northern Hemisphere (–1% to –2% decade$^{-1}$). A comparison of the seasonally dependent ozone trends with available analyses of the seasonally dependent stratospheric temperature trends reveals a positive correlation (trends in the same direction) in the dynamically controlled lower stratosphere and negative correlation (trends in opposite directions) above 30 km, where photochemical processes dominate.

### *3.3.2.4 Consistency of Total Column Ozone Trends and Partial Column Trends*

In past Assessments, trends in TCO have been a gauge of the efficacy of the Montreal Protocol in halting stratospheric ozone layer losses. Since 1998–2000, the previous rapid decline in TCO, which had been primarily driven by stratospheric ozone losses,

has halted. However, it is only now that significant increases in TCO are being detected, and only at some latitudes (*Section 3.3.1* and **Figure 3-6**). Since the last Assessment, there have been further investigations into the contribution of different vertical regions to TCO trends, particularly the contribution of tropospheric changes (see **Box 3-3**). Overall, these findings raise questions about whether TCO is the best metric for determining ozone recovery in the context of the Montreal Protocol.

Stratospheric ozone represents ~90% of the total column, but it may no longer reflect the bulk of the long-term changes. Although analyses of some satellite datasets indicate a decline in tropospheric ozone since the early 2000s (e.g., some analyses shown by Gaudel et al., 2018), several estimates of tropospheric ozone changes conservatively suggest increases of ~1.5 DU decade$^{-1}$ (~5% of the tropospheric column) globally since the early 2000s (Ball et al., 2018; Ziemke et al., 2019; Gaudel et al., 2018, 2020), and this is supported by modeling studies (Zhang et al., 2016, 2021). Where TCO changes match or are smaller than the tropospheric ozone trends (*Section 3.3.1*), post-2000 stratospheric column ozone changes may be zero or even negative. For example, focusing on observations at Irene, South Africa (~26°S), one recent study found that local TCO increases may be driven by tropospheric increases (Bencherif et al., 2020). Separating stratospheric ozone trends into partial column components isolates stratospheric trends. Such analyses indicate that the magnitude and significance of post-2000 ozone increases in the upper stratosphere (above 32 km) are strengthening with additional years (Ball et al., 2019a; *Sections 3.3.2.2* and *3.3.2.3*).

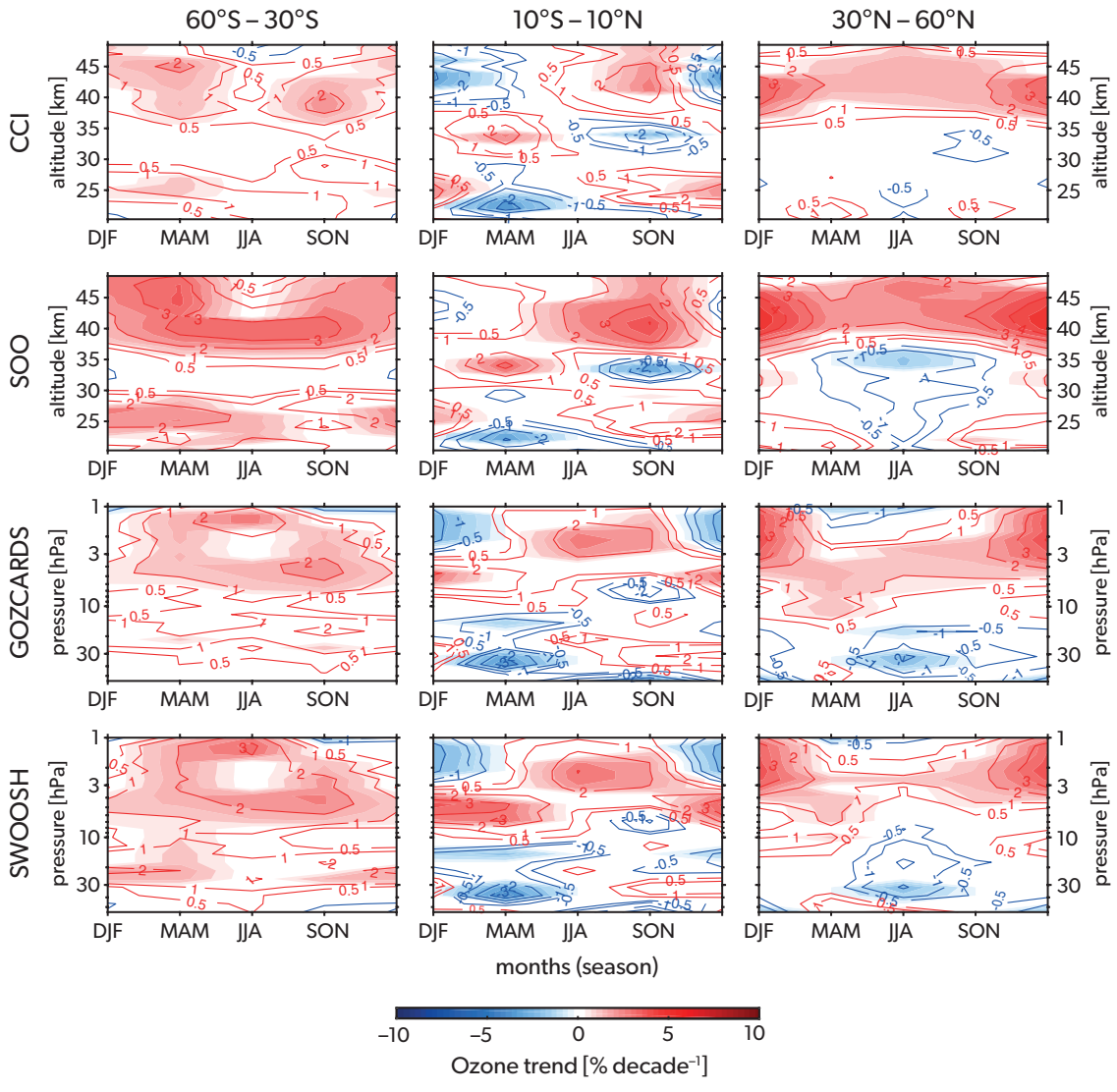


**Figure 3-15.** Altitude-season variation of linear trends for four merged ozone datasets (top to bottom, SAGE II-CCI-OMPS [CCI], SAGE II-OSIRIS-OMPS [SOO], GOZCARDS, and SWOOSH) calculated over the period 2000–2018 for three selected latitudinal bands (left to right, 60–30°S, 10°S–10°N, and 30–60°N). Data are presented on their natural vertical coordinate: altitude grid for CCI and SOO and pressure grid for GOZCARDS and SWOOSH. The colored shading denotes where the trends are significant at the 95% confidence level. [From Szeląg et al., 2020.]

## *Box 3-3. The Importance of the Troposphere for Total Column Ozone*

A key conclusion of this Assessment is that it is more difficult than in the past to interpret total column ozone (TCO) changes due to the different trends and processes that contribute to the overall column. In particular, the contribution from tropospheric ozone changes is highlighted for both current (*Section 3.3.2.4*) and future (*Section 3.4.3*) total column trends, despite the modest contribution (~10%) of the tropospheric column to the total amount of ozone in the column.

Production of ozone in the stratosphere results from the photolysis of molecular oxygen ($O_2$) and subsequent reaction of atomic oxygen with $O_2$. In contrast, tropospheric ozone is produced from photochemical reactions involving its precursors, nitrogen oxides (NO and $NO_2$; $NO_x$), carbon monoxide (CO), and volatile organic compounds, with an additional source from net stratosphere-to-troposphere transport. It is lost through additional chemical reactions as well as through deposition at the surface (e.g., Monks et al., 2015). Tropospheric ozone levels depend on highly temporally and spatially variable natural and anthropogenic precursor emissions, different local surfaces that impact dry deposition rates, and tropospheric weather. There are substantial challenges in fully understanding its distribution and changes using both measurements (Gaudel et al., 2018; Tarasick et al., 2019) and simulations (Young et al., 2018). Community efforts such as the Tropospheric Ozone Assessment Report (TOAR) are improving our understanding, while also making previously unpublished measurements available (Schultz et al., 2017). Community modeling efforts (e.g., CCMI; Morgenstern et al., 2017) also seek to evaluate models and better characterize and understand their deficiencies.

Despite these difficulties, models demonstrate skill in comparisons against observations, reproducing the tropospheric ozone burden, distribution, and trends (e.g., Young et al., 2018; **Box 3-3 Figure 1**). Model studies of the historical period (1850–present) find that increases in anthropogenic precursors have dominated the simulated ~30–35% increase in tropospheric ozone (e.g., Young et al., 2013; Griffiths et al., 2021), which is consistent with the 40% change inferred from ice core–based constraints (Yeung et al., 2019). Between 1980 and 2000, the same simulations suggest a ~5% increase in tropospheric ozone, broadly in agreement with observational constraints (Gaudel et al., 2018) and occurring at the same time as the most notable ODS-driven stratospheric ozone depletion. Since 2000, there have been spatially heterogeneous trends in precursor emissions and, consequently, tropospheric ozone (Zhang et al., 2016; Gaudel et al., 2018, 2020; Zhang et al., 2021). This complicates our understanding and interpretation of both the overall tropospheric trends and those of TCO.

Projected future changes in tropospheric ozone strongly depend on the future scenario of precursor emissions and, to a lesser degree, on the projected state of stratospheric ozone and climate (see **Box 3-1 Figure 1**; Stevenson et al., 2013; Young et al., 2013; Griffiths et al., 2021; see also *Section 3.4.3*). Because current and future tropospheric ozone changes may contribute substantially to TCO changes, or offset stratospheric ozone changes (Ball et al., 2018; Bencherif et al., 2020), they must be considered as an integral part of this Assessment.

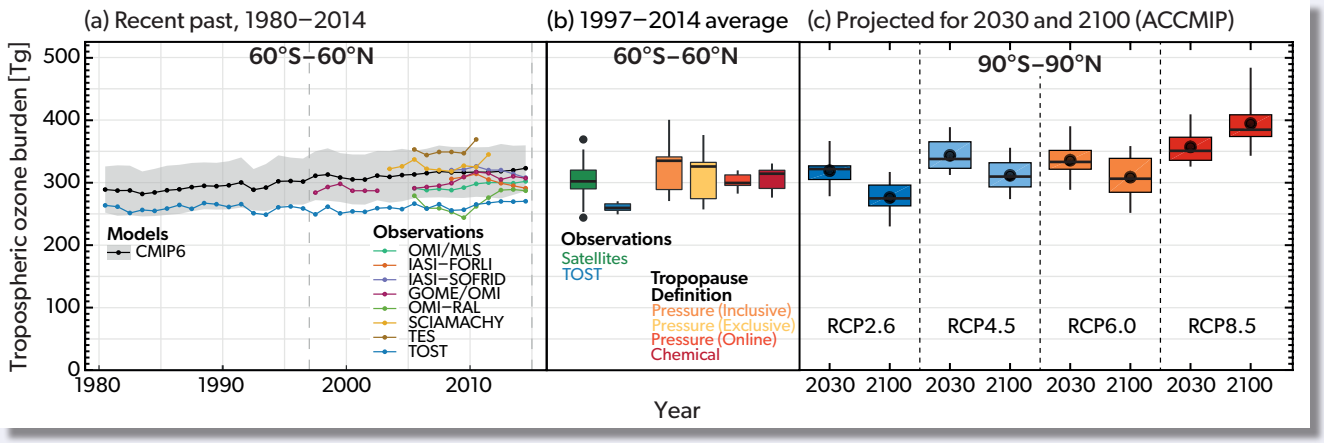


**Box 3-3 Figure 1.** The evolution of the global tropospheric ozone burden in simulations (1980–2100) and observations (1980–2014), showing (a) a comparison of the CMIP6 models (black; see **Box 3-4**) against observational estimates (colored lines) for 1980–2014, (b) a comparison of the 1997–2014 average tropospheric ozone burden in observations (green and blue boxes) and simulations (orange, yellow and red; with different definitions of the tropopause), and (c) the projected tropospheric ozone burden from the ACCMIP simulations (Lamarque et al., 2013) for 2030 and 2100 time slices for four different future climate scenarios (the Representative Concentration Pathways [RCPs]). [Adapted from Young et al., 2013 and Griffiths et al., 2021; see those references for further details.]

Partial column trends do not always show strong agreement with those derived from highly resolved vertical profiles, especially in terms of significance. This is primarily due to the poorly characterized small-scale and/or short-term variability in regression analyses (*Section 3.2*) that contribute to larger trend uncertainties. These issues become more pronounced for trends derived at higher vertical resolutions since vertical integration averages out some variability (*Section 3.3.3*), particularly if the partial columns are chosen for that purpose. On the other hand, if the vertical integration is performed over the entire column, a significant detection at some finer-resolution vertical levels may be averaged out if trends of opposite sign are present within the column integration. There can also be complications in integrating resolved data into partial columns (such as how data gaps are dealt with). There are few analyses investigating the consistency of TCO with respect to its partial column components in a holistic way.

### 3.3.3 Understanding Trends in the UTLS Region

Since the previous Assessment, additional observations and new CCM simulations have furthered our understanding of trends in the upper troposphere / lower stratosphere (UTLS) region, with a focus on the tropics (30°S–30°N) and SH and NH mid-latitudes (30–60°). The overall conclusion, discussed in detail below, is that ozone is decreasing in the tropical UTLS, consistent with understood changes in the stratospheric circulation. At mid-latitudes, the picture is more complex. Ozone is decreasing in the mid-latitudes, but 1) this trend has a magnitude and significance that is not consistent across different datasets and time periods, 2) the trend is not generally captured in chemistry-climate model (CCM) simulations, and 3) there is no clear consensus as to what might be driving it. Trends in the UTLS are difficult to assess due to high variability and the fact that there are only two decades of data available. Additionally, the quality of satellite-based observations is usually substantially reduced in the UTLS region compared to the middle and upper stratosphere, while ground-based observations, which do have good data in this region, provide only sparse coverage.

Findings and trends for the tropical lower stratosphere remain consistent with the previous Assessment. This region consistently displays significant, or near-significant, negative trends between the start years of ~1995–2000 and end years of 2013–2019 (Dietmüller et al., 2021; see also **Figure 3-16**). Modeling studies indicate these negative trends are to be expected, as tropical upwelling in the BDC strengthens in response to increasing greenhouse gases (Eyring et al., 2010; Dhomse et al., 2018; see also *Section 3.4* and *Chapter 5*), as reported in previous Assessments. This finding is further supported by a recent analysis of ozonesonde data, which found that ozone trends became insignificant after accounting for changes in tropopause height, suggesting that chemical ozone loss is not a driving factor in long-term changes in this region (Thompson et al., 2021). Separately, a recent model study of the 2016 Indonesian wildfires suggests that tropical UTLS ozone reductions can result from such events due to the gas-phase chemistry of reactive volatile organic compound emissions, although the magnitude of the effect is dependent on model assumptions (Rosanka et al., 2021). Trends and variability in the tropical UTLS are particularly important since this region is a large contributor to quasi-global (60°S–60°N) lower-stratospheric ozone changes.

The mid-latitude lower-stratospheric ozone declines over 1998–2016 reported in the last Assessment (Ball et al., 2017, 2018; Wargan et al., 2018) persist with additional years of data (**Figure 3-16**), both for analyses that are spatially resolved and for partial columns (Dietmüller et al., 2021). While temperature trends, which are expected to change alongside ozone, support this tendency of the ozone trends (Ball et al., 2020; Szeląg et al., 2020), the lower stratosphere is subject to large, dynamically driven interannual variability, and it remains difficult to make robust conclusions. Indeed, earlier studies using fewer data and with end years prior to 2017 also show a decline of ozone in this region, although in those cases the trend is not statistically significant (Bourassa et al., 2014, 2018; Sofieva et al., 2017; Steinbrecht et al., 2017). Trends are sensitive to large variability in the analyzed data, especially near the end of short time series, although

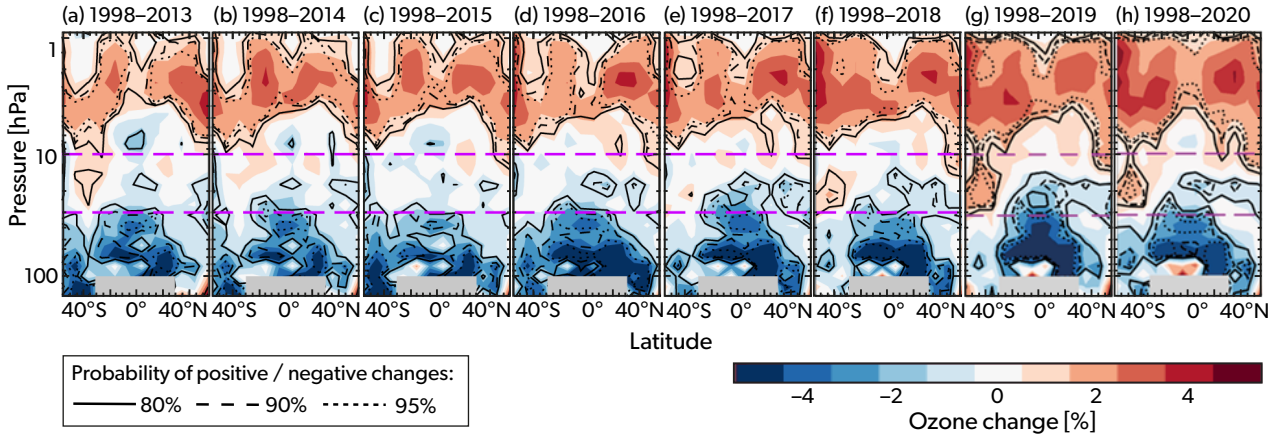


**Figure 3-16.** Zonal-mean ozone trends using the BASIC dataset (which is based on the GOZCARDS and SWOOSH datasets) starting in 1998 and finishing in years ranging from 2013 to 2020, moving from (a) to (h). Red regions indicate an ozone increase, while blue regions indicate a decrease. Confidence levels in the trends are indicated by solid (80%), dashed (90%), and dotted (95%) lines. [Updated from Ball et al., 2019a.]

the negative trends across the lower stratosphere are persistent even when the end years (**Figure 3-16**) and start years (Dietmüller et al., 2021) are varied. For instance, the large year-on-year ozone increase between 2016 and 2017 in the mid-latitude SH UTLS has been found to fully (Chipperfield et al., 2018) or partially (Ball et al., 2019a) offset the negative ozone trend over 1998–2016. Extended into 2018, the ozone changes in the SH lower stratosphere remain negative but become statistically insignificant (Ball et al., 2019a). Besides large short-term dynamical variability, natural variability (e.g., related to sea surface temperatures) can interfere on interannual (Rosanka et al., 2021) and decadal (Garfinkel et al., 2013; Ball et al., 2020; Iglesias-Suarez et al., 2021) timescales. Both timescales are relevant to understanding the limited observational period and future projections.

Since the previous Assessment, new studies of multiple ozone datasets (Ball et al., 2019a) and CCM simulations (Orbe et al., 2020) have explored the hemispheric pattern in the mid-latitude UTLS ozone trends in more detail. These have demonstrated that lower-stratospheric ozone in the Southern Hemisphere appears to display larger interannual variability than in the Northern Hemisphere, which is partly why trend significance there remains low. Negative changes in the Northern Hemisphere are both more persistent and have smaller uncertainties than in the Southern Hemisphere, although they are still statistically non-significant. The relative contributions of changes in mixing versus circulation to NH lower-stratospheric ozone changes remain an open question. While a model-based tracer budget analysis (over 1998–2018) found that decreases in NH ozone are primarily associated with changes in the meridional transport (poleward expansion of tropical upwelling and reduced downwelling in the northern subtropical region; Orbe et al., 2020), changes in meridional mixing are also important (Wargan et al., 2018; Ball et al., 2020; Orbe et al., 2020). However, it is worth noting that even recent studies that have made use of historical CCM runs with accurate real-world (e.g., sea surface temperature) variability only cover up to 2010 or 2014 (e.g., Orbe et al., 2020), which means comparisons of models with observations beyond this year are problematic.

A different approach to using CCM output is to examine the distribution of trends across an ensemble of free-running simulations, i.e., those where the long-term drivers of ODSs and greenhouse gases are the same but are unconstrained by observed interannual variability. However, statistical analysis of mid-latitude UTLS ozone trends across 31 such CCMI-1 simulations demonstrates that the observed trends represent an extreme value of the CCM probability distribution, indicating that it is between ~75% and 96% probable that the models are not capturing the mid-latitude lower-stratospheric changes (**Figure 3-17**; Dietmüller et al., 2021). Similarly, negative trends were found in both the tropics and mid-latitudes up to present day in only 2 out of 13 models that contributed to the older CCMVal-2 report (Ball et al., 2020). Moreover, simulated mid-latitude lower stratosphere trends remain positive even after accounting for variations in the start and end years (Dietmüller et al., 2021). There is a possibility that the lack of negative mid-latitude lower-stratospheric trends in the models is related to weaker-than-observed tropical BDC trends in climate models (Ball et al., 2020; Orbe et al., 2020; see also Stone et al., 2018).

Finally, we note that there is a spread among the UTLS ozone trends calculated for the available datasets. Most of the results

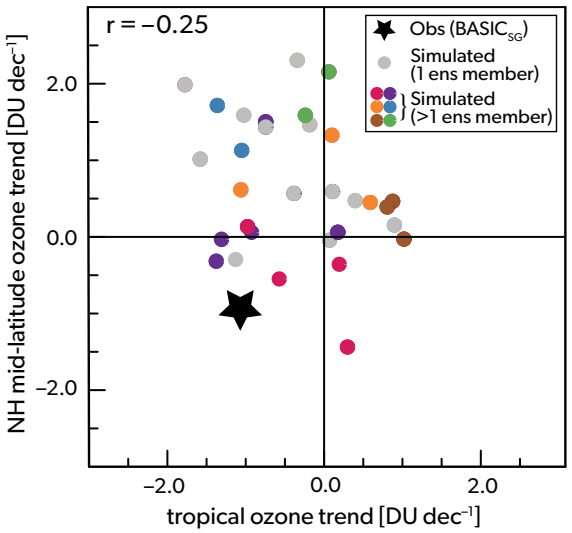


**Figure 3-17.** Scatter plot of lower stratosphere ozone column trends for the NH mid-latitudes (30–50°N; 150–30 hPa) against the tropics (20°S–20°N, 100–30 hPa) calculated over the period 1998–2018 for observations from the BASICSG dataset (star; Ball et al., 2018) and 31 CCMI REF-C2 simulations (circles; Morgenstern et al., 2017). All ensemble members of a particular model are shown in the same color, whereas simulations with only one ensemble member are shown in gray. Also shown is the correlation between the tropical and NH mid-latitude trends in the simulations. [Adapted from Dietmüller et al., 2021.]

discussed here have relied on observational data from SWOOSH and GOZCARDS, which are constructed using similar underlying satellite data, or on the BASIC dataset, which integrates both of these (Ball et al., 2017, 2018; Chipperfield et al., 2018; Wargan et al., 2018; Ball et al., 2020; Dietmüller et al., 2021; *Section 3A.3*). However, there is not consistency between trends from partial columns with those calculated from resolved profiles, particularly with respect to uncertainties, which are larger in the resolved profiles (SPARC/IO3C/GAW, 2019; Weber et al., 2020; **Figures 3-11** and **3-12**; *Section 3.3.2.4*). It should be emphasized that as data are ever more resolved (vertically, spatially, and/or temporally), higher uncertainties are expected (see *Section 3.3.2.4*), and confidence and consistency with more spatially and temporally smoothed partial columns will decrease (**Figures 3-11** and **3-12**; Bourassa et al., 2018; Arosio et al., 2019; SPARC/IO3C/GAW, 2019; Szeląg et al., 2020; Sofieva et al., 2021; Weber et al., 2021).

## 3.3.4 Past Ozone in Models and Trend Attribution

Since the previous Assessment, the latest generation of climate models (including some CCMs) have performed new simulations as part of the Coupled Model Intercomparison Project Phase 6 (CMIP6) experiment (Eyring et al., 2016), conducted in support of the Intergovernmental Panel on Climate Change. CMIP6 defines some simulations that are aimed at either identifying the drivers of past changes or exploring future changes under different emissions scenarios (see **Box 3-4** and *Section 3.4.1*).

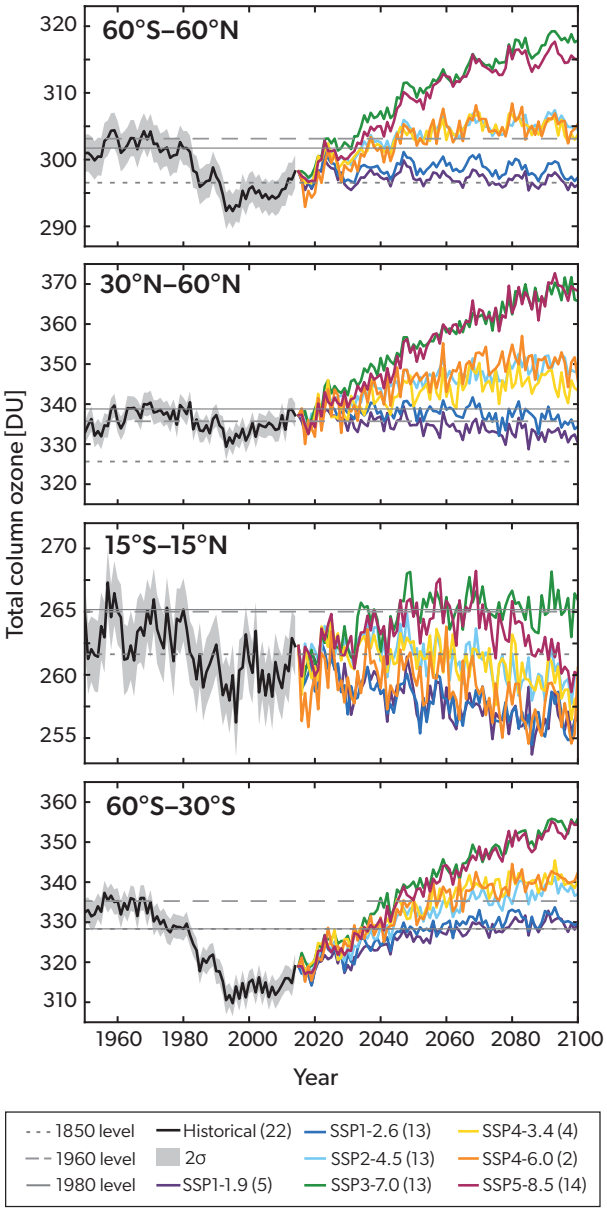


**Figure 3-18.** CMIP6 multi-model mean, annual mean TCO projections for the historical simulation (black line) and different shared socioeconomic pathways (SSPs; colored lines; see **Box 3-4**) for different latitude bands: near global (60°S–60°N), NH mid-latitudes (30–60°N), tropics (15°S–15°N), and SH mid-latitudes (60–30°S). The light gray envelope indicates the 95% confidence interval for the multi-model mean for the historical simulations. Simulated TCO values for the 1850, 1960, and 1980 annual means are given by the dotted, dashed, and solid horizontal gray lines, respectively. The number of models performing each simulation is provided in parentheses in the legend. Many of the models provided ozone output for a core set of SSPs (SSP1-2.6, SSP2-4.5, SSP3-7.0, and SSP5-8.5), while a smaller number provided data for other SSPs (SSP1-1.9, SSP4-3.4, and SSP4-6.0). [Adapted from Keeble et al., 2021a.]

### *3.3.4.1 Past Ozone in Models*

The individual CMIP6 models span a range of model complexity, from models using interactive chemistry schemes to calculate ozone changes within the model (i.e., in response to changing chemical and physical conditions) to those using a time-evolving ozone field from a pre-prepared dataset (i.e., where the ozone does not interact with the simulation). While the prescribed ozone field is from the same source for all models in the latter category, it is not implemented consistently, with the result that different models have different TCO values (Keeble et al., 2021a).

In contrast to the CCMI-1 simulations (Dhomse et al., 2018) discussed in the last Assessment, which started in 1960, the CMIP6 simulations extend back to 1850. This allows additional exploration of several decades preceding ozone depletion, which can be used to benchmark simulated future changes. In terms of long-term changes in TCO, the simulated near-global (60°S–60°N), annual multi-model mean increases by ~2% between 1850 and 1960 (Keeble et al., 2021a) before rapidly declining through the 1980s and 1990s due to emissions of halogenated ODSs (**Figure 3-18**). TCO reaches a minimum in the late 1990s before increasing again as ODS levels decrease.

Simulated TCO changes for different latitude bands are similar to those for the near-global mean (**Figure 3-18**), although the 1850–1960 ozone increase (not shown) is larger in the Northern Hemisphere and tropics and less prominent in the Southern Hemisphere. This difference is driven by simulated increases in NH tropospheric ozone between the preindustrial period (1850) and present day, as seen in the changes in zonal-mean ozone mixing ratios (**Figure 3-19**; see also *Section 3.3.4.3* and **Box 3-3**; Griffiths et al., 2021; Keeble et al., 2021a). While stratospheric ozone levels have decreased between the preindustrial and present day, particularly in the upper stratosphere and Antarctic polar lower stratosphere due to changes in chlorine-catalyzed ozone depletion, tropospheric ozone has significantly increased during this same period (**Figure 3-19**; Tarasick et al., 2019; Yeung et al., 2019). The impact of these combined changes is that despite stratospheric ozone depletion linked to ODS emissions, the simulated NH mid-latitude TCO is higher in the 1990s than in the preindustrial period (**Figure 3-18**). Although the simulated increase remains to be validated against (the very limited) available observations (e.g., Rieder et al., 2010), this nonetheless highlights the problem of using TCO as a metric for stratospheric ozone changes (see **Box 3-3** and *Sections 3.3.2.4* and *3.4.2*).

TCO over 1980–2014 is ~10 DU higher in the CMIP6 multi-model mean compared to observations when all models are included (Keeble et al., 2021a). Using only those models that explicitly simulate chemical processes, bias-correcting their TCO (to the 1964–1980 average) and then smoothing it using an 11-point boxcar filter (as per Dhomse et al., 2018), the observed TCO trend (**Figure 3-20**) is well captured by the multi-model mean in the 60°S–60°N region and in the mid-latitudes. It is less well captured in the tropics (see also *Section 3.3.3*). Good agreement has also been shown for TCO trends over the period 1979–2000 between the multi-model mean of CMIP6 models that use interactive chemistry schemes and observations at most latitudes (Morgenstern et al., 2020). However, for some locations, there is a large spread in the simulated ozone trends between individual models, and our understanding of the reasons behind this is currently lacking (see also the discussion in *Section 3.4.1*).

## Box 3-4. Models and Scenarios: CMIP6 and SSPs

Coordinated model intercomparison projects are a key method for bringing information from multiple model simulations and research groups into climate and ozone assessments. This Assessment makes use of the Coupled Model Intercomparison Project Phase 6 (CMIP6), an international activity that consists of a suite of climate model experiments designed to explore the impacts of past and future emissions changes on the long-term evolution of the Earth system (Eyring et al., 2016).

Of particular interest to this Assessment are the CMIP6 historical simulations, as well as sensitivity simulations performed for the Aerosol Chemistry Model Intercomparison Project (AerChemMIP; Collins et al., 2017) and the projections performed for the Scenario Model Intercomparison Project (ScenarioMIP; O'Neill et al., 2016). The ScenarioMIP simulations use a new set of future climate scenarios, the Shared Socioeconomic Pathways (SSPs; Riahi et al., 2017). SSPs replace Representative Concentration Pathways (RCPs) explored in the previous Assessment but serve the same purpose: to provide a range of future emissions scenarios that assume different socioeconomic trajectories and different levels of climate change mitigation. SSP5-3.4-OS is slightly different from the others in that it is an "overshoot" scenario, following the SSP5-8.5 (high climate forcing) scenario until 2040, with aggressive mitigation thereafter. This scenario informs the Assessment in *Chapter 6*.

Compared to the RCPs, the SSPs explore a much wider range of possible future emissions pathways for well-mixed greenhouse gases, such as $CO_2$ (carbon dioxide), $N_2O$ (nitrous oxide), and $CH_4$ (methane), in addition to changes to the emissions of near-term climate forcers (NTCFs), which include tropospheric ozone precursors and aerosols (Gidden et al., 2019). For long-lived halogenated ozone-depleting substances (ODSs), all SSPs assume compliance with the Montreal Protocol and its Amendments and adjustments. However, as models are run with surface mixing ratios as input, rather than emissions, the levels of ODSs do differ marginally between SSPs due to the impacts of different climate trajectories on their lifetime (see also *Chapter 4*). Finally, hydrofluorocarbons (HFCs; *Chapter 2*) differ more markedly between SSPs than do controlled ODSs, as each scenario has different compliance rates with the Kigali Amendment (Meinshausen et al., 2020).

**Box 3-4 Table 1.** Description of the relevant CMIP6 simulations discussed in this Assessment report (GHGs = greenhouse gases, ODSs = ozone-depleting substances, NTCFs = near-term climate forcers, SSTs = sea surface temperatures, SICs = sea ice concentrations).

| Simulation Name(s) | Type | Purpose | Features |
|---|---|---|---|
| historical | Hindcast simulation of the period 1850–2014 | To produce realistic simulations of the past atmospheric state | GHGs, ODSs, volcanic aerosol, solar variability, ozone, and aerosol precursors are prescribed from observations. Uses a coupled ocean model for SSTs and SICs |
| histSST | Historical atmosphere-only transient simulation of the period 1850–2014 | Control experiment for AerChemMIP historical perturbation experiments | As "historical," but with SSTs and SICs prescribed from the "historical" experiment rather than using a coupled ocean model. |
| histSST-piNTCF<br>histSST-piCH4<br>histSST-piN2O<br>histSST-1950HC | Series of historical atmosphere-only transient perturbation simulations of the period 1850–2014 based on histSST | To assess the impact of NTCFs, $CH_4$, $N_2O$, and halocarbon (HC) emissions on the past evolution of atmospheric composition and climate change | As histSST, but with either NTCF, $CH_4$, or $N_2O$ emissions held at their preindustrial ("pi") levels, or with HCs held at their 1950 levels, while all other emissions evolve as in "historical" |
| SSP1-1.9<br>SSP1-2.6<br>SSP2-4.5<br>SSP3-7.0<br>SSP4-3.4<br>SSP4-6.0<br>SSP5-8.5<br>SSP5-3.4-OS | Future simulations of the period 2015–2100 | To produce estimates of future atmospheric composition and climate changes given specific emissions assumptions. Named for the radiative forcing level by 2100 (1.9 $Wm^{-2}$, 2.6 $Wm^{-2}$, etc.) | GHGs, ODSs, volcanic aerosol, ozone, and aerosol precursors are prescribed following the named SSP scenario (SSP1-1.9, etc.); uses coupled ocean model for SSTs and SICs |

The CMIP6 models span a range of complexity, particularly with regard to the simulation of atmospheric chemistry. In contrast to phase 1 of the Chemistry Climate Model Initiative (CCMI-1; Morgenstern et al., 2017), which was used extensively in the last Assessment and includes exclusively those models with interactive chemistry schemes, CMIP6 includes both models with interactive chemistry and those that prescribe ozone fields from a shared dataset. As a result, there is a smaller number of CMIP6 models suitable for exploration of ozone return dates (*Section 3.4.1*) than have been shown in previous Assessments. However, these models have performed simulations following a larger number of potential future emissions pathways.

All of the relevant CMIP6 simulations are described in detail in **Box 3-4 Table 1**, coupled with **Box 3-4 Figure 1** showing the evolution of surface concentrations for selected long-lived greenhouse gases for different SSPs.

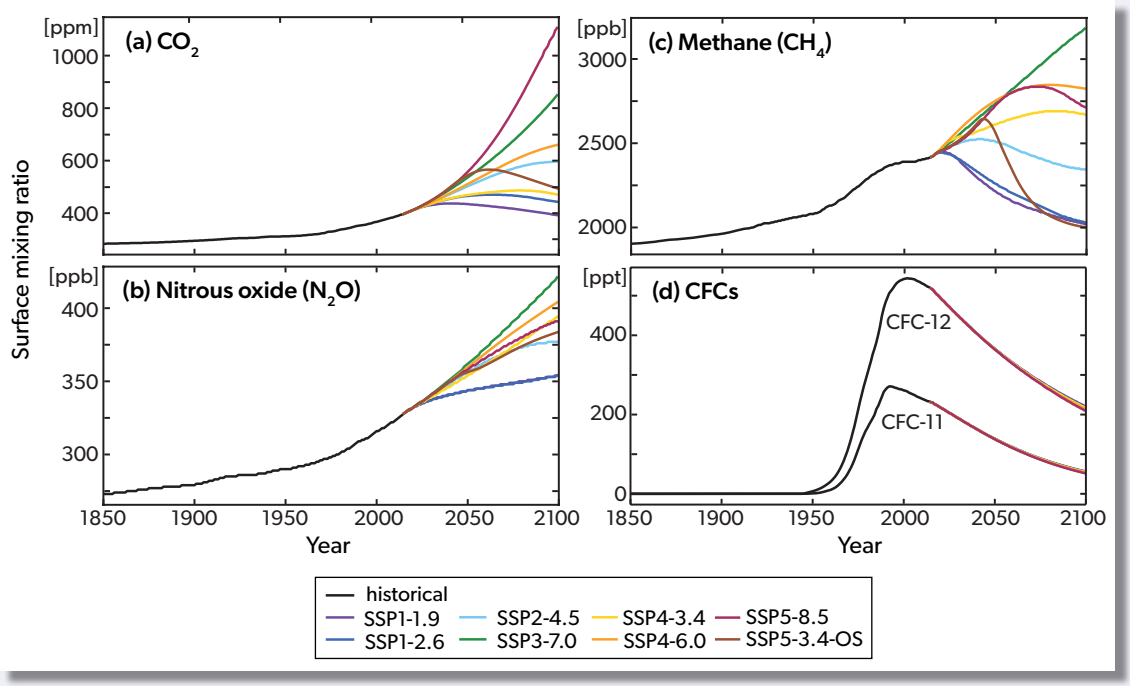


**Box 3-4 Figure 1.** Evolution of the surface mixing ratios of (a) carbon dioxide ($CO_2$; in parts per million, ppm), (b) nitrous oxide ($N_2O$; in parts per billion, ppb), (c) methane ($CH_4$; in parts per billion, ppb), and (d) the ODSs CFC-11 and CFC-12 (in parts per trillion, ppt) from 1850–2100 for the historical period (black lines) and within different SSPs (colored lines). CFC-11 and CFC-12 surface mixing ratios differ between scenarios but only marginally. See **Box 3-4 Table 1** for more information.

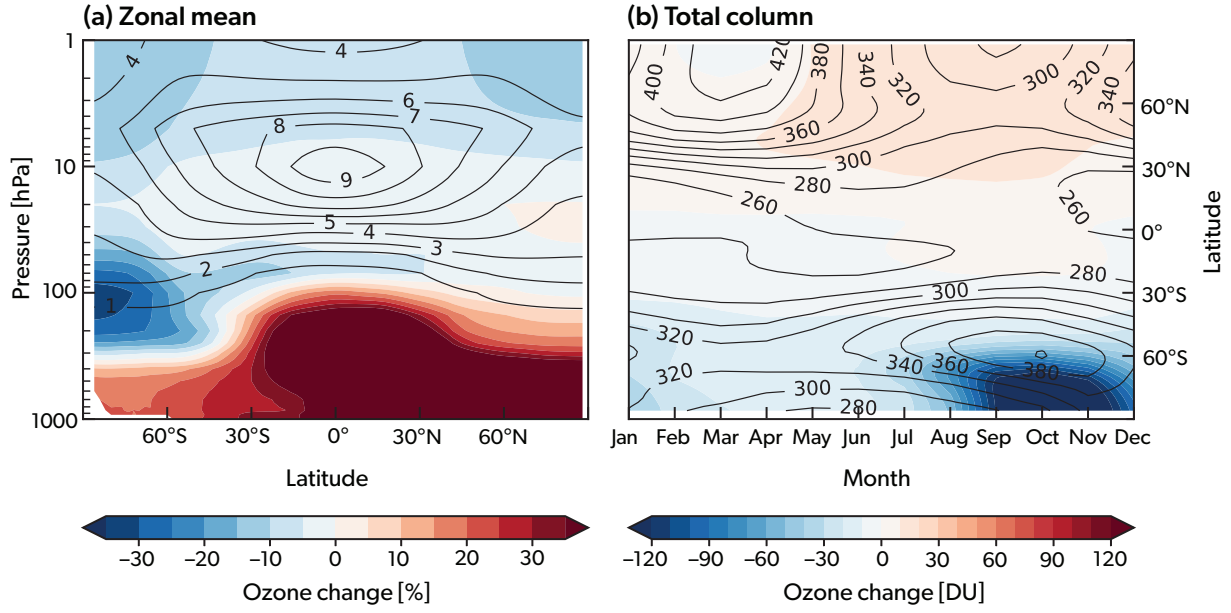


**Figure 3-19.** Simulated changes in ozone from the preindustrial (1850–1864 average) to present day (2000–2014 average) for the CMIP6 multi-model mean. Color fills show (a) the change in annual and zonal-mean ozone mixing ratios (%) and (b) the change in monthly and zonal-mean TCO (DU). Black contour lines in each panel show the present-day climatology as (a) mixing ratio (ppm) and (b) DU. [Adapted from Keeble et al., 2021.]

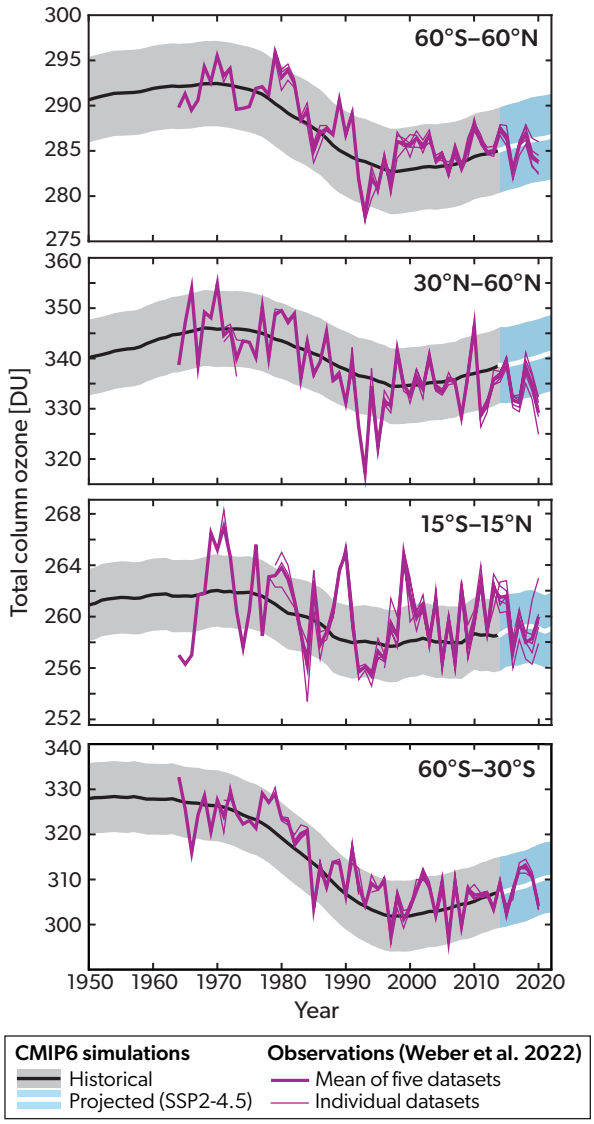


**Figure 3-20.** TCO for the CMIP6 multi-model mean from 1950 to 2022 (historical to 2014 in black and then extended with SSP2-4.5 in white; see **Box 3-4**) and the five individual observational datasets from **Figure 3-6** (thin purple lines) and their mean (thick purple line) from 1964–2020. Data shown are annual mean values for four different latitude bands: near global (60°S–60°N), NH mid-latitudes (35–60°N), tropics (20°S–20°N), and SH mid-latitudes (60–35°S). The CMIP6 multi-model mean is calculated as an unweighted mean of the five CMIP6 models available that include interactive chemistry schemes. Each model is first bias corrected to the observations averaged over the period 1964–1980, before being smoothed with an 11-point boxcar smoothing. The gray and light blue envelopes show the spread between the individual models that make up the CMIP6 multi-model mean and are calculated as the ±1 standard deviation of the bias-corrected, smoothed model values, averaged 1850–2100 excluding the years 1954–1990, during which time the model variance becomes artificially low due to the bias correction step. [Adapted from Keeble et al., 2021a.]

### 3.3.4.2 Simulated Impacts of Very Short-Lived Substances

Chlorine and bromine from very short-lived substances (VSLSs; halogenated ozone-depleting substances with lifetimes shorter than six months) contribute to ozone depletion, particularly in the lower stratosphere, where their present-day contribution may be up to half as large as that from long-lived ODSs (e.g., Hossaini et al., 2015; see also *Chapter 1*). Overall, while model sensitivity experiments show that the contribution of past trends in short-lived chlorine species to recent ozone changes is small (e.g., Chipperfield et al., 2018; see also *Section 3.3.3*), the long-term impact of continued VSLS increases on stratospheric ozone recovery remains to be quantified (see also Barrera et al., 2020).

Although VSLSs are not routinely included in all CCMs, the previous Assessment reported how simulations of recent ozone changes can be improved by the inclusion of VSLSs. Since the last Assessment, model studies have sought to quantify the amount of chlorine and bromine from VSLSs in the stratosphere, including highlighting the important role of transport to the stratosphere in the Asian summer monsoon (Adcock et al., 2021). One modeling study estimated that the total amount of stratospheric chlorine from VSLSs has increased from 69 ± 14 ppt in 2000 to 111 ± 22 ppt in 2017 (Hossaini et al., 2019). Due to decreases in long-lived ODSs over the same period, the increase in chlorine from VSLSs has led to their relative contribution to total stratospheric chlorine, increasing from ~2% in 2000 to ~3.4% in 2017. Another CCM study (Barrera et al., 2020) found that brominated VSLSs account for 8 DU (3%), 2.5 DU (1%), and 5.5 DU (2%) additional ozone loss for the SH mid-latitudes, tropics, and NH mid-latitudes, respectively. The same study also noted that the inclusion of 5 ppt biogenic bromine results in a realistic stratospheric bromine loading and improves the agreement between the modeled and observed mid-latitude TCO over the period 1980–2015, consistent with previous findings (Sinnhuber and Meul, 2015).

### 3.3.4.3 Attributing Drivers of Past Ozone Changes

New sensitivity simulations from the Aerosol and Chemistry Model Intercomparison Project (AerChemMIP; Collins et al., 2017), part of CMIP6 (**Box 3-4**), can be used to attribute past ozone changes to a broader range of individual drivers than was possible using the CCMI-1 models in the last Assessment. These drivers include emissions of non-methane near-term climate forcers (NTCFs; precursors of tropospheric ozone and aerosol; lifetimes <10 years), methane ($CH_4$), nitrous oxide ($N_2O$), and halogenated ODSs. AerChemMIP also includes simulations over a longer historical time period (1850–2014 versus 1960–2014). The individual roles of changes in NTCFs, $CH_4$, $N_2O$, and halogenated ODSs on historical ozone column changes can be determined by contrasting the AerChemMIP sensitivity simulations (with individual forcing agents held at their preindustrial levels) against an "all-forcing" simulation, where all forcings evolve (histSST; **Box 3-4**; Zeng et al., 2022). In contrast to the seven CCMI-1 models in the previous Assessment, there are only between three and five AerChemMIP models with suitable output to assess the contributions of the different drivers.

In close agreement with the CMIP6 simulations (**Figure 3-18**), the all-forcing multi-model mean of the four AerChemMIP models with interactive stratospheric and tropospheric chemistry

shows a gradual increase of near-global mean TCO during ~1900–1970, mainly due to the increase in tropospheric ozone (**Figure 3-21**). TCO decreases rapidly after the 1970s until the late 1990s, when stratospheric ozone depletion dominates its decrease in all regions. The largest decrease occurs in the SH mid-latitudes. However, in the NH mid-latitudes and the tropics, the continuous increase of the tropospheric ozone column from the 1950s contributes to long-term TCO changes, offsetting the reduction in stratospheric ozone in these regions. The model spread is particularly large in the stratospheric ozone changes that contribute to the uncertainty in TCO changes, particularly in mid-latitudes.

As in previous Assessments, the sensitivity simulations—where individual forcing agents are turned off—can be used to quantify the roles of individual drivers in ozone trends. These runs reveal the dominant role of ODS-induced stratospheric ozone depletion for the global TCO decrease from the 1970s to the late 1990s (**Figure 3-22**). During this ozone depletion period, individual models differ substantially in simulating the stratospheric ozone response to ODS increases; this is the main cause of large intermodel differences in the simulated TCO trend. In contrast, tropospheric column ozone increases can be attributed to the monotonic increases in NTCFs and $CH_4$ (**Box 3-4 Figure 1**), particularly from the 1950s to the late 1990s. NTCFs contribute to TCO increases largely through increased tropospheric columns (**Box 3-3**), particularly in the tropics and the NH mid-latitudes. Methane contributes to total column increases both through the tropospheric column (as a tropospheric ozone precursor) and the stratospheric column (through its reaction with chlorine, which reduces ozone depletion from ODSs), particularly in the mid-latitudes over 1970–2000. The impact of increased $N_2O$ is to decrease TCO through its role as an ODS in the stratosphere, even though it increases ozone in the tropical lower stratosphere (due to "self-healing," arising from increased UV fluxes as a result from a depleted ozone layer aloft), consistent with the CCMI-1 models (Morgenstern et al., 2018; **Figure 3-22**). Note, this impact is estimated based on only three AerChemMIP models, as the other two did not perform the relevant simulations, and there is a large model spread and large interannual variation.

No simulations directly targeted the impact of carbon dioxide ($CO_2$) increases on ozone, but this can be estimated from the residual of the other effects, i.e., the difference between the impact from all forcings (histSST) and the combined impact from the other single-forcing perturbations (NTCFs, $CH_4$, halogenated ODSs, and $N_2O$), although only for the three models with the required simulations. The impact of $CO_2$ on simulated TCO is dominated by changes in the stratospheric partial columns (**Figure 3-22**). This includes a slight increase in stratospheric column ozone prior to the 1970s due to $CO_2$-induced stratospheric cooling (*Chapter 5*), which reduces stratospheric ozone loss, mainly in the NH mid-latitudes, and a sharp decrease after the late 1970s, when ODSs increase and stratospheric cooling leads to enhanced ODS-driven ozone depletion. However, this approach of deriving the impact of $CO_2$ is associated with large uncertainties, as it involves several simulations and cannot account for couplings between forcing agents.

These sensitivity simulations can also be used to attribute the drivers of vertically resolved ozone trends (**Figure 3-23**). In agreement with previous Assessments, the simulated negative trend in stratospheric ozone is predominantly driven by ODSs during the depletion period (1979–1999). Both the trend

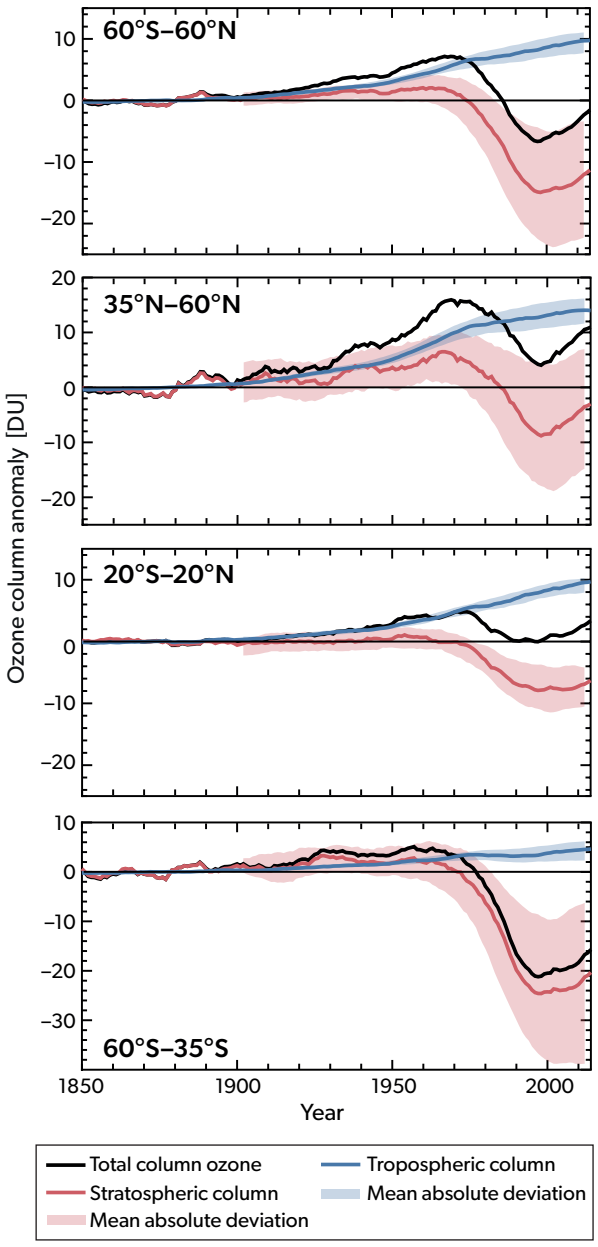


**Figure 3-21.** Annual multi-model mean TCO (black) and the stratospheric (red) and tropospheric (blue) partial column ozone anomalies (relative to 1850–1900 base period) for 1850 to 2014 from the AerChemMIP histSST simulation (**Box 3-4**), for the near-global mean (60°S–60°N), NH mid-latitudes (35–60°N), the tropics (20°S–20°N), and the SH mid-latitudes (60–35°S). Four models (CESM2-WACCM, GFDL-EM4, MRI-ESM2-0, and UKESM1-0-LL) are included in the ensemble, and the shaded areas are the mean absolute deviation from the multi-model mean. The annual means are smoothed using a 20-year boxcar filter. For the partial columns, the tropopause is defined using the WMO lapse rate definition in each model. [Adapted from Zeng et al., 2022.]

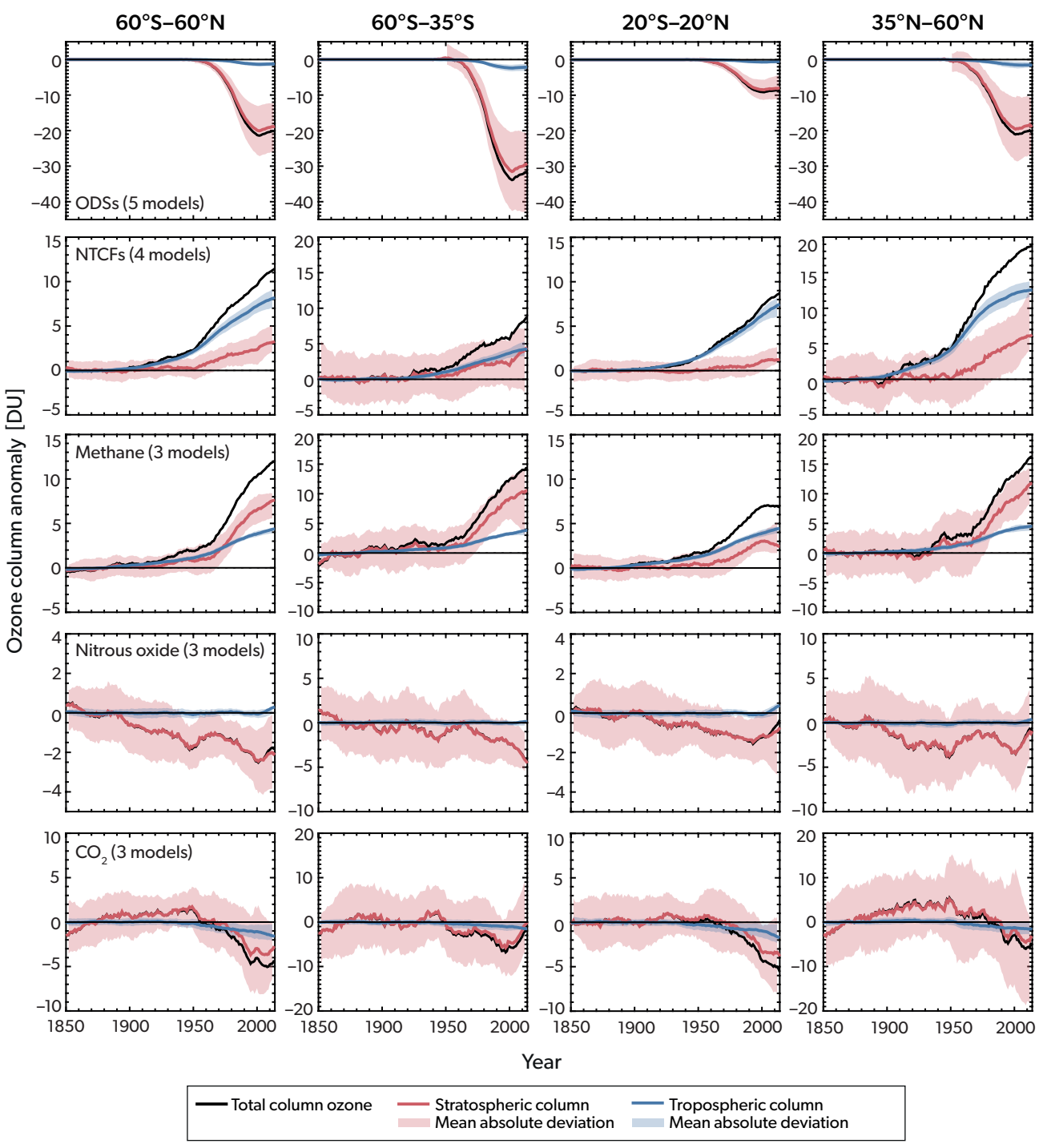


**Figure 3-22.** Attribution of total column (black), stratospheric column (red), and tropospheric column (blue) ozone changes to *(top to bottom)* halogenated ODSs, near-term climate forcers (NTCFs), methane ($CH_4$), nitrous oxide ($N_2O$), and carbon dioxide ($CO_2$), shown *(left to right)* for the near-global (60°S–60°N), SH mid-latitude (60–35°S), tropical (20°S–20°N), and NH mid-latitude (35–60°N) means. Time series are the smoothed annual mean (20-year boxcar filter) AerChemMIP multi-model mean deviation of ozone columns from their preindustrial values (1850–1900). Except for $CO_2$, the impact of each forcing (X) on ozone is calculated by subtracting a simulation with a forcing held fixed at the preindustrial level (histX) from one where all forcings evolve (histSST – histX; **Box 3-4**). The impact of $CO_2$ is derived from subtracting the sum of all single-forcing perturbations (i.e., ODSs, NTCF, $CH_4$, and $N_2O$) from the all-forcing (histSST) simulation. Shaded areas are the mean absolute deviations from the multi-model mean. The tropopause is defined by the WMO lapse rate definition. [Adapted from Zeng et al., 2022.]

in ozone and its attribution to ODSs are significant at the 95% confidence level throughout the SH mid-latitudes, a large part of the NH mid-latitudes, and above 20 hPa in the tropics. Methane ($CH_4$) plays a significant role in driving the positive ozone trend in the mid-latitude middle to upper stratosphere and in the tropical upper stratosphere. The combined impact of $N_2O$ and $CO_2$ on ozone is predominantly negative and is significant (at the 95% confidence level) in the middle stratosphere over the NH mid-latitudes and the upper tropical stratosphere. The net impact of greenhouse gases (GHGs) on stratospheric ozone during that period is largely insignificant (at the 95% confidence level) due to the opposing effects of $CH_4$ versus that of $CO_2$ and $N_2O$.

Between 2000 and 2014, the ozone trends from the all-forcing simulation are largely positive and significant in the upper stratosphere, due mainly to the decline in ODSs. The individual forcings do not result in any significant trends in stratospheric ozone due to the brevity of the simulation period and a large model uncertainty. The increase in GHGs as well as declining ODSs drive the positive ozone trend in the middle to upper stratosphere (**Figure 3-23**), in agreement with the last Assessment. The trend in ozone in the middle and upper stratosphere due to $CH_4$ increases is negative during this period (although generally not significant at the 95% confidence level), reflecting a coupling with now decreasing ODSs.

In the lower stratosphere, the ozone trends due to all forcings and individual forcings are masked by large dynamical

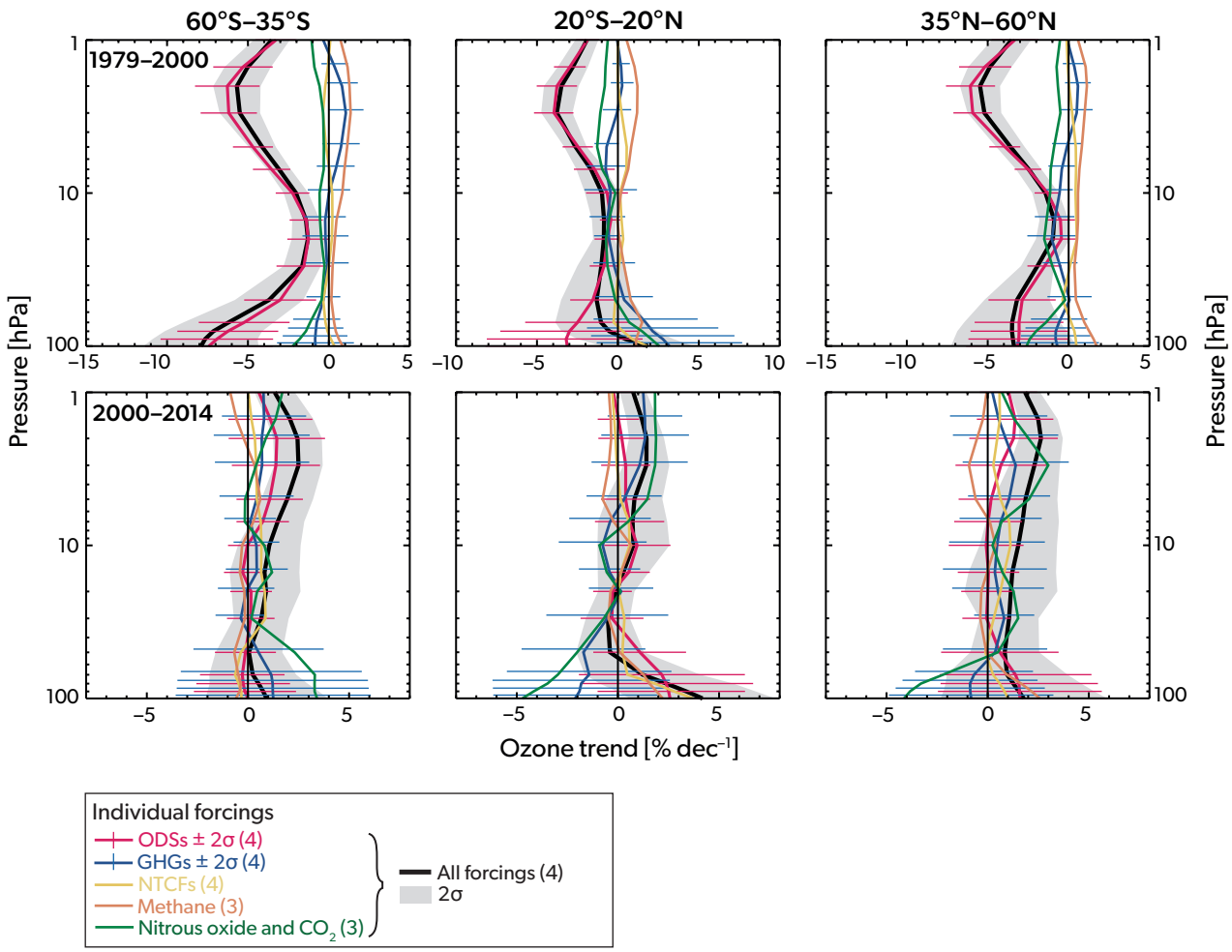


**Figure 3-23.** Attribution of stratospheric ozone trends along a vertical profile as a function of pressure as simulated by the AerChemMIP models, for *(left to right)* SH mid-latitudes (60–35°S), tropics (20°S–20°N), and NH mid-latitudes (35–60°N), calculated over the periods *(top panels)* 1979–1999 and *(bottom panels)* 2000–2014. The black lines show the vertically resolved trends in the multi-model mean ozone from the histSST simulation (**Box 3-4**), which includes all forcings, with the 2σ uncertainty range shaded in gray (accounting for statistical and model uncertainty). Colored lines show the contributions to the trends from ODSs (red), the combined greenhouse gases ($CO_2$, $N_2O$, and $CH_4$; dark blue), NTCFs (yellow), $CH_4$ (orange), and combined $N_2O$ and $CO_2$ (green). The 2σ uncertainty ranges are indicated for ODSs and combined greenhouse gases as error bars. The impact from the combined greenhouse gases is derived by subtracting the impact from ODSs and NTCFs from the all-forcing histSST simulation. Numbers in parentheses next to the labels are the number of the models included in the ensemble. [Adapted from Zeng et al., 2022.]

variability, as was shown for the CCMI-based results presented in the last Assessment. Although the ozone trend due to all forcings here is small and insignificant, contributions from individual forcings are much larger, but there is some offsetting and cancellation between them. The increase in $CO_2$ drives a strengthening of the BDC (*Sections 3.3.3* and *3.4*; see also *Chapter 5*), which leads to an ozone reduction in the tropical lower stratosphere. Meanwhile, the increases in NTCFs, $CH_4$, and $N_2O$ lead to lower-stratospheric ozone increases mainly through chemical processes, although this is outweighed overall by the impact of $CO_2$ on the circulation. Significant trends in ozone occur only in the lowermost tropical stratosphere, driven by NTCF increases over this period.

## 3.4 PROJECTED OZONE CHANGES

While past changes in ozone can be evaluated using a combination of observations and models, detailed projections of ozone rely on simulations performed using chemistry–climate models (CCMs). This section discusses future ozone recovery, including its impacts on the troposphere, using new simulations that have become available since the last Assessment. The ozone impact of potential future supersonic and hypersonic transport is discussed in *Section 4.3.5.3*, as this issue is most relevant for polar ozone.

### 3.4.1 Model Projections and Their Uncertainty

CCMs provide projections of ozone recovery under different future emissions scenarios, often as part of a coordinated, multi-model activity where the different models follow the same protocols to perform a comparable set of simulations (**Box 3-4**). As in the previous Assessment, three types of uncertainty for these future ozone projections can be considered: internal variability of the climate system (sometimes called "weather noise"); structural uncertainty from the way the models are built, with the result that different models may not respond consistently to identical inputs; and scenario uncertainty, which is the spread in simulated atmospheric composition and climate from following different scenarios. The relative importance of these uncertainties varies at different spatial and temporal scales and for different variables (Hawkins and Sutton, 2009, 2010). Analysis from an earlier model intercomparison project (Charlton-Perez et al., 2010) indicates that, compared to scenario uncertainty, internal variability and structural uncertainty are larger drivers of uncertainty in global ozone projections over the first two-thirds of this century. Typically, the spread in model results from these two uncertainties is reduced by simple averaging across ensemble members to form a multi-model mean. While this potentially reduces the uncertainty from internal variability (assuming there is no bias in that quantity), a simple unweighted mean does not account for known differences in model skill across the ensemble (e.g., Dhomse et al., 2018). Statistical methods have been demonstrated to account for variable model skill in projections of stratospheric ozone (Amos et al., 2020), but these methods have not been assessed outside the polar regions, and additional evidence is required to evaluate best practices (see also **Box 3-1**).

Scenario uncertainty is outside the control of the models and arises from the ultimately unknowable future trajectories of greenhouse gas (GHG) and pollutant emissions and the societal changes that underpin them (although there is considerable debate as to what futures are "likely"; e.g., Hausfather and Peters, 2020). Since the last Assessment, CMIP6 model simulations following a new set of future emissions scenarios, the Shared Socioeconomic Pathways (SSPs), have been run (see **Box 3-4**). All these scenarios assume future compliance with the Montreal Protocol and its Amendments and adjustments, meaning that the future emissions of controlled ozone-depleting substances (ODSs) are the same across the SSPs. At the same time, the SSPs cover a range of future changes in well-mixed GHGs (such as $CO_2$, $N_2O$, and $CH_4$) and near-term climate forcers (NTCFs, which include precursors to tropospheric ozone and aerosols; Gidden et al., 2019). It is well known that projections of total column ozone (TCO) are sensitive to the emissions of these species (e.g., Dhomse et al., 2018; Morgenstern et al., 2018). However, the SSPs necessarily represent only a limited number of trajectories, excluding, for instance, future unregulated emissions of ODSs banned by the Montreal Protocol (*Section 3.4.4*), future very short-lived substance (VSLS) emissions (*Section 3.3.3.2*), volcanic eruptions (*Section 3.2.1.3*), hydrogen emissions from a future where hydrogen plays a large role as an energy source (*Chapter 1*), future supersonic and hypersonic transport (*Chapter 4*), and the impacts of stratospheric climate interventions (*Chapter 6*).

Finally, there are no standard simulations targeted at understanding and characterizing the response of CCMs to idealized ODS emissions, allowing comparison between different models and between different multi-model experiments (cf. the $2\times CO_2$ simulations that form part of the so-called DECK experiments in CMIP; Meehl et al., 2014). This hampers our ability to compare projected ozone and ozone recovery metrics across different assessments, as the scenarios are refined or changed.

### 3.4.2 Total Column Ozone and Expected Return to 1980 Levels

The simulated evolution of 21$^{st}$-century annual mean TCO strongly depends on the SSP scenario and latitude band considered (**Figure 3-18**; Keeble et al., 2021a). For scenarios with stabilizing or slightly declining GHG levels (SSP2-4.5, SSP4-3.4, and SSP4-6.0), near-global mean (60°S–60°N) TCO is projected to return to mid/late-20$^{th}$ century levels by the middle of the 21$^{st}$ century and remain at those levels until 2100. For scenarios with continued GHG increases (SSP3-7.0 and SSP5-8.5), near-global TCO is projected to return to mid/late-20$^{th}$ century levels sooner and significantly exceed these levels throughout the latter half of the 21$^{st}$ century. In contrast, despite the assumption that halogenated ODSs will continue to decline throughout this century, near-global TCO is not projected to return to mid/late-20$^{th}$ century levels under scenarios with the strongest GHG and NTCF mitigation (SSP1-1.9 and SSP1-2.6) due to the NTCF-driven reductions in tropospheric ozone.

A long-standing milestone on the road to ozone recovery is the year at which TCO is projected to return to 1980 values. Only the five CMIP6 models that include interactive chemistry schemes are used for the calculation of the TCO return dates discussed here, since their ozone fields are consistent with both the future emissions scenario and internal model dynamical fields. This is a relatively small number of models compared to that used in the previous Assessment, which drew on the projections from 19 models, meaning that here structural uncertainty is under sampled. On the other hand, this Assessment presents return dates for four scenarios (SSP1-2.6, SSP2-4.5, SSP3-7.0, and SSP5-8.5)

as opposed to the one from the last Assessment (RCP6.0). Each scenario assumes the same future emissions of species regulated under the Montreal Protocol and its subsequent amendments, and so any difference in return dates between scenarios is due to the impacts of other emitted species, such as GHGs and tropospheric ozone precursors.

TCO return dates are calculated following the approach used in the previous Assessment (and described in detail by Dhomse et al., 2018). In brief, the individual CMIP6 models are first bias-corrected to match the observations (in this case the NIWA-BS dataset; Bodeker et al., 2020) averaged over 1980–1984. They are then smoothed with an 11-point boxcar filter to reduce internal variability. The bias-corrected, smoothed time series for each of the five models are then averaged together to give a single multi-model mean time series for each SSP scenario. The return date is defined as the first time this multi-model mean TCO reaches an annual mean value equal to or higher than the 1980 TCO value. Uncertainty estimates for the return dates are given by the first and last times at which the ±1 standard deviation envelope (calculated from the individual model time series) crosses the 1980 TCO value. The process is illustrated in **Figure 3-24a**, which shows two hypothetical TCO projections: one where TCO recovers rapidly and exceeds the 1980 value by the end of the century (FastRecovery), and another where TCO recovers slowly and only slightly exceeds the 1980 value (SlowRecovery). Both

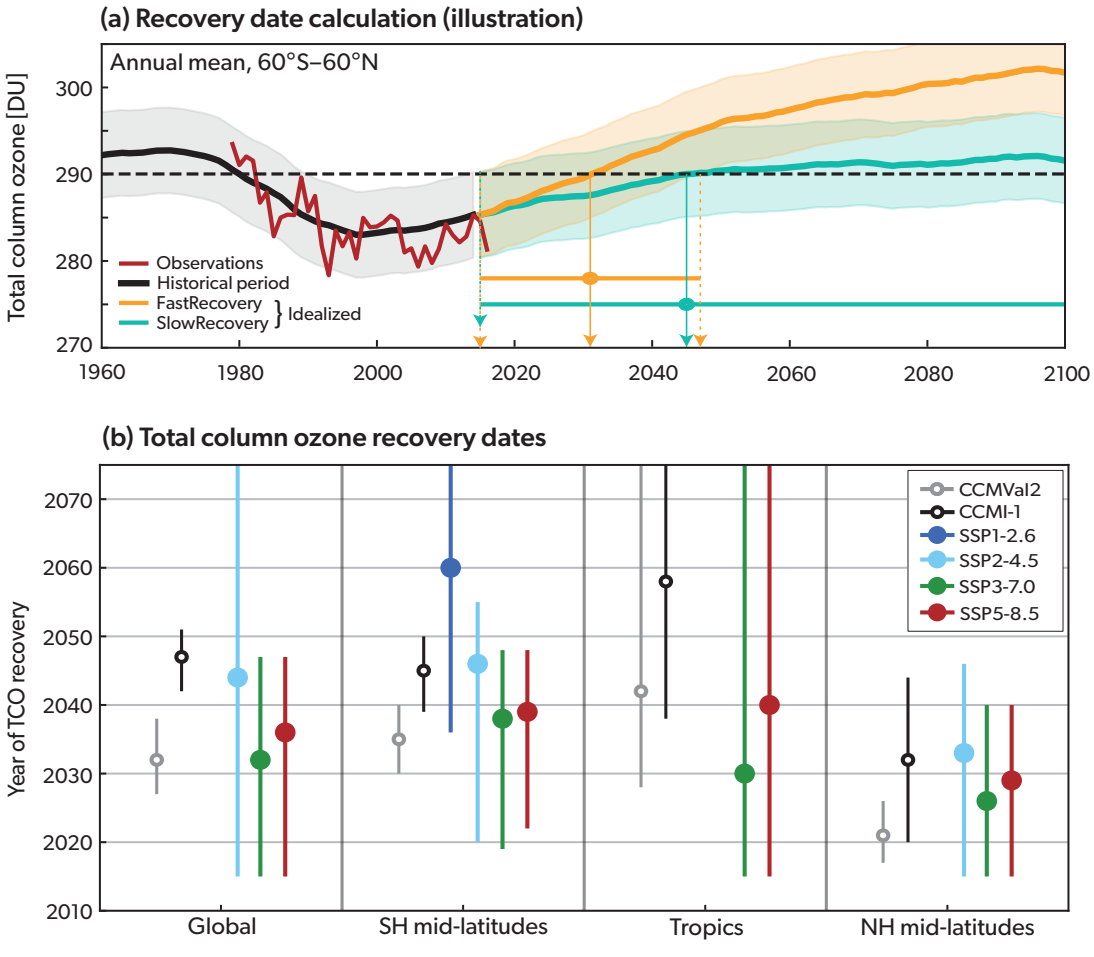


**Figure 3-24.** Year at which TCO recovers to its 1980 value. (a) Recovery date and error bar calculation for two different idealized scenarios of ozone recovery: FastRecovery (yellow) and SlowRecovery (green). The recovery date is when the multi-model mean (thick lines) meets the 1980 value (arrows with solid lines; 1980 value indicated by dashed black line), with the upper and lower bounds of its uncertainty corresponding to when, respectively, the top and bottom of the 1 standard deviation envelope (from the spread of the individual means; indicated by shading) also meet the 1980 value (arrows with dotted lines). (b) TCO recovery dates for different latitude bands and for four SSPs, calculated using five CMIP6 models (thicker lines, solid circles; uncertainty indicated by bars calculated as per panel [a]), as well as models from the CCMVal2 (SPARC, 2010) and CCMI-1 (Morgenstern et al., 2017) experiments (thinner lines, unfilled circles; error bars for CCMI-1 as per SSPs, whereas CCMVal-2 are the 95% confidence interval based on the individual model simulations), as shown in the previous Assessment and documented by Dhomse et al. (2018). The multi-model mean TCO does not return to its 1980 value by 2100 for the global, tropics, and NH mid-latitudes for SSP1-2.6, and for the tropics for SSP2-4.5. Global return dates are calculated using data averaged from 60°S–60°N for the CCMI-1 and SSP simulations and from 90°S–90°N for CCMVal2.

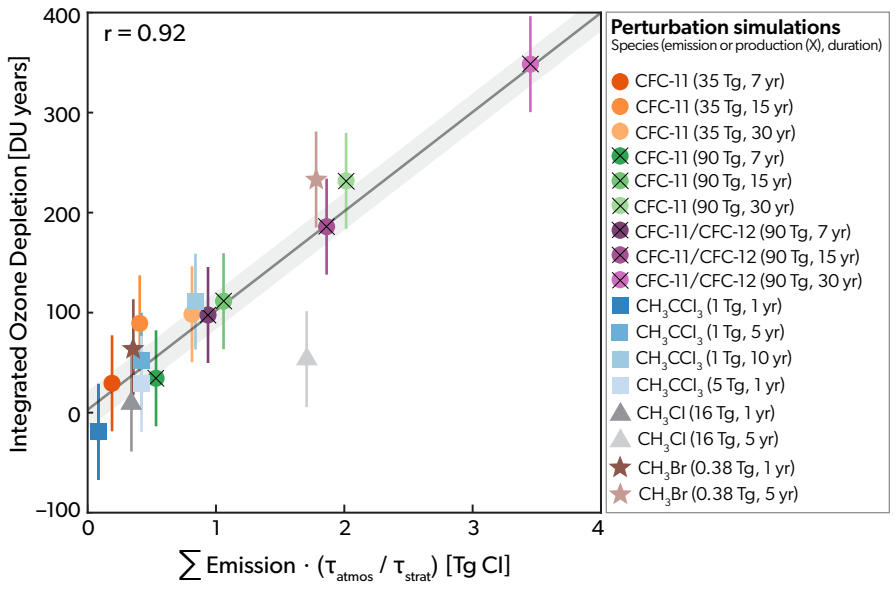


**Figure 3-25.** Integrated ozone depletion (IOD; units of DU years) from different CCM simulations performed with the UM-UKCA chemistry-climate model, plotted against the cumulative emissions of a halogenated source gas (quantified in units of Tg Cl) multiplied by the dimensionless ratio of the whole-atmospheric lifetime to the stratospheric lifetime of that halogenated source gas. The different colored points correspond to CCM experiments with different emitted species (different shapes), the magnitude of the annual emissions or production (with an "X"; includes a major portion that goes in banks) of that species, and the duration of the emissions. [Adapted from Pyle et al., 2022.]

have the same variance. The FastRecovery scenario clearly recovers to the 1980 value sooner than SlowRecovery and so has an earlier return date. There is also a much smaller uncertainty associated with the FastRecovery return date, despite the identical variances, since the lower bound on the projected TCO remains above the 1980 value from the late 2040s onward. In contrast, the lower bound for TCO remains below the 1980 value beyond 2100 for the SlowRecovery scenario. TCO projections that only slightly exceed the 1980 TCO value therefore have large uncertainty ranges in their return dates.

Generally, TCO return dates from CMIP6 models using the SSPs are consistent with those from previous modeling activities (**Figure 3-24b**). Under the SSP2-4.5 scenario, which assumes more modest increases in GHGs, near-global mean (60°S–60°N) TCO is projected to return to 1980s values before the middle of the century (around 2040). In contrast, under scenarios with the least mitigation for GHGs and NTCFs (SSP3-7.0 and SSP5-8.5), near-global mean TCO is projected to return to 1980 values earlier (around 2030). However, as noted above, for the scenario with the strongest mitigation (SSP1-2.6), the total column is not projected to return to 1980 values before 2100. Recovery happens for all analyzed SSPs in the SH mid-latitudes (where the levels of tropospheric ozone precursors are already low), but ozone does not return to 1980 values in the tropics for the two SSPs with the strongest (SSP1-2.6) and comparatively strong (SSP2-4.5) mitigation (**Figure 3-24b**). In addition, tropical TCO recovery for the SSP with weakest GHG mitigation (SSP5-8.5) does not last the whole century (**Figure 3-24b**), as the strengthened Brewer–Dobson circulation (BDC; see *Chapter 5*) reduces the column beyond 1980 levels after about 2070 (**Figure 3-18**). Finally, some of the return dates are associated with very large uncertainty estimates, particularly the near-global return date under the SSP2-4.5 scenario and the tropical return dates under the SSP3-7.8 and SSP5-8.5 scenarios (**Figure 3-24b**). This is because TCO remains close to the 1980 value for several decades on either side of the return date for those scenarios, and interannual variability means that it may rise above and fall below the return threshold.

While the 1980 return date has been widely used as a metric of ozone recovery in this and previous Assessments and remains an important milestone on the road to ozone recovery, it has some shortcomings. In addition to the fact that significant ozone depletion occurred before 1980 (Shepherd et al., 2014; Langematz et al., 2016), future ozone changes in some regions may be dominated by changes in other processes, such as stratospheric temperature and circulation changes following increases to GHGs or changes happening in the troposphere (**Box 3-3**). Overall, this can mean that despite reductions in stratospheric halogens, the total column never returns to historical values. Return dates also do not measure the overall integrated decrease in ozone prior to that date, which may be more relevant for some impacts (e.g., changes in surface UV). This is particularly true for short-lived halogenated ODSs (*Section 3.3.4.2*), which, owing to their short atmospheric lifetimes, may substantially deplete stratospheric ozone without affecting TCO return dates.

Recognizing these shortcomings, a new ozone recovery metric has recently been proposed to use alongside return dates: integrated ozone depletion (IOD; Pyle et al., 2022). IOD measures the time integrated TCO difference between separate future ozone projections, each following different halogen emissions scenarios. For example, a hypothetical, large, short-duration emission of a halogenated species with a short lifetime (e.g., methyl chloride [$CH_3Cl$] or methyl bromide [$CH_3Br$]) would result in substantial ozone depletion, and therefore a large IOD, but potentially no change in the return date if the additional emitted halogen is removed from the atmosphere before the total column has returned to historical values. Conversely, additional emissions of a long-lived species like CFC-11 could result in TCO reductions of a few Dobson units for several decades, which may lead to large delays in ozone return dates, but only a small IOD. Using CCM simulations, it has been shown that there is a linear relationship between IOD and the product of the time-integrated additional emissions (in Tg chlorine) of a halogenated species and the ratio of the species' whole-atmospheric lifetime to its stratospheric lifetime (**Figure 3-25**). There is scope to exploit this

empirical relationship to estimate IOD values without the need for CCM simulations, allowing simple predictions of the impact of halogenated emissions on ozone recovery.

### 3.4.3 Vertically Resolved Ozone Projections

Vertically resolved changes over the 21st century also depend strongly on the future scenario. Zonal-mean ozone differences between the end of the 21st century (2086–2100 average) and the present day (2000–2014 average) are shown in **Figure 3-26** for a range of SSPs (SSP1-2.6, SSP2-4.5, SSP3-7.0, and SSP5-8.5) and a subset of the CMIP6 models (after Keeble et al., 2021a). The zonal-mean picture is complemented by the future evolution of TCO and the stratosphere and troposphere partial columns (**Figure 3-27**). Ozone mixing ratios in the upper stratosphere and SH polar lower stratosphere are projected to increase for all the SSPs shown, consistent with the decline in halogenated ODSs. The upper-stratospheric increases in ozone grow in magnitude as the GHG emissions increase across the scenarios (moving from SSP1-2.6 to SSP5-8.5) due to the resulting $CO_2$-induced cooling of the stratosphere (e.g., Isaksen et al., 1980).

Significant differences between the scenarios are seen in the troposphere and tropical lower stratosphere. Tropospheric ozone mixing ratios decrease in the scenarios with large reductions in the emissions of ozone precursors (SSP1-2.6 and SSP2-4.5). In particular, under SSP1-2.6 the decreases in tropospheric ozone are particularly strong in the Northern Hemisphere, while the increases in stratospheric ozone outside of the Antarctic polar lower stratosphere are smaller than in other scenarios (consistent with less $CO_2$-induced cooling). The strong emissions mitigation in these scenarios slow or prevent the return of TCO to its historical levels (*Section 3.4.2*).

In contrast, ozone mixing ratios are projected to increase throughout much of the troposphere and upper stratosphere in the SSPs with weak or little mitigation (SSP3-7.0 and SSP5-8.5), leading to the projected super-recovery of the mid- and high-latitude TCO by the end of the century (**Figure 3-18**). However, ozone mixing ratios are projected to be lower in the tropical

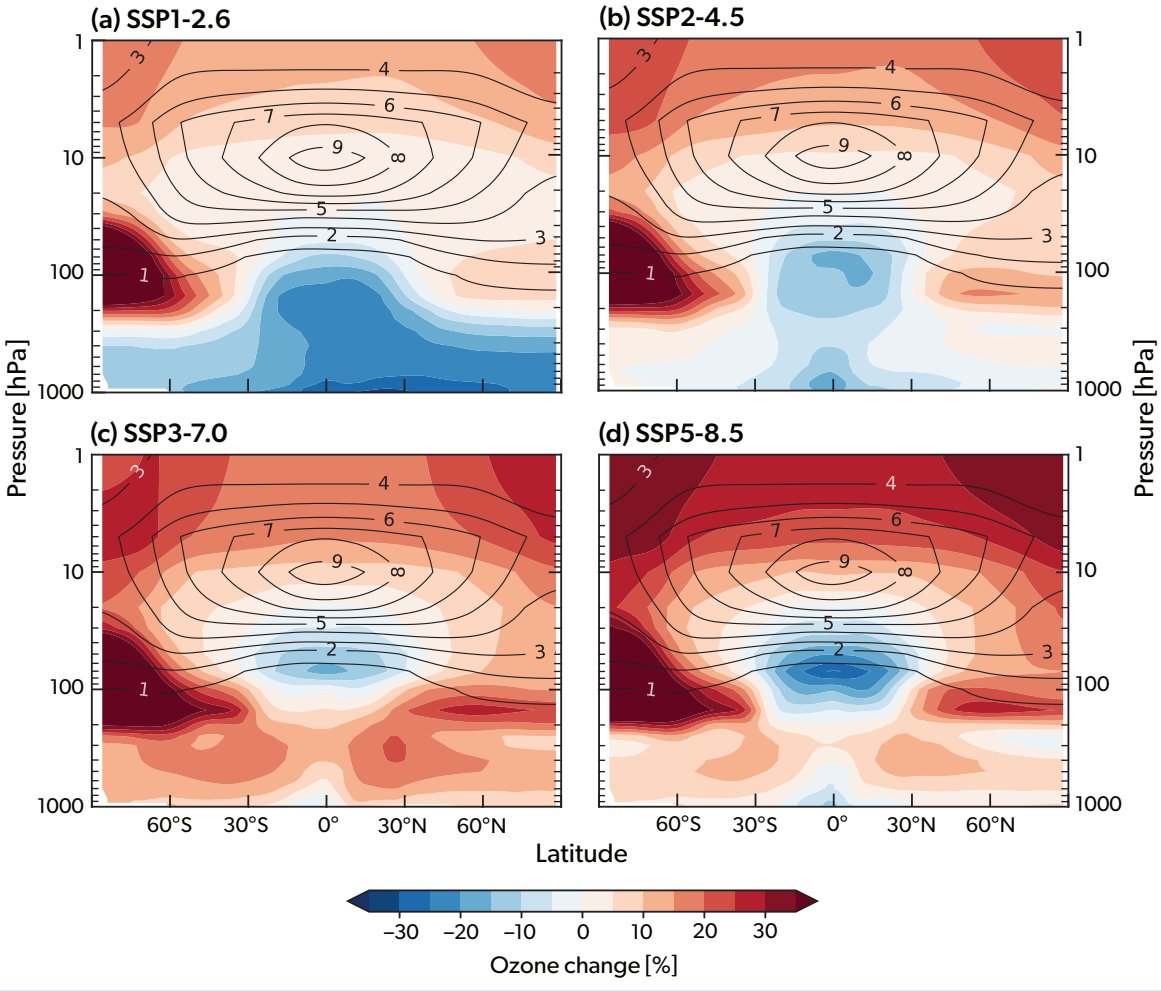


**Figure 3-26.** Simulated CMIP6 multi-model mean (12 models) and zonal-mean ozone changes (%) between the beginning (2000–2014 average) and end (2086–2100 average) of the 21st century. The present-day (2000–2014) zonal mean ozone climatology (as mixing ratio, in ppmv) is also shown as black contour lines. Changes are shown for the (a) SSP1-2.6, (b) SSP2-4.5, (c) SSP3-7.0, and (d) SSP5-8.5 scenarios (see **Box 3-4**). [Adapted from Keeble et al., 2021a.]

lower stratosphere by the end of the century (**Figure 3-26**) for these scenarios. As noted in the last Assessment, this is due to the acceleration of the BDC, resulting in decreases in tropical lower-stratospheric ozone and the reduced production of ozone, due to a thicker overhead column ozone (Eyring et al., 2013; Iglesias-Suarez et al., 2016; Meul et al., 2016; Keeble et al., 2017). This decrease in lower-stratospheric ozone offsets increases at higher altitudes, leading to renewed TCO decreases in the latter half of the 21st century for the SSP with the strongest GHG increases (SSP5-8.5), despite projected reductions in stratospheric halogens under the Montreal Protocol (**Figure 3-18**; *Section 3.4.2*).

### 3.4.4 Impacts of Unregulated CFC-11 Emissions on Ozone Recovery

Since the last Assessment, a new source of CFC-11 emissions was identified in East Asia (Montzka et al., 2018; Rigby et al., 2019; see also *Chapter 1*). Given the well-established effectiveness of chlorofluorocarbon-derived chlorine at depleting stratospheric ozone, several recent model studies have estimated the impacts of increased CFC-11 emissions on the trajectory of stratospheric ozone recovery (Dameris et al., 2019; Dhomse et al., 2019; Fleming et al., 2020, 2021; Keeble et al., 2020; WMO, 2021). In contrast to the CMIP6 simulations, which explored future ozone

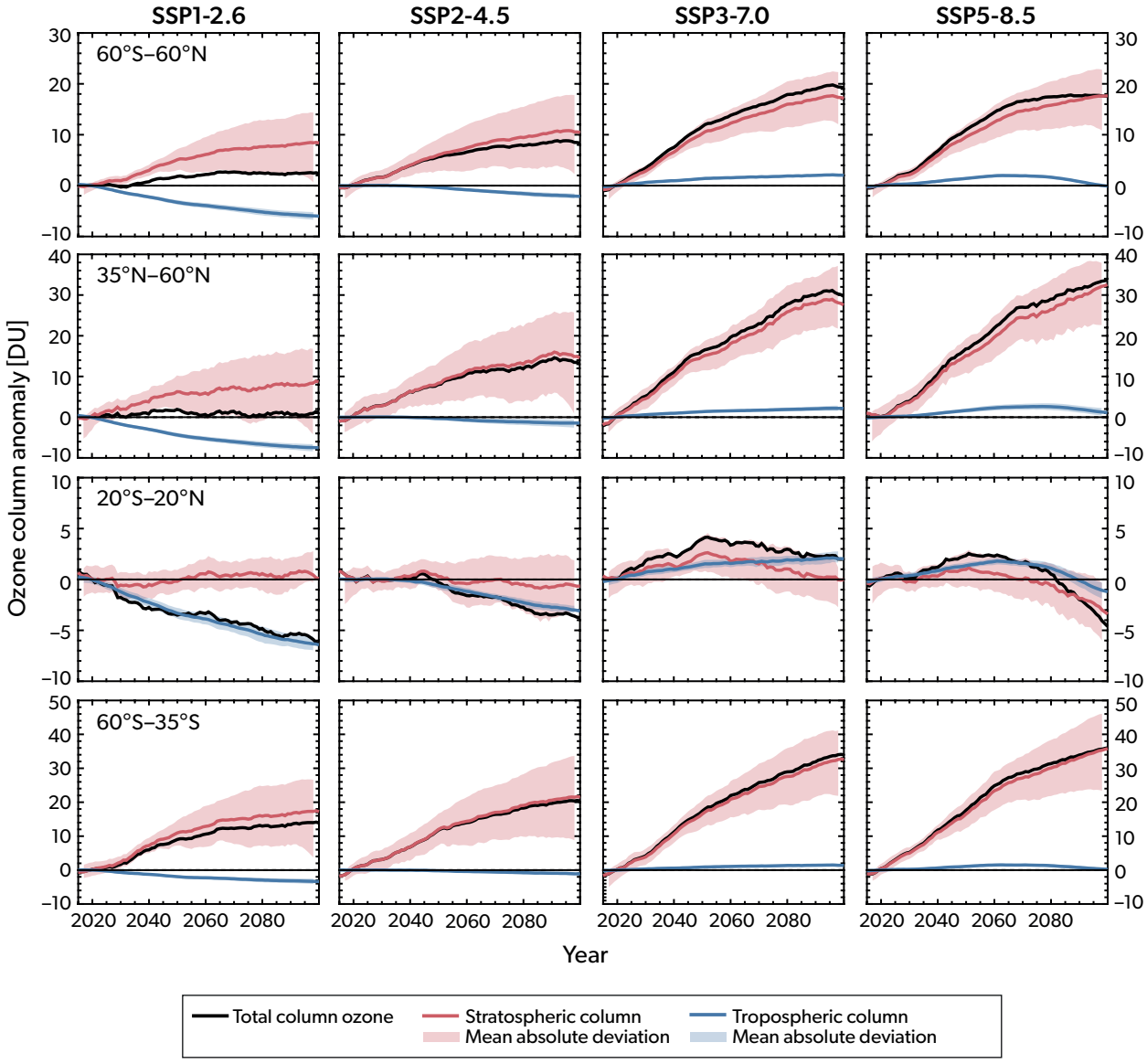


**Figure 3-27.** Time series of annual and CMIP6 multi-model mean anomalies (four models; relative to 2015) for TCO (black) and stratospheric (red) and tropospheric (blue) partial column ozone for the *(left to right)* SSP1-2.6, SSP2-4.5, SSP3-7.0 and SSP5-8.5 scenarios (see **Box 3-4**), shown for *(top to bottom)* the near-global mean (60°S–60°N), NH mid-latitudes (35–60°N), tropics (20°S–20°N), and SH mid-latitudes (60–35°S). Shaded areas, for the stratospheric and tropospheric ozone columns, are the mean absolute deviations from the multi-model mean. [Updated from results published by Keeble et al., 2021a.]

changes for specific emissions scenarios, there are no common scenarios that consider noncompliance with the Montreal Protocol, and, instead, individual studies followed different assumptions for CFC-11 emissions. Nevertheless, a key result that emerges from combining these studies is a linear relationship between the cumulative amount of CFC-11 emitted and metrics of stratospheric ozone recovery: global total column depletion and the delay in return dates (Keeble et al., 2020; Fleming et al., 2021; WMO, 2021). This allows an estimate of the impact of the actual emissions of CFC-11 identified through observations, even if that specific scenario has not been performed with a chemistry model.

Using the linear relationship, given the estimated additional 120–440 Gg CFC-11 emissions over the period 2012–2019 (WMO, 2021), and applying a decrease of 0.4–0.7 DU per 1000 Gg cumulative CFC-11 emissions (Keeble et al., 2020; Fleming et al., 2021), the estimated global mean total column depletion is 0.05–0.31 DU. This is supported by further simulations run from 2000 to 2017 with and without an additional 230 Gg (cumulative) CFC-11 emissions. These runs simulate the impact of the additional CFC-11 emissions specifically on polar ozone, where the response is expected to be largest, and even here the impact is small (Dhomse et al., 2019; WMO, 2021). Together, these studies indicate that the impact of increased emissions of CFC-11 to date have had a small impact on TCO, and, for instance, do not explain the recent lower-stratosphere ozone trends (see *Section 3.3.3*).

Finally, as with TCO, a linear relationship between the additional CFC-11 emissions and the delay of total ozone recovery to 1980 values can be estimated from the simulations, with the delay varying between 0.9 and 4.2 years per 1000 Gg cumulative CFC-11 emissions (**Figure 3-28**). Based on the estimated 120–440 Gg cumulative additional CFC-11 emissions for 2012–2019, the estimated delay to global ozone recovery is 0.4–1.3 years. While this further supports the fact that the additional CFC-11 emissions to date will have only a modest impact on stratospheric ozone recovery, it is clear from the linear relationships that if additional unregulated CFC-11 emissions were to continue in the future, noticeable delays to ozone return dates could result.

## 3.4.5 Impacts of Stratospheric Ozone Recovery on Tropospheric Ozone

Changes in the stratosphere will impact tropospheric ozone (Zeng et al., 2010) both dynamically, mainly via enhanced stratosphere-to-troposphere (STT) transport through a strengthened BDC (Butchart, 2014; *Chapter 5*), and chemically, such as through changes in photolysis rates via UV radiation changes due to changes in overhead ozone columns (Voulgarakis et al., 2013). The resulting impact on tropospheric ozone depends strongly on the scenario.

The influence of a future stratosphere on tropospheric ozone has been explored in four CMIP6 models running a weak mitigation scenario (SSP3-7.0; Griffiths et al., 2021; **Figure 3-29**). For these models, STT increases over the 21st century, consistent with the stratospheric ozone recovery (due to the reduction in ODSs) and a strengthened BDC (due to increased GHGs; **Figure 3-29**). There is, however, a large model spread in the magnitude of the STT increase. By the end of this century, STT exceeds pre-depletion levels in all models except the one that shows the strongest ozone depletion over 1980–2000 (UKESM1-LL-0). Moreover, the strongest STT increase is seen in the model that shows the weakest ozone depletion (MRI-ESM2.0). Confidence in the magnitudes of these changes in STT is low, however. STT was not directly diagnosed by the models and is instead inferred as a residual of other fields by assuming that tropospheric chemical production and the net influx from STT balances tropospheric chemical loss and dry deposition to the surface, and this is somewhat sensitive to how the tropopause is defined (Young et al., 2018; Griffiths et al., 2021).

STT has also been explored in other CCMs, giving broadly consistent results to the CMIP6 models. Since the last Assessment,

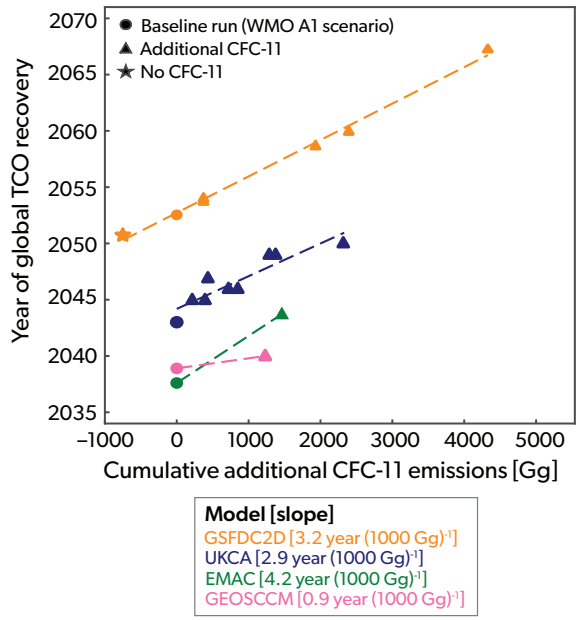


**Figure 3-28.** Dependence of global (90°S–90°N) annual mean TCO 1980 return dates on cumulative additional equivalent CFC-11 emissions (Gg), emitted up to the return date for each simulation, for various models. Colors represent different models and symbols represent different simulations. Each model performed a baseline simulation (circles) with the WMO A1 scenario for ODS halogen loadings (WMO, 2018). On top of this baseline scenario, the models performed perturbation simulations (stars and triangles) with different assumptions of additional CFC-11 emissions (and in some cases CFC-12, which are converted to equivalent CFC-11 emissions) shown by the x-axis. The dashed lines show the best linear fits to the simulations for each model, with the slope giving the delay in global TCO recovery in units of years per 1000 Gg. For consistent plotting, the simulated return dates for EMAC (which ignores some replacement chlorine compounds and produces early recovery) and GEOSCCM have been moved later by 20 years and 5 years, respectively. [Adapted from WMO, 2021.]

there has been further analysis of a subset of seven CCMI-1 CCMs, providing a more detailed exploration of the potential impact of future stratospheric ozone changes on the tropospheric ozone burden using a stratospheric ozone tracer (Abalos et al., 2020). This stratospheric transport tracer ($O_3S$) is a diagnostic that is directly related to the ozone concentration in the stratosphere, but in the troposphere its value is affected by photochemical destruction and deposition, meaning that it can be used as a marker of the fraction of tropospheric ozone that originated in the stratosphere. For the RCP6.0 scenario (which has lower emissions than the SSP3-7.0 scenario), the $O_3S$ tropospheric column increases from the year 2000 to around 2060, consistent with stratospheric ozone recovery and an enhanced BDC, which both contribute to enhanced STT (Abalos et al., 2020; **Figure 3-30a**). The proportion of the tropospheric ozone column attributable to $O_3S$ (i.e., ozone sourced from the stratosphere) increases monotonically in all models. However, there is a large spread in the absolute value of this proportion between the models, ranging from 22 to 45% at the start of the 21st century and 25 to 55% at the end of the century (Abalos et al., 2020; **Figure 3-30b**). In terms of attributing drivers to the STT trends, the CCMI analysis found that ODS-induced stratospheric ozone changes overwhelm the greenhouse gas effect on the BDC between 2000 and 2100 (Abalos et al., 2020). Although the decline of ODSs has been projected to weaken the BDC (Polvani et al., 2019; see also *Chapter 5*), the increased ozone reservoir in the stratosphere dominates the future ozone STT trends (Abalos et al., 2020).

The relative contributions to future STT from ODSs and GHG changes will depend on the emissions scenario, with a potentially bigger contribution from an enhanced BDC in higher GHG emissions scenarios. A single model study has projected a 53% increase in STT between 2000 and 2100 under a high emissions scenario (RCP8.5), attributing 46% of this to the effects of increasing GHGs and 7% to the effects of decreasing ODSs. This results in the ratio of $O_3S$ to the total tropospheric ozone increasing from 43 to 46% in the Northern Hemisphere and from 48 to 52% in the Southern (Meul et al., 2018). The same single model study also explored a scenario with weak mitigation (RCP6.0) and found that the ratio of $O_3S$ to tropospheric column ozone had a similar increase despite a smaller STT increase. This underlines that the relative impact of stratospheric ozone on tropospheric ozone depends on the evolution of tropospheric ozone under different future GHG and ozone precursor scenarios. Nevertheless, a robust result from the simulations is that a projected future increase in STT associated with higher GHG emissions will have a detectable impact on tropospheric ozone.

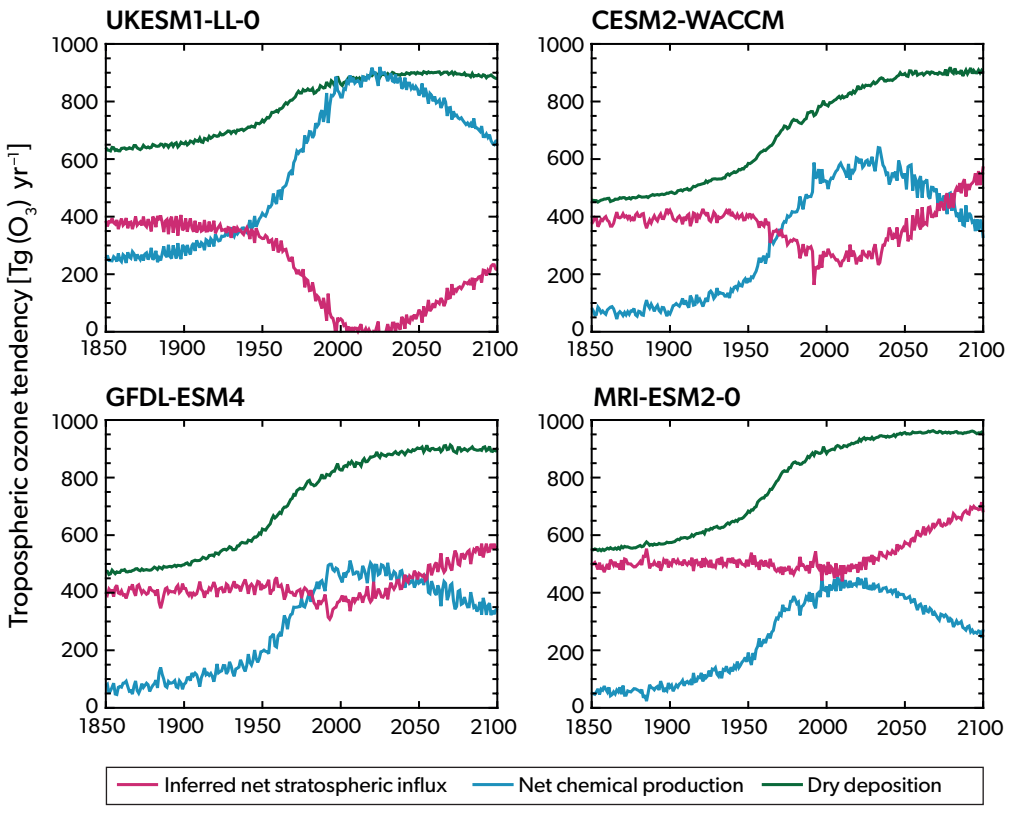


**Figure 3-29.** Time series of the simulated tropospheric ozone budget terms over 1850–2100 in four CMIP6 models from the historical (1850–2014) and SSP3-7.0 (2015–2100) simulations, showing dry deposition (green), net chemical production (NCP, blue), and the residual (dry deposition minus NCP, assumed to be net stratospheric influx; red). The troposphere is delimited using the WMO tropopause definition. The budget terms are shown for the four CMIP6 models with the required output: UKESM1-0-LL, CESM2-WACCM, GFDL-ESM4, and MRI-ESM2-0. [Adapted from Griffiths et al., 2021.]

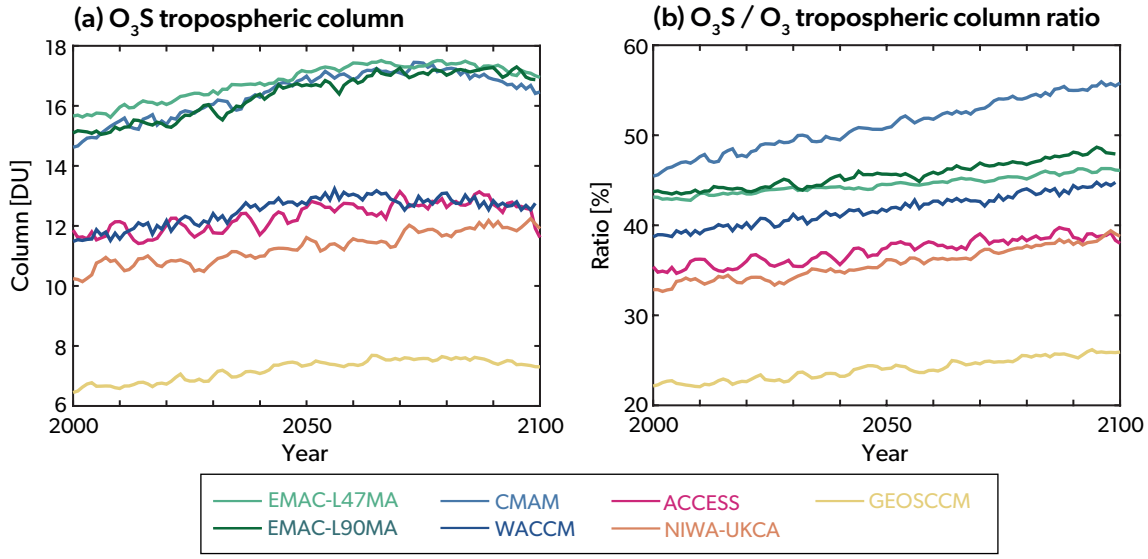


**Figure 3-30.** Time series for 2000–2100 of (a) the tropospheric column contribution of the stratospheric ozone tracer ($O_3S$) and (b) the ratio of $O_3S$ to the global tropospheric ozone column, from the REF-C2 simulations of seven CCMs from the CCMI-1 experiment (Morgenstern et al., 2017). [Adapted from Abalos et al., 2020.]

Finally, the last Assessment noted that future changes in tropospheric ozone are likely to be dominated by changes in precursor emissions, with the stratosphere playing a relatively minor role in the increasing tropospheric ozone abundance. However, given that most tropospheric ozone precursors decrease under the new SSPs (apart from methane, which follows a range of trajectories; **Box 3-4**), STT plays an increasingly important role in tropospheric ozone changes. Indeed, recent improvements in diagnostic and modeling tools provide new evidence that the stratosphere has had a much larger influence than previously thought over the most recent climatological period (1980–2010; Williams et al., 2019). Moreover, a new accounting method proposed for the tropospheric budget also suggests an increased importance for ozone of stratospheric origin (Bates and Jacob, 2020). If these tools and methods are assessed in additional models and applied more generally, it could lead to a reappraisal of the role of the stratosphere in current and projected tropospheric ozone budgets.

# APPENDIX 3A : DATA SOURCES

## 3A.1 PROXIES USED IN DIFFERENT PUBLISHED OZONE TREND MODELS

The proxies, parameters used for the proxies, and their data sources are listed in **Table 3A-1**.

## 3A.2 GROUND-BASED DATASETS

The total column ozone (TCO) and profile trends assessed in this report are based on datasets listed in **Table 3A-2** for ozone observations by ground-based techniques. Most ground-based data records have been simply extended in time since the 2018 Assessment and are archived in the WOUDC or NDACC databases. This is the case for Dobson and Brewer spectrophotometers, SAOZ spectrometers, FTIR spectrometers, microwave radiometers, lidars, balloon-borne ozonesondes, and aircraft-mounted sensors (see WMO, 2018, and references therein).

Since the last Assessment, several records have been revised to detect and correct for inhomogeneities. The four NOAA Dobson Umkehr datasets of Boulder, Lauder, Observatoire de Haute-Provence (OHP), and Mauna Loa have been optimized through a day-to-day comparison with Umkehr profiles simulated by a chemical transport model (Petropavlovskikh et al., 2022), resulting in a noticeable bias reduction compared to MLS and the combined SBUV and OMPS records.

There is a seasonal dependence to the difference between TCO measurements by Dobson and Brewer spectrophotometers that is attributed to the temperature sensitivity of the ozone absorption coefficient of the Dobson instrument (Redondas et al., 2014). The Arosa datasets have been reprocessed using a newer ozone absorption cross section (Serdyuchenko et al., 2014) in conjunction with an effective ozone temperature dataset. This has reduced the seasonal dependence of the difference to 1% (Gröbner et al., 2021). The quality of the world's longest ozone column measurements time series has been assessed, with the conclusion that any bias induced by the automatization and the relocation of the Dobson instrument is not statistically significant (Stübi et al., 2021).

**Table 3A-1.** Proxies used in different published ozone trend models, including representative data sources. Those used in the different trend analyses presented in *Section 3.3* are highlighted in bold text.

| Proxy | Parameter | Data Sources |
|---|---|---|
| Solar Cycle | **10.7 cm solar radio flux** | **National Research Council Canada Dominion Radio Astrophysical Observatory: www.spaceweather.gc.ca/forecast-prevision/solar-solaire/solarflux/sx-en.php** |
| | 30 cm solar radio flux | CNES Collecte Localisation Satellites Space Weather Services: spaceweather.cls.fr/services/radioflux/ |
| | **Core-to-wing ratio of Mg II doublet (280 nm)** | **University of Bremen: www.iup.uni-bremen.de/UVSAT/Datasets/mgii** |
| QBO | **EOF1 and EOF2 of tropical zonal winds** | **Free University of Berlin: www.geo.fu-berlin.de/en/met/ag/strat/produkte/qbo/** |
| | **Tropical zonal winds at 2 pressure levels (e.g., 30 and 50 hPa; 10 and 30 hPa)** | **NOAA National Weather Service Climate Prediction Center: www.cpc.ncep.noaa.gov/data/indices/** |
| ENSO | **Multivariate ENSO index (v1 superseded by v2 from December 2018)** | **NOAA Earth System Research Laboratory: www.esrl.noaa.gov/psd/enso/mei/** |
| | Niño 3.4 index | NOAA National Weather Service Climate Prediction Center: www.cpc.ncep.noaa.gov/data/indices www.cpc.ncep.noaa.gov/products/precip/CWlink/MJO/enso.shtml |
| | Southern Oscillation index | |
| Aerosol | **Aerosol extinction, optical depth, and properties** | **NASA EarthData ASDC: asdc.larc.nasa.gov/project/GloSSAC/GloSSAC_2.0** |
| | Aerosol extinction | Chouza et al. (2020) |
| | **Aerosol optical depth** | **NASA Goddard Institute for Space Studies: data.giss.nasa.gov/modelforce/strataer (terminates in 2012)** |
| Other Dynamical Proxies | Brewer–Dobson circulation (BDC): eddy heat flux (EHF) at 100 hPa | NOAA National Weather Service Climate Prediction Center: www.cpc.ncep.noaa.gov/products/stratosphere/polar/polar_body.html |
| | North Atlantic Oscillation (NAO) index | NOAA National Weather Service Climate Prediction Center: www.cpc.ncep.noaa.gov/products/precip/CWlink/pna/nao.shtml |
| | **Arctic Oscillation (AO) index** | **NOAA National Weather Service Climate Prediction Center: www.cpc.ncep.noaa.gov/products/precip/CWlink/daily_ao_index/ao.shtml** |
| | **Antarctic Oscillation (AAO) index** | **NOAA National Weather Service Climate Prediction Center: www.cpc.ncep.noaa.gov/products/precip/CWlink/daily_ao_index/aao/aao.shtml** |
| | Tropopause pressure (TP) | NOAA Earth System Research Laboratory: www.esrl.noaa.gov/psd/data/gridded/data.ncep.reanalysis.tropopause.html NASA Global Modeling and Assimilation Office: disc.gsfc.nasa.gov/datasets?project=MERRA-2 |
| | Upper BDC index (UBDC) | Ball et al. (2016) |
| | Indian Ocean Dipole Mode Index (IOD MI) | psl.noaa.gov/gcos_wgsp/Timeseries/DMI/ |

Ongoing efforts are being conducted by the ozonesonde community to quantify the uncertainties and biases of those measurements (Tarasick et al., 2021) in the framework of the ASOPOS 2.0 project (Smit and Thompson, 2021). There is also an effort to homogenize the individual ozonesonde datasets, performed either by the station scientists themselves or in the broader framework of the Tropospheric Ozone Assessment Report Phase 2 (TOAR II) project (42 of the stations have been processed [R. van Malderen, personal communication] and are used in the zonal-mean anomalies time series and trends in this Assessment; see **Table 3A-2**). However, comparisons between TCO from ECC ozonesondes and OMI and OMPS TCO show a decrease in TCO and stratospheric ozone up to 6% for one-third of the 37 stations after 2013. This decline is attributed to ozone measured by the ECC instruments, although no single property of the ozonesondes explains the findings (Stauffer et al., 2020). The post-2013 datasets of the affected sites should not be used for trend estimation and are not used in this Assessment.

The Izaña FTIR record has been reprocessed using an improved retrieval algorithm that optimizes the selection of ozone spectral micro windows and simultaneously retrieves the temperature (García et al., 2022). This enhances the precision and accuracy of the FTIR ozone total column by 0.1–0.2% and results in better agreement with coincident Brewer observations.

Since the 2018 Assessment, European ozone lidars have been evaluated in two campaigns (Wing et al., 2020, 2021), with the conclusion that there is good agreement between all ozone lidar measurements in the range of 15–41 km, with relative differences between collocated ozone profiles of less than ±10%.

## 3A.3 MERGED AND INDIVIDUAL SATELLITE DATASETS

### 3A.3.1 Total Column Ozone

Since the last ozone Assessment, TCO time series have been updated and reported as zonal-mean and global mean datasets

**Table 3A-2.** TCO and ozone profiles measured by ground-based techniques used in the monthly zonal-mean data considered in this Assessment. Datasets marked with an asterisk (*) have been homogenized since the last Assessment. Datasets in square brackets are sonde stations that have not been corrected for 2013 drop-off.

| Instruments | Altitude Range Vertical Resolution Units | Station (Start of Data Record) | | |
|---|---|---|---|---|
| | | 60–35°S | 20°S–20°N | 35–60°N |
| Ozonesonde | 0–30 km<br>~150 m<br>mPa | Lauder (1986),<br>Macquarie Island (1994),<br>Broadmeadows (1999) | *Hilo (1982),<br>[*Samoa (1986)],<br>*Izaña (1995),<br>[Ascension (1998)],<br>[*Fiji (1997)],<br>Irene (1998),<br>[Nairobi (1998)],<br>[Natal (1998)],<br>Reunion (1998),<br>Kuala Lumpur (1998),<br>*Paramaribo (1999),<br>Hong Kong Observatory (2000),<br>Hanoi (2004),<br>[Costa Rica (2005)] | *Goose Bay (1963),<br>*Payerne (1966),<br>*Hohenpeißenberg (1966),<br>*Boulder (1967),<br>Tateno (1968),<br>*Uccle (1969),<br>*Edmonton (1970),<br>[*Churchill (1973)],<br>Lindenberg (1975),<br>Legionowo (1979),<br>Praha (1979),<br>*Boulder (1991),<br>*OHP (1991),<br>*De Bilt (1992),<br>Lerwick (1992),<br>Madrid (1994),<br>Valentia (1994),<br>Wallops Island (1995),<br>*Trinidad Head (1997),<br>*Yarmouth (2003),<br>*Kelowna/Port Hardy (2003) |
| Lidar | 15–50 km<br>1–10 km<br>number density | Lauder (1994) | Mauna Loa (1993) | OHP (1986),<br>Hohenpeißenberg (1987),<br>Table Mountain (1988) |
| Microwave Radiometer (MWR) | 20–70 km<br>8–15 km<br>ppm | Lauder (1992) | Mauna Loa (1995) | Bern (1994),<br>Payerne (2000) |
| FTIR Spectrometer | 0–50 km<br>8–20 km<br>molec $cm^{-2}$<br>Total column by integrating ozone profiles | Wollongong (1996),<br>Lauder (2001) | Izaña (1999) | Jungfraujoch (2000) |
| Dobson and Brewer Umkehr | 0–50 km<br>5–10 km<br>DU | Perth (1984),<br>*Lauder (1987) | *Mauna Loa (1984) | *Arosa/Davos (1956),<br>*Boulder (1984),<br>*OHP (1984),<br>Fairbanks (1994) |
| Dobson<br>Brewer<br>SAOZ UV-VIS<br>Filter Ozone Meters<br>Ozonesondes | Total column ozone<br>DU<br><br>Integrated ozone profiles | worldwide (1926) | | |

(Weber et al., 2020, 2022). As described below, four merged and homogenized datasets are used in this report. See further details in **Table 3A-3**.

There are integrated vertical ozone profiles from two different versions of merged datasets from the series of SBUV and SBUV-2 satellite instruments and OMPS (NASA SBUV MOD v8.7 and NOAA SBUV Merge v8.7). The NASA SBUV MOD v8.7 is now a monthly mean zonal (5°) and gridded average product, including both profiles and TCO data. OMPS v2.6 data have been included since 2012 and have been intercalibrated to the SBUV series based on overlap comparisons with NOAA 19 SBUV/2 (McPeters et al., 2019).

There are two merged datasets based on the series of European satellite spectrometers (GOME, SCIAMACHY, and GOME-2A), which use different retrieval algorithms and slightly different merging approaches (University of Bremen GSG and ESA/DLR GTO datasets). The ozone retrieval algorithm (GODFIT v4) and the merging approach of the GTO dataset were improved since the last Assessment, and three more sensors were added (OMI/Aura, GOME-2/MetOp-B, and TropOMI/Sentinel-5P; Garane et al., 2018). Comparisons with adjusted MERRA-2 reanalysis data indicate a mean bias of −0.9 ± 1.5% on the monthly mean TCO (Coldewey-Egbers et al., 2020), with a change of ~2% in 2004 when OMI data are included in both GTO and MERRA-2 (Zhao et al., 2021).

### 3A.3.2 Profiles

Information about the zonally averaged merged datasets of ozone profiles, which are used in this Assessment, is listed in **Table 3A-4**. Since the last Assessment, these datasets have been extended until December 2020 (Froidevaux et al., 2015; Davis et al., 2016; Bourassa et al., 2018; Sofieva et al., 2017; Arosio et al., 2019; Ball et al., 2019a). Additional efforts were made to improve the consistency and stability of the SBUV datasets (Frith et al., 2017; Wild et al., 2016). Several merged datasets with a gridded structure (latitudinally and longitudinally resolved) have been the focus of recent developments (Sofieva et al., 2021; Arosio et al., 2019; Davis et al., 2016; Frith et al., 2017; **Table 3A-5**). They are the basis of the regionally and seasonally dependent trend analyses discussed in this chapter.

Several studies have compared the consistency, biases, and stability between different individual satellite ozone datasets, which are incorporated in the merged datasets used in this Assessment (Rahpoe et al., 2015; Hubert et al., 2016; Hegglin et al., 2021).

**Table 3A-3.** Satellite-based merged TCO datasets used in this Assessment.

| Merged Dataset | Instruments and Data Version | Ozone Representataion | Latitude Coverage and Sampling | Temporal Coverage |
|---|---|---|---|---|
| SBUV NASA (MOD) | Nimbus 4 BUV v8.7<br>Nimbus 7 SBUV v8.7<br>NOAA 11 SBUV/2 v 8.7<br>NOAA 14 SBUV/2 v8.7<br>NOAA 16 SBUV/2 v8.7<br>NOAA 17 SBUV/2 v8.7<br>NOAA 18 SBUV/2 v8.7<br>NOAA 19 SBUV/2 v8.7<br>S-NPP OMPS NP NASA v2.8 | Integrated vertical ozone profile in DU | 80°S–80°N,<br>5° latitude bands | 1970–2020 |
| SBUV NOAA (COH) | Nimbus 7 SBUV v8.6<br>NOAA 11 SBUV/2 v 8.6<br>NOAA 14 SBUV/2 v8.6<br>NOAA 16 SBUV/2 v8.6<br>NOAA 17 SBUV/2 v8.6<br>NOAA 18 SBUV/2 v8.6<br>NOAA 19 SBUV/2 v8.6<br>S-NPP OMPS NP NOAA v3r2 | Integrated vertical ozone profile in DU | 80°S–80°N,<br>5° latitude bands | 1978–2020 |
| GTO | GOME/ERS-2<br>SCIAMACHY/Envisat<br>GOME-2/MetOp-A<br>OMI/Aura<br>GOME-2/MetOp-B<br>TropOMI/Sentinel-5P | mol $m^{-2}$ or DU | 90°S–90°N,<br>1° × 1° | 1995–2020 |
| GSG | GOME/ERS-2<br>SCIAMACHY/Envisat<br>GOME-2/MetOp-A | mol $m^{-2}$ or DU | 90°S–90°N,<br>1° × 1.25°,<br>(5° latitude bands) | 1995–2020 |

**Table 3A-4.** Merged satellite vertical ozone profile datasets used in this Assessment (monthly zonal-mean data).

| Merged Dataset | Instruments and Data Version | Ozone Representation | Latitude Coverage and Sampling | Vertical Range and Sampling | Temporal Coverage |
|---|---|---|---|---|---|
| SBUV NASA (MOD) | Nimbus 4 BUV v8.7<br>Nimbus 7 SBUV v8.7<br>NOAA 11 SBUV/2 v 8.7<br>NOAA 14 SBUV/2 v8.7<br>NOAA 16 SBUV/2 v8.7<br>NOAA 17 SBUV/2 v8.7<br>NOAA 18 SBUV/2 v8.7<br>NOAA 19 SBUV/2 v8.7<br>S-NPP OMPS NP NOAA v2.8 | Mixing ratio on pressure levels | 80°S–80°N,<br>5° latitude bands | 15 pressure levels between 50 and 0.5 hPa | 1970–2020 |
| SBUV NOAA (COH) | Nimbus 7 SBUV v8.6<br>NOAA 11 SBUV/2 v 8.6<br>NOAA 14 SBUV/2 v8.6<br>NOAA 16 SBUV/2 v8.6<br>NOAA 17 SBUV/2 v8.6<br>NOAA 18 SBUV/2 v8.6<br>NOAA 19 SBUV/2 v8.6<br>S-NPP OMPS NP NASA v2.6 | Mixing ratio on pressure levels | 80°S–80°N,<br>5° latitude bands | 15 pressure levels between 50 and 0.5 hPa | 1978–2020 |
| SWOOSH | SAGE II v7.0<br>HALOE v19<br>UARS MLS v5<br>SAGE III v4<br>Aura MLS v4.2 | Mixing ratio on pressure levels | 90°S–90°N,<br>10°, 5°, 2.5° latitude bands | 316–1 hPa, ~3 km | 1984–2020 |
| SAGE II-CCI- OMPS | SAGE II v7<br>OSIRIS v5.10<br>MIPAS v7<br>SCIAMACHY UBr v3.5<br>GOMOS ALGOM 2s<br>ACE-FTS v3.5/3.6<br>OMPS USask v1.1.0 | Number density (anomalies) on altitude levels | 90°S–90°N,<br>10° latitude bands | 10–50 km,<br>1 km | 1984–2020 |
| SAGE II-OSIRIS-OMPS | SAGE II v7<br>OSIRIS v5.10<br>OMPS USask v1.1.0 | Number density (anomalies) on altitude levels | 60°S–60°N,<br>10° latitude bands | 0–50 km,<br>1 km | 1984–2020 |
| SAGE II-SCIAMACHY-OMPS | SAGE II v7<br>SCIAMACHY UBr v3.5<br>OMPS UBr | Number density (anomalies) on altitude levels | 90°S–90°N,<br>10° latitude bands | 9–64 km,<br>3–4 km | 1984–2020 |
| $BASIC_{SG}$ | SWOOSH v2.6<br>GOZCARDS v2.20 | Mixing ratio on pressure levels | 60°S–60°N,<br>10° latitude bands | 147–1 hPa<br>~3 km | 1985–2020 |

# REFERENCES


Abalos, M., C. Orbe, D.E. Kinnison, D. Plummer, L.D. Oman, P. Jöckel, O. Morgenstern, R.R. Garcia, G. Zeng, K.A. Stone, and M. Dameris, Future trends in stratosphere-to-troposphere transport in CCMI models, ***Atmos. Chem. Phys.***, ***20***, 6883–6901, doi:10.5194/acp-20-6883-2020, 2020.

Adcock, K.E., P.J. Fraser, B.D. Hall, R.L. Langenfelds, G. Lee, S.A. Montzka, D.E. Oram, T. Röckmann, F. Stroh, W.T. Sturges, B. Vogel, and J.C. Laube, Aircraft-based observations of ozone-depleting substances in the upper troposphere and lower stratosphere in and above the Asian summer monsoon, ***J. Geophys. Res.***, ***126*** (1), doi:10.1029/2020jd033137, 2021.

Alsing, J., dlmmc: Dynamical linear model regression for atmospheric time-series analysis, ***J. Open Source Softw.***, ***4*** (37), 1157, doi:10.21105/joss.01157, 2019.

Amos, M., P.J. Young, J.S. Hosking, J.-F. Lamarque, N.L. Abraham, H. Akiyoshi, A.T. Archibald, S. Bekki, M. Deushi, P. Jöckel, D. Kinnison, O. Kirner, M. Kunze, M. Marchand, D.A. Plummer, D. Saint-Martin, K. Sudo, S. Tilmes, and Y. Yamashita, Projecting ozone hole recovery using an ensemble of chemistry–climate models weighted by model performance and independence, ***Atmos. Chem. Phys.***, ***20***, 9961–9977, doi:10.5194/acp-20-9961-2020, 2020.

Anstey, J.A., and T.G. Shepherd, High-latitude influence of the quasi-biennial oscillation, ***Quart. J. Roy. Meteor. Soc.***, ***140***, 1–21, doi:10.1002/qj.2132, 2014.

Anstey, J.A., T.P. Banyard, N. Butchart, L. Coy, P.A. Newman, S. Osprey, and C.J. Wright, Prospect of increased disruption to the QBO in a changing climate, ***Geophys. Res. Lett.***, ***48*** (15), doi:10.1029/2021gl093058, 2021.

Arosio, C., A. Rozanov, E. Malinina, K.-U. Eichmann, T. von Clarmann, and J.P. Burrows, Retrieval of ozone profiles from OMPS limb scattering observations, ***Atmos. Meas. Tech.***, ***11***, 2135–2149, doi:10.5194/amt-11-2135-2018, 2018.

Arosio, C., A. Rozanov, E. Malinina, M. Weber, and J.P. Burrows, Merging of ozone profiles from SCIAMACHY, OMPS and SAGE II observations to study stratospheric ozone changes, ***Atmos. Meas. Tech.***, ***12***, 2423–2444, doi:10.5194/amt-12-2423-2019, 2019.

Ashok, K., S.K. Behera, S.A. Rao, H. Weng, and T. Yamagata, El Niño Modoki and its possible teleconnection, ***J. Geophys. Res.***, ***112*** (C11), doi:10.1029/2006jc003798, 2007.

Austin, J., K. Tourpali, E. Rozanov, H. Akiyoshi, S. Bekki, G. Bodeker, C. Brühl, N. Butchart, M. Chipperfield, M. Deushi, V.I. Fomichev, M.A. Giorgetta, L. Gray, K. Kodera, F. Lott, E. Manzini, D. Marsh, K. Matthes, T. Nagashima, K. Shibata, R.S. Stolarski, H. Struthers, and W. Tian, Coupled chemistry climate model simulations of the solar cycle in ozone and temperature, ***J. Geophys. Res.***, ***113*** (D11), doi:10.1029/2007jd009391, 2008.

Bai, K., N.-B. Chang, R. Shi, H. Yu, and W. Gao, An intercomparison of multidecadal observational and reanalysis data sets for global total ozone trends and variability analysis, ***J. Geophys. Res.***, ***122***, 7119–7139, doi:10.1002/2016JD025835, 2017.

Baldwin, M.P., L.J. Gray, T.J. Dunkerton, K. Hamilton, P.H. Haynes, W.J. Randel, J.R. Holton, M.J. Alexander, I. Hirota, T. Horinouchi, D.B.A. Jones, J.S. Kinnersley, C. Marquardt, K. Sato, and M. Takahashi, The quasi-biennial oscillation, ***Rev. Geophys.***, ***39***, 179–229, doi:10.1029/1999rg000073, 2001.

Ball, W.T., A. Kuchař, E.V. Rozanov, J. Staehelin, F. Tummon, A.K. Smith, T. Sukhodolov, A. Stenke, L. Revell, A. Coulon, W. Schmutz, and T. Peter, An upper-branch Brewer–Dobson circulation index for attribution of stratospheric variability and improved ozone and temperature trend analysis, ***Atmos. Chem. Phys.***, ***16***, 15,485–15,500, doi:10.5194/acp-16-15485-2016, 2016.

Ball, W.T., J. Alsing, D.J. Mortlock, E.V. Rozanov, F. Tummon, and J.D. Haigh, Reconciling differences in stratospheric ozone composites, ***Atmos. Chem. Phys.***, ***17***, 12,269–12,302, doi:10.5194/acp-17-12269-2017, 2017.

Ball, W.T., J. Alsing, D.J. Mortlock, J. Staehelin, J.D. Haigh, T. Peter, F. Tummon, R. Stübi, A. Stenke, J. Anderson, A. Bourassa, S.M. Davis, D. Degenstein, S. Frith, L. Froidevaux, C. Roth, V. Sofieva, R. Wang, J. Wild, P. Yu, J.R. Ziemke, and E.V. Rozanov, Evidence for a continuous decline in lower stratospheric ozone offsetting ozone layer recovery, ***Atmos. Chem. Phys.***, ***18*** (2), 1379–1394, doi:10.5194/acp-18-1379-2018, 2018.

Ball, W.T., J. Alsing, J. Staehelin, S.M. Davis, L. Froidevaux, and T. Peter, Stratospheric ozone trends for 1985–2018: sensitivity to recent large variability, ***Atmos. Chem. Phys.***, ***19***, 12,731–12,748, doi:10.5194/acp-19-12731-2019, 2019a.

Ball, W.T., E.V. Rozanov, J. Alsing, D.R. Marsh, F. Tummon, D.J. Mortlock, D. Kinnison, and J.D. Haigh, The upper stratospheric solar cycle ozone response, ***Geophys. Res. Lett.***, ***46***, 1831–1841, doi:10.1029/2018gl081501, 2019b.

Ball, W.T., G. Chiodo, M. Abalos, J. Alsing, and A. Stenke, Inconsistencies between chemistry–climate models and observed lower stratospheric ozone trends since 1998, ***Atmos. Chem. Phys.***, ***20***, 9737–9752, doi:10.5194/acp-20-9737-2020, 2020.

Banerjee, A., J.C. Fyfe, L.M. Polvani, D. Waugh, and K.-L. Chang, A pause in Southern Hemisphere circulation trends due to the Montreal Protocol, ***Nature***, ***579***, 544–548, doi:10.1038/s41586-020-2120-4, 2020.

Barrera, J.A., R.P. Fernandez, F. Iglesias-Suarez, C.A. Cuevas, J.-F. Lamarque, and A. Saiz-Lopez, Seasonal impact of biogenic very short-lived bromocarbons on lower-most stratospheric ozone between 60° N and 60° S during the 21st century, ***Atmos. Chem. Phys.***, ***20***, 8083–8102, doi:10.5194/acp-20-8083-2020, 2020.

Bates, K.H., and D.J. Jacob, An expanded definition of the odd oxygen family for tropospheric ozone budgets: Implications for ozone lifetime and stratospheric influence, ***Geophys. Res. Lett.***, ***47***, doi:10.1029/2019gl084486, 2020.

Bencherif, H., A.M. Toihir, N. Mbatha, V. Sivakumar, D.J. du Preez, N. Bègue, and G. Coetzee, Ozone variability and trend estimates from 20-years of ground-based and satellite observations at Irene Station, South Africa, ***Atmosphere***, ***11*** (11), 1216, doi:10.3390/atmos11111216, 2020.

Bernath, P., C. Boone, and J. Crouse, Wildfire smoke destroys stratospheric ozone, ***Science***, ***375***, 1292–1295, doi:10.1126/science.abm5611, 2022.

Bernet, L., I. Boyd, G. Nedoluha, R. Querel, D. Swart, and K. Hocke, Validation and trend analysis of stratospheric ozone data from ground-based observations at Lauder, New Zealand, ***Remote Sens.***, ***13*** (1), 109, doi:10.3390/rs13010109, 2020.

Blair, G.S., P. Henrys, A. Leeson, J. Watkins, E. Eastoe, S. Jarvis, and P.J. Young, Data science of the natural environment: a research roadmap, ***Front. Environ. Sci.***, ***7***, 121, doi:10.3389/fenvs.2019.00121, 2019.

Bodeker, G.E., B. Hassler, P.J. Young, and R.W. Portmann, A vertically resolved, global, gap-free ozone database for assessing or constraining global climate model simulations, ***Earth Syst. Sci. Data***, ***5***, 31–43, doi:10.5194/essd-5-31-2013, 2013.

Bodeker, G.E., J. Nitzbon, J.S. Tradowsky, S. Kremser, A. Schwertheim, and J. Lewis, A global total column ozone climate data record, ***Earth Syst. Sci. Data***, ***13*** (8), 3885–3906, doi:10.5194/essd-2020-218, 2020.

Boleti, E., C. Hueglin, S.K. Grange, A.S.H. Prévôt, and S. Takahama, Temporal and spatial analysis of ozone concentrations in Europe based on timescale decomposition and a multi-clustering approach, ***Atmos. Chem. Phys.***, ***20***, 9051–9066, doi:10.5194/acp-20-9051-2020, 2020.

Bourassa, A.E., D.A. Degenstein, W.J. Randel, J.M. Zawodny, E. Kyrölä, C.A. McLinden, C.E. Sioris, and C.Z. Roth, Trends in stratospheric ozone derived from merged SAGE II and Odin-OSIRIS satellite observations, ***Atmos. Chem. Phys.***, ***14***, 6983–6994, doi:10.5194/acp-14-6983-2014, 2014.

Bourassa, A.E., C.Z. Roth, D.J. Zawada, L.A. Rieger, C.A. McLinden, and D.A. Degenstein, Drift-corrected Odin-OSIRIS ozone product: algorithm and updated stratospheric ozone trends, ***Atmos. Meas. Tech.***, ***11***, 489–498, doi:10.5194/amt-11-489-2018, 2018.

Bourassa, A.E., L.A. Rieger, D.J. Zawada, S. Khaykin, L.W. Thomason, and D.A. Degenstein, Satellite limb observations of unprecedented forest fire aerosol in the stratosphere, ***J. Geophys. Res.***, ***124***, 9510–9519, doi:10.1029/2019jd030607, 2019.

Braesicke, P., and J. Neu, (Lead Authors), V. Fioletev, S. Godin-Beekman, D. Hubert, I. Petropalovskikh, M. Shiotani, and B.-M. Sinnhuber, Update on Global Ozone: Past, present, and Future, Chapter 3 in ***Scientific Assessment of Ozone Depletion: 2018***, World Meteorological Organization, 78 pp., Geneva, Switzerland, 2018.

Butchart, N., The Brewer-Dobson circulation, ***Rev. Geophys.***, ***52***, 157–184, doi:10.1002/2013rg000448, 2014.

Charlton-Perez, A.J., E. Hawkins, V. Eyring, I. Cionni, G.E. Bodeker, D.E. Kinnison, H. Akiyoshi, S.M. Frith, R. Garcia, A. Gettelman, J.F. Lamarque, T. Nakamura, S. Pawson, Y. Yamashita, S. Bekki, P. Braesicke, M.P. Chipperfield, S. Dhomse, M. Marchand, E. Mancini, O. Morgenstern, G. Pitari, D. Plummer, J.A. Pyle, E. Rozanov, J. Scinocca, K. Shibata, T.G. Shepherd, W. Tian, and D.W. Waugh, The potential to narrow uncertainty in projections of stratospheric ozone over the 21st century, ***Atmos. Chem. Phys.***, ***10*** (19), 9473–9486, doi:10.5194/acp-10-9473-2010, 2010.

Chen, Z., P.K. Bhartia, R. Loughman, P. Colarco, and M. DeLand, Improvement of stratospheric aerosol extinction retrieval from OMPS/LP using a new aerosol model, ***Atmos. Meas. Tech.***, ***11***, 6495–6509, doi:10.5194/amt-11-6495-2018, 2018.

Chen, Z., P.K. Bhartia, O. Torres, G. Jaross, R. Loughman, M. DeLand, P. Colarco, R. Damadeo, and G. Taha, Evaluation of the OMPS/LP stratospheric aerosol extinction product using SAGE III/ISS observations, ***Atmos. Meas. Tech.***, ***13***, 3471–3485, doi:10.5194/amt-13-3471-2020, 2020.

Chipperfield, M.P., S. Dhomse, R. Hossaini, W. Feng, M.L. Santee, M. Weber, J.P. Burrows, J.D. Wild, D. Loyola, and M. Coldewey-Egbers, On the cause of recent variations in lower stratospheric ozone, ***Geophys. Res. Lett.***, ***45***, 5718–5726, doi:10.1029/2018gl078071, 2018.

Chouza, F., T. Leblanc, J. Barnes, M. Brewer, P. Wang, and D. Koon, Long-term (1999–2019) variability of stratospheric aerosol over Mauna Loa, Hawaii, as seen by two co-located lidars and satellite measurements, ***Atmos. Chem. Phys.***, ***20***, 6821–6839, doi:10.5194/acp-20-6821-2020, 2020.

Cisewski, M., J. Zawodny, J. Gasbarre, R. Eckman, N. Topiwala, O. Rodriguez-Alvarez, D. Cheek, and S. Hall, The stratospheric aerosol and gas experiment (SAGE III) on the International Space Station (ISS) Mission, in ***Sensors, Systems, and Next-Generation Satellites XVIII***, ***9241***, 59–65, doi:10.1117/12.2073131, 2014.

Coddington, O., J.L. Lean, P. Pilewskie, M. Snow, and D. Lindholm, A solar irradiance climate data record, ***Bull. Am. Meteorol. Soc.***, ***97***, 1265–1282, doi:10.1175/BAMS-D-14-00265.1, 2016.

Coldewey-Egbers, M., D.G. Loyola R., P. Braesicke, M. Dameris, M. van Roozendael, C. Lerot, and W. Zimmer, A new health check of the ozone layer at global and regional scales, ***Geophys. Res. Lett.***, ***41***, 4363–4372, doi:10.1002/2014gl060212, 2014.

Coldewey-Egbers, M., D.G. Loyola, G. Labow, and S.M. Frith, Comparison of GTO-ECV and adjusted MERRA-2 total ozone columns from the last 2 decades and assessment of interannual variability, ***Atmos. Meas. Tech.***, ***13***, 1633–1654, doi:10.5194/amt-13-1633-2020, 2020.

Coldewey-Egbers, M., D.G. Loyola, C. Lerot, and M. Van Roozendael, Global, regional and seasonal analysis of total ozone trends derived from the 1995–2020 GTO-ECV climate data record, ***Atmos. Chem. Phys.***, ***22*** (10), 6861–6878, doi:10.5194/acp-2021-1047, 2022.

Collins, W.J., J.-F. Lamarque, M. Schulz, O. Boucher, V. Eyring, M.I. Hegglin, A. Maycock, G. Myhre, M. Prather, D. Shindell, and S.J. Smith, AerChemMIP: Quantifying the effects of chemistry and aerosols in CMIP6, ***Geosci. Model Dev.***, ***10***, 585–607, doi:10.5194/gmd-10-585-2017, 2017.

Coy, L., P.A. Newman, S. Pawson, and L.R. Lait, Dynamics of the disrupted 2015/16 Quasi-Biennial Oscillation , ***J. Clim.***, ***30***, 5661–5674, doi:10.1175/JCLI-D-16-0663.1, 2017.

Damadeo, R.P., J.M. Zawodny, and L.W. Thomason, Reevaluation of stratospheric ozone trends from SAGE II data using a simultaneous temporal and spatial analysis, ***Atmos. Chem. Phys.***, ***14***, 13,455–13,470, doi:10.5194/acp-14-13455-2014, 2014.

Dameris, M., P. Jöckel, and M. Nützel, Possible implications of enhanced chlorofluorocarbon-11 concentrations on ozone, ***Atmos. Chem. Phys.***, ***19***, 13,759–13,771, doi:10.5194/acp-19-13759-2019, 2019.

Davis, S.M., K.H. Rosenlof, B. Hassler, D.F. Hurst, W.G. Read, H. Vömel, H. Selkirk, M. Fujiwara, and R. Damadeo, The Stratospheric Water and Ozone Satellite Homogenized (SWOOSH) database: a long-term database for climate studies, ***Earth Syst. Sci. Data***, ***8***, 461–490, doi:10.5194/essd-8-461-2016, 2016.

Davis, S.M., M.I. Hegglin, M. Fujiwara, R. Dragani, Y. Harada, C. Kobayashi, C. Long, G.L. Manney, E.R. Nash, G.L. Potter, S. Tegtmeier, T. Wang, K. Wargan, and J.S. Wright, Assessment of upper tropospheric and stratospheric water vapor and ozone in reanalyses as part of S-RIP, ***Atmos. Chem. Phys.***, ***17***, 12,743–12,778, doi:10.5194/acp-17-12743-2017, 2017.

Davis, S.M., and M.I. Hegglin (Lead Authors), R. Dragani, M. Fujiwara, Y. Harada, C. Kobayashi, C. Long, G.L. Manney, E.R. Nash, G.L. Potter, S. Tegtmeier, T. Wang, K. Wargan, and J.S. Wright, Overview of ozone and water vapour, in ***SPARC Reanalysis Intercomparison Project (S-RIP) Final Report***, edited by M. Fujiwara, G.L.M.L. Gray, and J.S. Wright, SPARC Report No. 10, WCRP-6/2021, 121–162, doi:10.17874/800dee57d13, 2021.

Dhomse, S., M. Weber, I. Wohltmann, M. Rex, and J.P. Burrows, On the possible causes of recent increases in northern hemispheric total ozone from a statistical analysis of satellite data from 1979 to 2003, ***Atmos. Chem. Phys.***, ***6***, 1165–1180, doi:10.5194/acp-6-1165-2006, 2006.

Dhomse, S.S., M.P. Chipperfield, R.P. Damadeo, J.M. Zawodny, W.T. Ball, W. Feng, R. Hossaini, G.W. Mann, and J.D. Haigh, On the ambiguous nature of the 11 year solar cycle signal in upper stratospheric ozone, ***Geophys. Res. Lett.***, ***43***, 7241–7249, doi:10.1002/2016gl069958, 2016.

Dhomse, S.S., D. Kinnison, M.P. Chipperfield, R.J. Salawitch, I. Cionni, M.I. Hegglin, N.L. Abraham, H. Akiyoshi, A.T. Archibald, E.M. Bednarz, S. Bekki, P. Braesicke, N. Butchart, M. Dameris, M. Deushi, S. Frith, S.C. Hardiman, B. Hassler, L.W. Horowitz, R.-M. Hu, P. Jöckel, B. Josse, O. Kirner, S. Kremser, U. Langematz, J. Lewis, M. Marchand, M. Lin, E. Mancini, V. Marécal, M. Michou, O. Morgenstern, F.M. O'Connor, L. Oman, G. Pitari, D.A. Plummer, J.A. Pyle, L.E. Revell, E. Rozanov, R. Schofield, A. Stenke, K. Stone, K. Sudo, S. Tilmes, D. Visioni, Y. Yamashita, and G. Zeng, Estimates of ozone return dates from Chemistry-Climate Model Initiative simulations, ***Atmos. Chem. Phys.***, ***18***, 8409–8438, doi:10.5194/acp-18-8409-2018, 2018.

Dhomse, S.S., W. Feng, S.A. Montzka, R. Hossaini, J. Keeble, J.A. Pyle, J.S. Daniel, and M.P. Chipperfield, Delay in recovery of the Antarctic ozone hole from unexpected CFC-11 emissions, ***Nat. Commun.***, ***10***, 5781, doi:10.1038/s41467-019-13717-x, 2019.

Dhomse, S.S., C. Arosio, W. Feng, A. Rozanov, M. Weber, and M.P. Chipperfield, ML-TOMCAT: machine-learning-based satellite-corrected global stratospheric ozone profile data set from a chemical transport model, ***Earth Syst. Sci. Data***, ***13***, 5711–5729, doi:10.5194/essd-13-5711-2021, 2021.

Dhomse, S.S., M.P. Chipperfield, W. Feng, R. Hossaini, G.W. Mann, M.L. Santee, and M. Weber, A single-peak-structured solar cycle signal in stratospheric ozone based on Microwave Limb Sounder observations and model simulations, ***Atmos. Chem. Phys.***, ***22***, 903–916, doi:10.5194/acp-22-903-2022, 2022.

Dietmüller, S., H. Garny, R. Eichinger, and W.T. Ball, Analysis of recent lower-stratospheric ozone trends in chemistry climate models, ***Atmos. Chem. Phys.***, ***21***, 6811–6837, doi:10.5194/acp-21-6811-2021, 2021.

Domeisen, D.I.V., C.I. Garfinkel, and A.H. Butler, The teleconnection of El Niño southern oscillation to the stratosphere, ***Rev. Geophys.***, ***57*** (1), 5–47, doi:10.1029/2018rg000596, 2019.

Dudok de Wit, T., S. Bruinsma, and K. Shibasaki, Synoptic radio observations as proxies for upper atmosphere modelling, ***J. Space Weather Space Clim.***, ***4***, A06, doi:10.1051/swsc/2014003, 2014.

Dudok de Wit, T., and S. Bruinsma, The 30 cm radio flux as a solar proxy for thermosphere density modelling, ***J. Space Weather Space Clim.***, ***7***, A9, doi:10.1051/swsc/2017008, 2017.

Ermakova, T.S., O.G. Aniskina, I.A. Statnaia, M.A. Motsakov, and A.I. Pogoreltsev, Simulation of the ENSO influence on the extra-tropical middle atmosphere, ***Earth Planets Space***, ***71*** (1), 1–9, doi:10.1186/s40623-019-0987-9, 2019.

Errera, Q., S. Chabrillat, Y. Christophe, J. Debosscher, D. Hubert, W. Lahoz, M.L. Santee, M. Shiotani, S. Skachko, T. von Clarmann, and K. Walker, Technical note: Reanalysis of Aura MLS chemical observations, ***Atmos. Chem. Phys.***, ***19***, 13,647–13,679, doi:10.5194/acp-19-13647-2019, 2019.

Eyring, V., I. Cionni, G.E. Bodeker, A.J. Charlton-Perez, D.E. Kinnison, J.F. Scinocca, D.W. Waugh, H. Akiyoshi, S. Bekki, M.P. Chipperfield, M. Dameris, S. Dhomse, S.M. Frith, H. Garny, A. Gettelman, A. Kubin, U. Langematz, E. Mancini, M. Marchand, T. Nakamura, L.D. Oman, S. Pawson, G. Pitari, D.A. Plummer, E. Rozanov, T.G. Shepherd, K. Shibata, W. Tian, P. Braesicke, S.C. Hardiman, J.F. Lamarque, O. Morgenstern, J.A. Pyle, D. Smale, and Y. Yamashita, Multi-model assessment of stratospheric ozone return dates and ozone recovery in CCMVal-2 models, ***Atmos. Chem. Phys.***, ***10***, 9451–9472, doi:10.5194/acp-10-9451-2010, 2010.

Eyring, V., J.M. Arblaster, I. Cionni, J. Sedláček, J. Perlwitz, P.J. Young, S. Bekki, D. Bergmann, P. Cameron-Smith, W.J. Collins, G. Faluvegi, K.D. Gottschaldt, L.W. Horowitz, D.E. Kinnison, J.F. Lamarque, D.R. Marsh, D. Saint-Martin, D.T. Shindell, K. Sudo, S. Szopa, and S. Watanabe, Long-term ozone changes and associated climate impacts in CMIP5 simulations, ***J. Geophys. Res.***, ***108***, 5029–5060, doi:10.1002/jgrd.50316, 2013.

Eyring, V., S. Bony, G.A. Meehl, C.A. Senior, B. Stevens, R.J. Stouffer, and K.E. Taylor, Overview of the Coupled Model Intercomparison Project Phase 6 (CMIP6) experimental design and organization, ***Geosci. Model Dev.***, ***9*** (5), 1937–1958, doi:10.5194/gmd-9-1937-2016, 2016.

Fleming, E.L., P.A. Newman, Q. Liang, and J.S. Daniel, The impact of continuing CFC-11 emissions on stratospheric ozone, ***J. Geophys. Res.***, ***125*** (3), doi:10.1029/2019jd031849, 2020.

Fleming, E.L., Q. Liang, L.D. Oman, P.A. Newman, F. Li, and M.M. Hurwitz, Stratospheric impacts of continuing CFC-11 emissions simulated in a chemistry-climate model, ***J. Geophys. Res.***, ***126*** (9), doi:10.1029/2020jd033656, 2021.

Flemming, J., A. Benedetti, A. Inness, R.J. Engelen, L. Jones, V. Huijnen, S. Remy, M. Parrington, M. Suttie, A. Bozzo, V.-H. Peuch, D. Akritidis, and E. Katragkou, The CAMS interim reanalysis of carbon monoxide, ozone and aerosol for 2003–2015, ***Atmos. Chem. Phys.***, ***17***, 1945–1983, doi:10.5194/acp-17-1945-2017, 2017.

Frith, S.M., R.S. Stolarski, N.A. Kramarova, and R.D. McPeters, Estimating uncertainties in the SBUV Version 8.6 merged profile ozone data set, ***Atmos. Chem. Phys.***, ***17***, 14,695–14,707, doi:10.5194/acp-17-14695-2017, 2017.

Froidevaux, L., J. Anderson, H.-J. Wang, R.A. Fuller, M.J. Schwartz, M.L. Santee, N.J. Livesey, H.C. Pumphrey, P.F. Bernath, J.M. Russell III, and M.P. McCormick, Global OZone chemistry and related trace gas data records for the stratosphere (GOZCARDS): Methodology and sample results with a focus on HCl, H2O, and O3, ***Atmos. Chem. Phys.***, ***15*** (18), 10,471–10,507, doi:10.5194/acp-15-10471-2015, 2015.

Galytska, E., A. Rozanov, M.P. Chipperfield, S.S. Dhomse, M. Weber, C. Arosio, W. Feng, and J.P. Burrows, Dynamically controlled ozone decline in the tropical mid-stratosphere observed by SCIAMACHY, ***Atmos. Chem. Phys.***, ***19***, 767–783, doi:10.5194/acp-19-767-2019, 2019.

Garane, K., C. Lerot, M. Coldewey-Egbers, T. Verhoelst, M.E. Koukouli, I. Zyrichidou, D.S. Balis, T. Danckaert, F. Goutail, J. Granville, D. Hubert, A. Keppens, J.-C. Lambert, D. Loyola, J.-P. Pommereau, M. Van Roozendael, and C. Zehner, Quality assessment of the Ozone_cci Climate Research Data Package (release 2017) – Part 1: Ground-based validation of total ozone column data products, ***Atmos. Meas. Tech.***, ***11***, 1385–1402, doi:10.5194/amt-11-1385-2018, 2018.

García, O.E., E. Sanromá, M. Schneider, F. Hase, S.F. León-Luis, T. Blumenstock, E. Sepúlveda, A. Redondas, V. Carreño, C. Torres, and N. Prats, Improved ozone monitoring by ground-based FTIR spectrometry, ***Atmos. Meas. Tech.***, ***15***, 2557–2577, doi:10.5194/amt-15-2557-2022, 2022.

Garfinkel, C.I., D.W. Waugh, L.D. Oman, L. Wang, and M.M. Hurwitz, Temperature trends in the tropical upper troposphere and lower stratosphere: Connections with sea surface temperatures and implications for water vapor and ozone, ***J. Geophys. Res.***, ***118***, 9658–9672, doi:10.1002/jgrd.50772, 2013.

Gaudel, A., O.R. Cooper, G. Ancellet, B. Barret, A. Boynard, J.P. Burrows, C. Clerbaux, P.-F. Coheur, J. Cuesta, E. Cuevas, S. Doniki, G. Dufour, F. Ebojie, G. Foret, O. Garcia, M.J. Granados-Muñoz, J.W. Hannigan, F. Hase, B. Hassler, G. Huang, D. Hurtmans, D. Jaffe, N. Jones, P. Kalabokas, B. Kerridge, S. Kulawik, B. Latter, T. Leblanc, E. Le Flochmoën, W. Lin, J. Liu, X. Liu, E. Mahieu, A. McClure-Begley, J.L. Neu, M. Osman, M. Palm, H. Petetin, I. Petropavlovskikh, R. Querel, N. Rahpoe, A. Rozanov, M.G. Schultz, J. Schwab, R. Siddans, D. Smale, M. Steinbacher, H. Tanimoto, D.W. Tarasick, V. Thouret, A.M. Thompson, T. Trickl, E. Weatherhead, C. Wespes, H.M. Worden, C. Vigouroux, X. Xu, G. Zeng, and J. Ziemke, Tropospheric Ozone Assessment Report: Present-day distribution and trends of tropospheric ozone relevant to climate and global atmospheric chemistry model evaluation, ***Elementa (Wash., DC)***, ***6***, 39, doi:10.1525/elementa.291, 2018.

Gaudel, A., O.R. Cooper, K.-L. Chang, I. Bourgeois, J.R. Ziemke, S.A. Strode, L.D. Oman, P. Sellitto, P. Nédélec, R. Blot, V. Thouret, and C. Granier, Aircraft observations since the 1990s reveal increases of tropospheric ozone at multiple locations across the Northern Hemisphere, ***Sci. Adv.***, ***6*** (34), doi:10.1126/sciadv.aba8272, 2020.

Gidden, M.J., K. Riahi, S.J. Smith, S. Fujimori, G. Luderer, E. Kriegler, D.P. van Vuuren, M. van den Berg, L. Feng, D. Klein, K. Calvin, J.C. Doelman, S. Frank, O. Fricko, M. Harmsen, T. Hasegawa, P. Havlik, J. Hilaire, R. Hoesly, J. Horing, A. Popp, E. Stehfest, and K. Takahashi, Global emissions pathways under different socioeconomic scenarios for use in CMIP6: a dataset of harmonized emissions trajectories through the end of the century, ***Geosci. Model Dev.***, ***12***, 1443–1475, doi:10.5194/gmd-12-1443-2019, 2019.

Godin-Beekmann, S., N. Azouz, V. Sofieva, D. Hubert, I. Petropavlovskikh, P. Effertz, G. Ancellet, D. Degenstein, D. Zawada, L. Froidevaux, S. Frith, J. Wild, S. Davis, W. Steinbrecht, T. Leblanc, R. Querel, K. Tourpali, R. Damadeo, E. Maillard-Barras, R. Stübi, C. Vigouroux, C. Arosio, G. Nedoluha, I. Boyd, and R. van Malderen, Updated trends of the stratospheric ozone vertical distribution in the 60° S–60° N latitude range based on the LOTUS regression model, ***Atmos. Chem. Phys. Discuss.***, 1–28, doi:10.5194/acp-2022-137, 2022.

Griffiths, P.T., L.T. Murray, G. Zeng, Y.M. Shin, N.L. Abraham, A.T. Archibald, M. Deushi, L.K. Emmons, I.E. Galbally, B. Hassler, L.W. Horowitz, J. Keeble, J. Liu, O. Moeini, V. Naik, F.M. O'Connor, N. Oshima, D. Tarasick, S. Tilmes, S.T. Turnock, O. Wild, P.J. Young, and P. Zanis, Tropospheric ozone in CMIP6 simulations, ***Atmos. Chem. Phys.***, ***21***, 4187–4218, doi:10.5194/acp-21-4187-2021, 2021.

Gröbner, J., H. Schill, L. Egli, and R. Stübi, Consistency of total column ozone measurements between the Brewer and Dobson spectroradiometers of the LKO Arosa and PMOD/WRC Davos, ***Atmos. Meas. Tech.***, ***14***, 3319–3331, doi:10.5194/amt-14-3319-2021, 2021.

Haigh, J.D., The role of stratospheric ozone in modulating the solar radiative forcing of climate, ***Nature***, ***370***, 544–546, doi:10.1038/370544a0, 1994.

Harder, J.W., J.M. Fontenla, P. Pilewskie, E.C. Richard, and T.N. Woods, Trends in solar spectral irradiance variability in the visible and infrared, ***Geophys. Res. Lett.***, ***36*** (7), doi:10.1029/2008gl036797, 2009.

Hausfather, Z., and G.P. Peters, Emissions – the "business as usual" story is misleading, ***Nature***, ***577***, 618–620, doi:10.1038/d41586-020-00177-3, 2020.

Hawkins, E., and R. Sutton, The potential to narrow uncertainty in regional climate predictions, ***Bull. Am. Meteorol. Soc.***, ***90*** (8), 1095–1108, doi:10.1175/2009BAMS2607.1, 2009.

Hawkins, E., and R. Sutton, The potential to narrow uncertainty in projections of regional precipitation change, ***Clim. Dyn.***, ***37***, 407–418, doi:10.1007/s00382-010-0810-6, 2010.

Hegglin, M.I., S. Tegtmeier, J. Anderson, A.E. Bourassa, S. Brohede, D. Degenstein, L. Froidevaux, B. Funke, J. Gille, Y. Kasai, E.T. Kyrölä, J. Lumpe, D. Murtagh, J.L. Neu, K. Pérot, E.E. Remsberg, A. Rozanov, M. Toohey, J. Urban, T. von Clarmann, K.A. Walker, H.-J. Wang, C. Arosio, R. Damadeo, R.A. Fuller, G. Lingenfelser,, C. McLinden, D. Pendlebury, C. Roth, N.J. Ryan, C. Sioris, L. Smith, and K. Weigel, Overview and update of the SPARC Data Initiative: comparison of stratospheric composition measurements from satellite limb sounders, ***Earth Syst. Sci. Data***, ***13***, 1855–1903, doi:10.5194/essd-13-1855-2021, 2021.

Henley, B.J., J. Gergis, D.J. Karoly, S. Power, J. Kennedy, and C.K. Folland, A tripole index for the interdecadal Pacific oscillation, ***Clim. Dyn.***, ***45***, 3077–3090, doi:10.1007/s00382-015-2525-1, 2015.

Hersbach, H., B. Bell, P. Berrisford, S. Hirahara, A. Horányi, J. Muñoz-Sabater, J. Nicolas, C. Peubey, R. Radu, D. Schepers, A. Simmons, C. Soci, S. Abdalla, X. Abellan, G. Balsamo, P. Bechtold, G. Biavati, J. Bidlot, M. Bonavita, G. Chiara, P. Dahlgren, D. Dee, M. Diamantakis, R. Dragani, J. Flemming, R. Forbes, M. Fuentes, A. Geer, L. Haimberger, S. Healy, R.J. Hogan, E. Hólm, M. Janisková, S. Keeley, P, Laloyaux, P. Lopez, C. Lupu, G. Radnoti, P. Rosnay, I. Rozum, F. Vamborg, S. Villaume, and J.-N. Thépaut, The ERA5 global reanalysis, ***Quart. J. Roy. Meteor. Soc.***, ***146***, 1999–2049, doi:10.1002/qj.3803, 2020.

Hood, L.L., and B.E. Soukharev, Quasi-decadal variability of the tropical lower stratosphere: The role of extratropical wave forcing, ***J. Atmos. Sci.***, ***60***, 2389–2403, doi:10.1175/1520-0469(2003)060<2389:QVOTTL>2.0.CO;2, 2003.

Hossaini, R., M.P. Chipperfield, S.A. Montzka, A. Rap, S. Dhomse, and W. Feng, Efficiency of short-lived halogens at influencing climate through depletion of stratospheric ozone, ***Nat. Geosci.***, ***8***, 186–190, doi:10.1038/ngeo2363, 2015.

Hossaini, R., E. Atlas, S.S. Dhomse, M.P. Chipperfield, P.F. Bernath, A.M. Fernando, J. Mühle, A.A. Leeson, S.A. Montzka, W. Feng, J.J. Harrison, P. Krummel, M.K. Vollmer, S. Reimann, S. O'Doherty, D. Young, M. Maione, J. Arduini, and C.R. Lunder, Recent trends in stratospheric chlorine from very short-lived substances, ***J. Geophys. Res.***, ***124***, 2318–2335, doi:10.1029/2018JD029400, 2019.

Hu, Z.-Z., M.J. McPhaden, A. Kumar, J.-Y. Yu, and N.C. Johnson, Uncoupled El Niño warming, ***Geophys. Res. Lett.***, ***47*** (7), doi:10.1029/2020gl087621, 2020.

Huang, B., P.W. Thorne, V.F. Banzon, T. Boyer, G. Chepurin, J.H. Lawrimore, M.J. Menne, T.M. Smith, R.S. Vose, and H.-M. Zhang, Extended reconstructed sea surface temperature, version 5 (ERSSTv5): upgrades, validations, and intercomparisons, ***J. Clim.***, ***30***, 8179–8205, doi:10.1175/JCLI-D-16-0836.1, 2017.

Hubert, D., J.-C. Lambert, T. Verhoelst, J. Granville, A. Keppens, J.-L. Baray, A.E. Bourassa, U. Cortesi, D.A. Degenstein, L. Froidevaux, S. Godin-Beekmann, K.W. Hoppel, B.J. Johnson, E. Kyrölä, T. Leblanc, G. Lichtenberg, M. Marchand, C.T. McElroy, D. Murtagh, H. Nakane, T. Portafaix, R. Querel, J.M. Russell III, J. Salvador, H.G.J. Smit, K. Stebel, W. Steinbrecht, K.B. Strawbridge, R. Stübi, D.P.J. Swart, G.

Taha, D.W. Tarasick, A.M. Thompson, J. Urban, J.A.E. van Gijsel, R. Van Malderen, P. von der Gathen, K.A. Walker, E. Wolfram, and J.M. Zawodny, Ground-based assessment of the bias and long-term stability of 14 limb and occultation ozone profile data records, ***Atmos. Meas. Tech.***, ***9***, 2497–2534, doi:10.5194/amt-9-2497-2016, 2016.

Hubert, D., K.-P. Heue, J.-C. Lambert, T. Verhoelst, M. Allaart, S. Compernolle, P.D. Cullis, A. Dehn, C. Félix, B.J. Johnson, A. Keppens, D.E. Kollonige, C. Lerot, D. Loyola, M. Maata, S. Mitro, M. Mohamad, A. Piters, F. Romahn, H.B. Selkirk, F.R. da Silva, R.M. Stauffer, A.M. Thompson, J.P. Veefkind, H. Vömel, J.C. Witte, and C. Zehner, TROPOMI tropospheric ozone column data: geophysical assessment and comparison to ozonesondes, GOME-2B and OMI, ***Atmos. Meas. Tech.***, ***14***, 7405–7433, doi:10.5194/amt-14-7405-2021, 2021.

Huijnen, V., K. Miyazaki, J. Flemming, A. Inness, T. Sekiya, and M.G. Schultz, An intercomparison of tropospheric ozone reanalysis products from CAMS, CAMS interim, TCR-1, and TCR-2, ***Geosci. Model Dev.***, ***13***, 1513–1544, doi:10.5194/gmd-13-1513-2020, 2020.

Iglesias-Suarez, F., P.J. Young, and O. Wild, Stratospheric ozone change and related climate impacts over 1850–2100 as modelled by the ACCMIP ensemble, ***Atmos. Chem. Phys.***, ***16***, 343–363, doi:10.5194/acp-16-343-2016, 2016.

Iglesias-Suarez, F., O. Wild, D.E. Kinnison, R.R. Garcia, D.R. Marsh, J. Lamarque, E.M. Ryan, S.M. Davis, R. Eichinger, A. Saiz-Lopez, and P.J. Young, Tropical stratospheric circulation and ozone coupled to pacific multi-decadal variability, ***Geophys. Res. Lett.***, ***48*** (11), doi:10.1029/2020gl092162, 2021.

Inness, A., J. Flemming, K.-P. Heue, C. Lerot, D. Loyola, R. Ribas, P. Valks, M. van Roozendael, J. Xu, and W. Zimmer, Monitoring and assimilation tests with TROPOMI data in the CAMS system: near-real-time total column ozone, ***Atmos. Chem. Phys.***, ***19***, 3939–3962, doi:10.5194/acp-19-3939-2019, 2019a.

Inness, A., M. Ades, A. Agustí-Panareda, J. Barré, A. Benedictow, A.-M. Blechschmidt, J.J. Dominguez, R. Engelen, H. Eskes, J. Flemming, V. Huijnen, L. Jones, Z. Kipling, S. Massart, M. Parrington, V.-H. Peuch, M. Razinger, S. Remy, M. Schulz, and M. Suttie, The CAMS reanalysis of atmospheric composition, ***Atmos. Chem. Phys.***, ***19***, 3515–3556, doi:10.5194/acp-19-3515-2019, 2019b.

Isaksen, I.S.A., E. Hesstvedt, and F. Stordal, Influence of stratospheric cooling from CO2 on the ozone layer, ***Nature***, ***283***, 189–191, doi:10.1038/283189a0, 1980.

Junge, C.E., C.W. Chagnon, and J.E. Manson, Stratospheric aerosols, ***J. Atmos. Sci.***, ***18*** (1), 81–108, doi:10.1175/1520-0469(1961)018<0081:SA>2.0.CO;2, 1961.

Kablick III, G.P., D.R. Allen, M.D. Fromm, and G.E. Nedoluha, Australian PyroCb smoke generates synoptic-scale stratospheric anticyclones, ***Geophys. Res. Lett.***, ***47*** (13), doi:10.1029/2020gl088101, 2020.

Kar, J., K.-P. Lee, M.A. Vaughan, J.L. Tackett, C.R. Trepte, D.M. Winker, P.L. Lucker, and B.J. Getzewich, CALIPSO level 3 stratospheric aerosol profile product: version 1.00 algorithm description and initial assessment, ***Atmos. Meas. Tech.***, ***12***, 6173–6191, doi:10.5194/amt-12-6173-2019, 2019.

Keeble, J., E.M. Bednarz, A. Banerjee, N.L. Abraham, N.R.P. Harris, A.C. Maycock, and J.A. Pyle, Diagnosing the radiative and chemical contributions to future changes in tropical column ozone with the UM-UKCA chemistry–climate model, ***Atmos. Chem. Phys.***, ***17***, 13,801–13,818, doi:10.5194/acp-17-13801-2017, 2017.

Keeble, J., N.L. Abraham, A.T. Archibald, M.P. Chipperfield, S. Dhomse, P.T. Griffiths, and J.A. Pyle, Modelling the potential impacts of the recent, unexpected increase in CFC-11 emissions on total column ozone recovery, ***Atmos. Chem. Phys.***, ***20***, 7153–7166, doi:10.5194/acp-20-7153-2020, 2020.

Keeble, J., B. Hassler, A. Banerjee, R. Checa-Garcia, G. Chiodo, S. Davis, V. Eyring, P.T. Griffiths, O. Morgenstern, P. Nowack, G. Zeng, J. Zhang, G. Bodeker, S. Burrows, P. Cameron-Smith, D. Cugnet, C. Danek, M. Deushi, L.W. Horowitz, A. Kubin, L. Li, G. Lohmann, M. Michou, M.J. Mills, P. Nabat, D. Olivié, S. Park, Ø. Seland, J. Stoll, K.-H. Wieners, and T. Wu, Evaluating stratospheric ozone and water vapour changes in CMIP6 models from 1850 to 2100, ***Atmos. Chem. Phys.***, ***21***, 5015–5061, doi:10.5194/acp-21-5015-2021, 2021a.

Keeble, J., Y.Y.S. Yiu, A.T. Archibald, F. O'Connor, A. Sellar, J. Walton, and J.A. Pyle, Using machine learning to make computationally inexpensive projections of 21st Century stratospheric column ozone changes in the tropics, ***Front Earth Sci.***, ***8***, 591, doi:10.3389/feart.2020.592667, 2021b.

Khaykin, S., B. Legras, S. Bucci, P. Sellitto, L. Isaksen, F. Tencé, S. Bekki, A. Bourassa, L. Rieger, D. Zawada, J. Jumelet, and S. Godin-Beekmann, The 2019/20 Australian wildfires generated a persistent smoke-charged vortex rising up to 35 km altitude, ***Commun. Earth Environ.***, ***1*** (1), 1–12, doi:10.1038/s43247-020-00022-5, 2020.

Klekociuk, A.R., M.B. Tully, P.B. Krummel, S.I. Henderson, D. Smale, R. Querel, S. Nichol, S.P. Alexander, P.J. Fraser, and G. Nedoluha, The Antarctic ozone hole during 2018 and 2019, ***J. South. Hemisphere Earth Syst. Sci.***, ***71***, 66–91, doi:10.1071/ES20010, 2021.

Kloss, C., G. Berthet, P. Sellitto, F. Ploeger, S. Bucci, S. Khaykin, F. Jégou, G. Taha, L.W. Thomason, B. Barret, E. Le Flochmoen, M. von Hobe, A. Bossolasco, N. Bègue, and B. Legras, Transport of the 2017 Canadian wildfire plume to the tropics via the Asian monsoon circulation, ***Atmos. Chem. Phys.***, ***19***, 13,547–13,567, doi:10.5194/acp-19-13547-2019, 2019.

Knutti, R., D. Masson, and A. Gettelman, Climate model genealogy: Generation CMIP5 and how we got there, ***Geophys. Res. Lett.***, ***40***, 1194–1199, doi:10.1002/grl.50256, 2013.

Kovilakam, M., L.W. Thomason, N. Ernest, L. Rieger, A. Bourassa, and L. Millán, The global space-based stratospheric aerosol climatology (version 2.0): 1979–2018, ***Earth Syst. Sci. Data***, ***12***, 2607–2634, doi:10.5194/essd-12-2607-2020, 2020.

Kremser, S., L.W. Thomason, M. von Hobe, M. Hermann, T. Deshler, C. Timmreck, M. Toohey, A. Stenke, J.P. Schwarz, R. Weigel, S. Fueglistaler, F.J. Prata, J.-P., Vernier, H. Schlager, J.E. Barnes, J.-C. Antuña-Marrero, D. Fairlie, M. Palm, E. Mahieu, J. Notholt, M. Rex, C. Bingen, F. Vanhellemont, A. Bourassa, J.M.C. Plane, D. Klocke, S.A. Carn, L. Clarisse, T. Trickl, R. Neely, A.D. James, L. Rieger, J.C. Wilson, and B. Meland, Stratospheric aerosol—Observations, processes, and impact on climate, ***Rev. Geophys.***, ***54***, 278–335, doi:10.1002/2015rg000511, 2016.

Krivova, N.A., L.E.A. Vieira, and S.K. Solanki, Reconstruction of solar spectral irradiance since the Maunder minimum, ***J. Geophys. Res.***, ***115*** (A12), doi:10.1029/2010ja015431, 2010.

Krzyścin, J.W., El Niño-Southern Oscillation and Indian Ocean Dipole contribution to the zonal mean total ozone in the Northern Hemisphere, ***Int. J. Climatol.***, ***37***, 3517–3524, doi:10.1002/joc.4933, 2017.

Kunze, M., T. Kruschke, U. Langematz, M. Sinnhuber, T. Reddmann, and K. Matthes, Quantifying uncertainties of climate signals in chemistry climate models related to the 11-year solar cycle – Part 1: Annual mean response in heating rates, temperature, and ozone, ***Atmos. Chem. Phys.***, ***20***, 6991–7019, doi:10.5194/acp-20-6991-2020, 2020.

Laine, M., N. Latva-Pukkila, and E. Kyrölä, Analysing time-varying trends in stratospheric ozone time series using the state space approach, ***Atmos. Chem. Phys.***, ***14***, 9707–9725, doi:10.5194/acp-14-9707-2014, 2014.

Lamarque, J.F., D.T. Shindell, B. Josse, P.J. Young, I. Cionni, V. Eyring, D. Bergmann, P. Cameron-Smith, W.J. Collins, R. Doherty, S. Dalsoren, G. Faluvegi, G. Folberth, S.J. Ghan, L.W. Horowitz, Y.H. Lee, I.A. MacKenzie, T. Nagashima, V. Naik, D. Plummer, M. Righi, S.T. Rumbold, M. Schulz, R.B. Skeie, D.S. Stevenson, S. Strode, K. Sudo, S. Szopa, A. Voulgarakis, and G. Zeng, The Atmospheric Chemistry and Climate Model Intercomparison Project (ACCMIP): overview and description of models, simulations and climate diagnostics, ***Geosci. Model Dev.***, ***6***, 179–206, doi:10.5194/gmd-6-179-2013, 2013.

Langematz, U., F. Schmidt, M. Kunze, G.E. Bodeker, and P. Braesicke, Antarctic ozone depletion between 1960 and 1980 in observations and chemistry–climate model simulations, ***Atmos. Chem. Phys.***, ***16***, 15,619–15,627, doi:10.5194/acp-16-15619-2016, 2016.

Li, F., P. Newman, S. Pawson, and J. Perlwitz, Effects of greenhouse gas increase and stratospheric ozone depletion on stratospheric mean age of air in 1960-2010, ***J. Geophys. Res.***, ***123***, 2098–2110, doi:10.1002/2017jd027562, 2018.

Li, K.-F., Q. Zhang, K.-K. Tung, and Y.L. Yung, Resolving a long-standing model-observation discrepancy on ozone solar cycle response, ***Earth Space Sci.***, ***3***, 431–440, doi:10.1002/2016ea000199, 2016.

Lin, J., and T. Qian, Impacts of the ENSO lifecycle on stratospheric ozone and temperature, ***Geophys. Res. Lett.***, ***46***, 10,646–10,658, doi:10.1029/2019gl083697, 2019.

Lin, P., I. Held, and Y. Ming, The early development of the 2015/16 quasi-biennial oscillation disruption, ***J. Atmos. Sci.***, ***76***, 821–836, doi:10.1175/JAS-D-18-0292.1, 2019.

Loyola, D.G., and M. Coldewey-Egbers, Multi-sensor data merging with stacked neural networks for the creation of satellite long-term climate data records, ***EURASIP J. Adv. Signal Process.***, ***2012*** (1), 1–10, doi:10.1186/1687-6180-2012-91, 2012.

Lu, J., F. Xie, W. Tian, J. Li, W. Feng, M. Chipperfield, J. Zhang, and X. Ma, Interannual variations in lower stratospheric ozone during the period 1984–2016, ***J. Geophys. Res.***, ***124***, 8225–8241, doi:10.1029/2019jd030396, 2019.

Maillard Barras, E., A. Haefele, L. Nguyen, F. Tummon, W.T. Ball, E.V. Rozanov, R.

Rüfenacht, K. Hocke, L. Bernet, N. Kämpfer, G. Nedoluha, and I. Boyd, Study of the dependence of long-term stratospheric ozone trends on local solar time, ***Atmos. Chem. Phys.***, ***20***, 8453–8471, doi:10.5194/acp-20-8453-2020, 2020.

Matthes, K., D.R. Marsh, R.R. Garcia, D.E. Kinnison, F. Sassi, and S. Walters, Role of the QBO in modulating the influence of the 11 year solar cycle on the atmosphere using constant forcings, ***J. Geophys. Res.***, ***115*** (D18), doi:10.1029/2009jd013020, 2010.

Matthes, K., B. Funke, M.E. Andersson, L. Barnard, J. Beer, P. Charbonneau, M.A. Clilverd, T. Dudok de Wit, M. Haberreiter, A. Hendry, C.H. Jackman, M. Kretzschmar, T. Kruschke, M. Kunze, U. Langematz, D.R. Marsh, A.C. Maycock, S. Misios, C.J. Rodger, A.A. Scaife, A. Seppälä, M. Shangguan, M. Sinnhuber, K. Tourpali, I. Usoskin, M. van de Kamp, P.T. Verronen, and S. Versick, Solar forcing for CMIP6 (v3.2), ***Geosci. Model Dev.***, ***10***, 2247–2302, doi:10.5194/gmd-10-2247-2017, 2017.

Mauceri, S., E. Richard, P. Pilewskie, D. Harber, O. Coddington, S. Béland, M. Chambliss, and S. Carson, Degradation correction of TSIS SIM, ***Solar Phys., 295*** (11), doi:10.1007/s11207-020-01707-y, 2020.

Maycock, A.C., K. Matthes, S. Tegtmeier, R. Thiéblemont, and L. Hood, The representation of solar cycle signals in stratospheric ozone – Part 1: A comparison of recently updated satellite observations, ***Atmos. Chem. Phys.***, ***16***, 10,021–10,043, doi:10.5194/acp-16-10021-2016, 2016.

Maycock, A.C., K. Matthes, S. Tegtmeier, H. Schmidt, R. Thiéblemont, L. Hood, H. Akiyoshi, S. Bekki, M. Deushi, P. Jöckel, O. Kirner, M. Kunze, M. Marchand, D.R. Marsh, M. Michou, D. Plummer, L.E. Revell, E. Rozanov, A. Stenke, Y. Yamashita, and K. Yoshida, The representation of solar cycle signals in stratospheric ozone – Part 2: Analysis of global models, ***Atmos. Chem. Phys.***, ***18***, 11,323–11,343, doi:10.5194/acp-18-11323-2018, 2018.

McPeters, R., S. Frith, N. Kramarova, J. Ziemke, and G. Labow, Trend quality ozone from NPP OMPS: the version 2 processing, ***Atmos. Meas. Tech.***, ***12***, 977–985, doi:10.5194/amt-12-977-2019, 2019.

Meehl, G.A., R. Moss, K.E. Taylor, V. Eyring, R.J. Stouffer, S. Bony, and B. Stevens, Climate model intercomparisons: Preparing for the next phase, ***Eos Trans. AGU***, ***95*** (9), 77–78, doi:10.1002/2014EO090001, 2014.

Meinshausen, M., Z.R.J. Nicholls, J. Lewis, M.J. Gidden, E. Vogel, M. Freund, U. Beyerle, C. Gessner, A. Nauels, N. Bauer, J.G. Canadell, J.S. Daniel, A. John, P.B. Krummel, G. Luderer, N. Meinshausen, S.A. Montzka, P.J. Rayner, S. Reimann, S.J. Smith, M. van den Berg, G.J.M. Velders, M.K. Vollmer, and R.H.J. Wang, The shared socio-economic pathway (SSP) greenhouse gas concentrations and their extensions to 2500, ***Geosci. Model Dev.***, ***13***, 3571–3605, doi:10.5194/gmd-13-3571-2020, 2020.

Mettig, N., M. Weber, A. Rozanov, C. Arosio, J.P. Burrows, P. Veefkind, A.M. Thompson, R. Querel, T. Leblanc, S. Godin-Beekmann, R. Kivi, and M.B. Tully, Ozone profile retrieval from nadir TROPOMI measurements in the UV range, ***Atmos. Meas. Tech.***, ***14***, 6057–6082, doi:10.5194/amt-14-6057-2021, 2021.

Meul, S., M. Dameris, U. Langematz, J. Abalichin, A. Kerschbaumer, A. Kubin, and S. Oberländer-Hayn, Impact of rising greenhouse gas concentrations on future tropical ozone and UV exposure, ***Geophys. Res. Lett.***, ***43*** (6), 2919–2927, doi:10.1002/2016GL067997, 2016.

Meul, S., U. Langematz, P. Kröger, S. Oberländer-Hayn, and P. Jöckel, Future changes in the stratosphere-to-troposphere ozone mass flux and the contribution from climate change and ozone recovery, ***Atmos. Chem. Phys.***, ***18***, 7721–7738, doi:10.5194/acp-18-7721-2018, 2018.

Monks, P.S., A.T. Archibald, A. Colette, O. Cooper, M. Coyle, R. Derwent, D. Fowler, C. Granier, K.S. Law, G.E. Mills, D.S. Stevenson, O. Tarasova, V. Thouret, E. von Schneidemesser, R. Sommariva, O. Wild, and M.L. Williams, Tropospheric ozone and its precursors from the urban to the global scale from air quality to short-lived climate forcer, ***Atmos. Chem. Phys.***, ***15***, 8889–8973, doi:10.5194/acp-15-8889-2015, 2015.

Montzka, S.A., G.S. Dutton, P. Yu, E. Ray, R.W. Portmann, J.S. Daniel, L. Kuijpers, B.D. Hall, D. Mondeel, C. Siso, J.D. Nance, M. Rigby, A.J. Manning, L. Hu, F. Moore, B.R Miller, and J.W. Elkins, An unexpected and persistent increase in global emissions of ozone-depleting CFC-11, ***Nature***, ***557***, 413–417, doi:10.1038/s41586-018-0106-2, 2018.

Morgenstern, O., M.I. Hegglin, E. Rozanov, F.M. O'Connor, N.L. Abraham, H. Akiyoshi, A.T. Archibald, S. Bekki, N. Butchart, M.P. Chipperfield, M. Deushi, S.S. Dhomse, R.R. Garcia, S.C. Hardiman, L.W. Horowitz, P. Jöckel, B. Josse, D. Kinnison, M. Lin, E. Mancini, M.E. Manyin, M. Marchand, V. Marécal, M. Michou, L.D. Oman, G. Pitari, D.A. Plummer, L.E. Revell, D. Saint-Martin, R. Schofield, A. Stenke, K. Stone, K. Sudo, T.Y. Tanaka, S. Tilmes, Y. Yamashita, K. Yoshida, and G. Zeng, Review of the global models used within phase 1 of the Chemistry–Climate Model Initiative (CCMI), ***Geosci. Model Dev.***, ***10***, 639–671, doi:10.5194/gmd-10-639-2017, 2017.

Morgenstern, O., K.A. Stone, R. Schofield, H. Akiyoshi, Y. Yamashita, D.E. Kinnison, R.R. Garcia, K. Sudo, D.A. Plummer, J. Scinocca, L.D. Oman, M.E. Manyin, G. Zeng, E. Rozanov, A. Stenke, L.E. Revell, G. Pitari, E. Mancini, G.D. Genova, D. Visioni, S.S. Dhomse, and M.P. Chipperfield, Ozone sensitivity to varying greenhouse gases and ozone-depleting substances in CCMI-1 simulations, ***Atmos. Chem. Phys.***, ***18***, 1091–1114, doi:10.5194/acp-18-1091-2018, 2018.

Morgenstern, O., F.M. O'Connor, B.T. Johnson, G. Zeng, J.P. Mulcahy, J. Williams, J. Teixeira, M. Michou, P. Nabat, L.W. Horowitz, V. Naik, L.T. Sentman, M. Deushi, S.E. Bauer, K. Tsigaridis, D.T. Shindell, and D.E. Kinnison, Reappraisal of the climate impacts of ozone-depleting substances, ***Geophys. Res. Lett.***, ***47*** (20), doi:10.1029/2020gl088295, 2020.

Newchurch, M.J., E.-S. Yang, D.M. Cunnold, G.C. Reinsel, J.M. Zawodny, and J.M. Russell III, Evidence for slowdown in stratospheric ozone loss: First stage of ozone recovery, ***J. Geophys. Res.***, ***108*** (D16), doi:10.1029/2003jd003471, 2003.

Newman, P.A., J.S. Daniel, D.W. Waugh, and E.R. Nash, A new formulation of equivalent effective stratospheric chlorine (EESC), ***Atmos. Chem. Phys.***, ***7***, 4537–4552, doi:10.5194/acp-7-4537-2007, 2007.

Newman, P.A., L. Coy, S. Pawson, and L.R. Lait, The anomalous change in the QBO in 2015-2016, ***Geophys. Res. Lett.***, ***43***, 8791–8797, doi:10.1002/2016gl070373, 2016.

Nowack, P., P. Braesicke, J. Haigh, N.L. Abraham, J. Pyle, and A. Voulgarakis, Using machine learning to build temperature-based ozone parameterizations for climate sensitivity simulations, ***Environ. Res. Lett.***, ***13*** (10), 104016, doi:10.1088/1748-9326/aae2be, 2018.

Nowack, P., J. Runge, V. Eyring, and J.D. Haigh, Causal networks for climate model evaluation and constrained projections, ***Nat. Commun.***, ***11*** (1), doi:10.1038/s41467-020-15195-y, 2020.

Olsen, M.A., G.L. Manney, and J. Liu, The ENSO and QBO impact on ozone variability and stratosphere-troposphere exchange relative to the subtropical jets, ***J. Geophys. Res.***, ***124*** (13), 7379–7392, doi:10.1029/2019jd030435, 2019.

Oman, L.D., A.R. Douglass, J.R. Ziemke, J.M. Rodriguez, D.W. Waugh, and J.E. Nielsen, The ozone response to ENSO in Aura satellite measurements and a chemistry-climate simulation, ***J. Geophys. Res.***, ***118***, 965–976, doi:10.1029/2012jd018546, 2013.

O'Neill, B.C., C. Tebaldi, D.P. van Vuuren, V. Eyring, P. Friedlingstein, G. Hurtt, R. Knutti, E. Kriegler, J.-F. Lamarque, J. Lowe, G.A. Meehl, R. Moss, K. Riahi, and B.M. Sanderson, The scenario model intercomparison project (ScenarioMIP) for CMIP6, ***Geosci. Model Dev.***, ***9***, 3461–3482, doi:10.5194/gmd-9-3461-2016, 2016.

Orbe, C., K. Wargan, S. Pawson, and L.D. Oman, Mechanisms linked to recent ozone decreases in the northern hemisphere lower stratosphere, ***J. Geophys. Res.***, ***125*** (9), doi:10.1029/2019jd031631, 2020.

ORM (Ozone Research Managers), ***Report of Part II of the Eleventh Meeting of the Ozone Research Managers of the Parties to the Vienna Convention for the Protection of the Ozone Layer***, GAW (Global Atmospheric Watch)–Report No. 271, 538 pp., Geneva, Switzerland, 2021.

Orr, A., H. Lu, P. Martineau, E.P. Gerber, G.J. Marshall, and T.J. Bracegirdle, Is our dynamical understanding of the circulation changes associated with the Antarctic ozone hole sensitive to the choice of reanalysis dataset?, ***Atmos. Chem. Phys.***, ***21***, 7451–7472, doi:10.5194/acp-21-7451-2021, 2021.

Osprey, S.M., N. Butchart, J.R. Knight, A.A. Scaife, K. Hamilton, J.A. Anstey, V. Schenzinger, and C. Zhang, An unexpected disruption of the atmospheric quasi-biennial oscillation, ***Science***, ***353***, 1424–1427, doi:10.1126/science.aah4156, 2016.

Petropavlovskikh, I., K. Miyagawa, A. McClure-Beegle, B. Johnson, J. Wild, S. Strahan, K. Wargan, R. Querel, L. Flynn, E. Beach, G. Ancellet, and S. Godin-Beekmann, Optimized Umkehr profile algorithm for ozone trend analyses, ***Atmos. Meas. Tech.***, ***15***, 1849–1870, doi:/10.5194/amt-15-1849-2022, 2022.

Polvani, L.M., L. Wang, M. Abalos, N. Butchart, M.P. Chipperfield, M. Dameris, M. Deushi, S.S. Dhomse, P. Jöckel, D. Kinnison, M. Michou, O. Morgenstern, L.D. Oman, D.A. Plummer, and K.A. Stone, Large impacts, past and future, of ozone-depleting substances on Brewer-Dobson circulation trends: A multi-model assessment, ***J. Geophys. Res.***, ***124***, 6669–6680, doi:10.1029/2018JD029516, 2019.

Provost, F., and T. Fawcett, Data science and its relationship to big data and data-driven decision making, ***Big Data, 1*** (1), 51–59, doi:10.1089/big.2013.1508, 2013.

Pyle, J.A., J. Keeble, N.L. Abraham, M.P. Chipperfield, and P.T. Griffiths, Integrated ozone depletion as a metric for ozone recovery, ***Nature***, ***608***, 719–723, doi:10.17863/CAM.86155, 2022.

Rahpoe, N., M. Weber, A.V. Rozanov, K. Weigel, H. Bovensmann, J.P. Burrows, A. Laeng, G. Stiller, T. von Clarmann, E. Kyrölä, V.F. Sofieva, J. Tamminen, K. Walker, D. Degenstein, A.E. Bourassa, R. Hargreaves, P. Bernath, J. Urban, and D.P. Murtagh, Relative drifts and biases between six ozone limb satellite measurements from the last decade, ***Atmos. Meas. Tech.***, ***8***, 4369–4381, doi:10.5194/amt-8-4369-2015, 2015.

Randel, W.J., and F. Wu, Isolation of the ozone QBO in SAGE II data by singular-value decomposition, ***J. Atmos. Sci.***, ***53***, 2546–2559, doi:10.1175/1520-0469(1996)053<2546:IOTOQI>2.0.CO;2, 1996.

Randel, W.J., R.R. Garcia, N. Calvo, and D. Marsh, ENSO influence on zonal mean temperature and ozone in the tropical lower stratosphere, ***Geophys. Res. Lett.***, ***36*** (15), doi:10.1029/2009gl039343, 2009.

Redondas, A., R. Evans, R. Stuebi, U. Köhler, and M. Weber, Evaluation of the use of five laboratory-determined ozone absorption cross sections in Brewer and Dobson retrieval algorithms, ***Atmos. Chem. Phys.***, ***14***, 1635–1648, doi:10.5194/acp-14-1635-2014, 2014.

Reutter, P., B. Škerlak, M. Sprenger, and H. Wernli, Stratosphere–troposphere exchange (STE) in the vicinity of North Atlantic cyclones, ***Atmos. Chem. Phys.***, ***15***, 10,939–10,953, doi:10.5194/acp-15-10939-2015, 2015.

Revell, L.E., A. Stenke, F. Tummon, A. Feinberg, E. Rozanov, T. Peter, N.L. Abraham, H. Akiyoshi, A.T. Archibald, N. Butchart, M. Deushi, P. Jöckel, D. Kinnison, M. Michou, O. Morgenstern, F.M. O'Connor, L.D. Oman, G. Pitari, D.A. Plummer, R. Schofield, K. Stone, S. Tilmes, D. Visioni, Y. Yamashita, and G. Zeng, Tropospheric ozone in CCMI models and Gaussian process emulation to understand biases in the SOCOLv3 chemistry-climate model, ***Atmos. Chem. Phys.***, ***18***, 16,155–16,172, doi:10.5194/acp-18-16155-2018, 2018.

Riahi, K., D.P. van Vuuren, E. Kriegler, J. Edmonds, B.C. O'Neill, S. Fujimori, N. Bauer, K. Calvin, R. Dellink, O. Fricko, W. Lutz, A. Popp, J.C. Cuaresma, S. Kc, M. Leimbach, L. Jiang, T. Kram, S. Rao, J. Emmerling, K. Ebi, T. Hasegawa, P. Havlik, F. Humpenöder, L.A. Da Silva, S. Smith, E. Stehfest, V. Bosetti, J. Eom, D. Gernaat, T. Masui, J. Rogelj, J. Strefler, L. Drouet, V. Krey, G. Luderer, M. Harmsen, K. Takahashi, L. Baumstark, J.C. Doelman, M. Kainuma, Z. Klimont, G. Marangoni, H. Lotze-Campen, M. Obersteiner, A. Tabeau, and M. Tavoni, The shared socioeconomic pathways and their energy, land use, and greenhouse gas emissions implications: an overview, ***Glob. Environ. Change***, ***42***, 153–168, doi:10.1016/j.gloenvcha.2016.05.009, 2017.

Rieder, H.E., J. Staehelin, J.A. Maeder, T. Peter, M. Ribatet, A.C. Davison, R. Stübi, P. Weihs, and F. Holawe, Extreme events in total ozone over Arosa – Part 2: Fingerprints of atmospheric dynamics and chemistry and effects on mean values and long-term changes, ***Atmos. Chem. Phys.***, ***10***, 10,033–10,045, doi:10.5194/acp-10-10033-2010, 2010.

Rieger, L.A., D.J. Zawada, A.E. Bourassa, and D.A. Degenstein, A multiwavelength retrieval approach for improved OSIRIS aerosol extinction retrievals, ***J. Geophys. Res.***, ***124*** (13), 7286–7307 doi:10.1029/2018jd029897, 2019.

Rieger, L.A., W.J. Randel, A.E. Bourassa, and S. Solomon, Stratospheric temperature and ozone anomalies associated with the 2020 Australian New Year fires, ***Geophys. Res. Lett.***, ***48*** (24), doi:10.1029/2021gl095898, 2021.

Rigby, M., S. Park, T. Saito, L.M. Western, A.L. Redington, X. Fang, S. Henne, A.J. Manning, R.G. Prinn, G.S. Dutton, P.J. Fraser, A.L. Ganesan, B.D. Hall, C.M. Harth, J. Kim, K.-R. Kim, P.B. Krummel, T. Lee, S. Li, Q. Liang, M.F. Lunt, S.A. Montzka, J. Mühle, S. O'Doherty, M.-K. Park, S. Reimann, P.K. Salameh, P. Simmonds, R.L. Tunnicliffe, R.F. Weiss, Y. Yokouchi, and D. Young, Increase in CFC-11 emissions from eastern China based on atmospheric observations, ***Nature***, ***569***, 546–550, doi:10.1038/s41586-019-1193-4, 2019.

Rosanka, S., B. Franco, L. Clarisse, P.-F. Coheur, A. Pozzer, A. Wahner, and D. Taraborrelli, The impact of organic pollutants from Indonesian peatland fires on the tropospheric and lower stratospheric composition, ***Atmos. Chem. Phys.***, ***21***, 11,257–11,288, doi:10.5194/acp-21-11257-2021, 2021.

Runge, J., P. Nowack, M. Kretschmer, S. Flaxman, and D. Sejdinovic, Detecting and quantifying causal associations in large nonlinear time series datasets, ***Sci. Adv.***, ***5*** (11), doi:10.1126/sciadv.aau4996, 2019.

Santee, M.L., A. Lambert, G.L. Manney, N.J. Livesey, L. Froidevaux, J.L. Neu, M.J. Schwartz, L.F. Millán, F. Werner, W.G. Read, M. Park, R.A. Fuller, and B.M. Ward, Prolonged and pervasive perturbations in the composition of the southern hemisphere midlatitude lower stratosphere from the Australian new year's fires, ***Geophys. Res. Lett.***, ***49*** (4), doi:10.1029/2021gl096270, 2022.

Saunders, M.A., A.S.R. Lea, and J.R. Smallwood, The quasi-biennial oscillation: A second disruption in four years, ***Earth Space Sci. Open Archive***, doi:10.1002/essoar.10504326.1, 2020.

Schultz, M.G., S. Schröder, O. Lyapina, O. Cooper, I. Galbally, I. Petropavlovskikh, E. Von Schneidemesser, H. Tanimoto, Y. Elshorbany, M. Naja, R. Seguel, U. Dauert, P. Eckhardt, S. Feigenspahn, M. Fiebig, A.-G. Hjellbrekke, Y.-D. Hong, P.C. Kjeld, H. Koide, G. Lear, D. Tarasick, M. Ueno, M. Wallasch, D. Baumgardner, M.-T. Chuang, R. Gillett, M. Lee, S. Molloy, R. Moolla, T. Wang, K. Sharps, J.A. Adame, G. Ancellet, F. Apadula, P. Artaxo, M. Barlasina, M. Bogucka, P. Bonasoni, L. Chang, A. Colomb, E. Cuevas, M. Cupeiro, A. Degorska, A. Ding, M. Fröhlich, M. Frolova, H. Gadhavi, F. Gheusi, S. Gilge, M.Y. Gonzalez, V. Gros, S.H. Hamad, D. Helmig, D. Henriques, O. Hermansen, R. Holla, J. Huber, U. Im, D.A. Jaffe, N. Komala, D. Kubistin, K.-S. Lam, T. Laurila, H. Lee, I. Levy, C. Mazzoleni, L. Mazzoleni, A. McClure-Begley, M. Mohamad, M. Murovic, M. Navarro-Comas, F. Nicodim, D. Parrish, K.A. Read, N. Reid, L. Ries, P. Saxena, J.J. Schwab, Y. Scorgie, I. Senik, P. Simmonds, V. Sinha, A. Skorokhod, G. Spain, W. Spangl, R. Spoor, S.R. Springston, K. Steer, M. Steinbacher, E. Suharguniyawan, P. Torre, T. Trickl, L. Weili, R. Weller, X. Xu, L. Xue, and M. Zhiqiang, Tropospheric ozone assessment report: Database and metrics data of global surface ozone observations, ***Elementa (Wash., DC)***, ***5***, 58, doi:10.1525/elementa.244, 2017.

Schwartz, M.J., M.L. Santee, H.C. Pumphrey, G.L. Manney, A. Lambert, N.J. Livesey, L. Millán, J.L. Neu, W.G. Read, and F. Werner, Australian new year's PyroCb impact on stratospheric composition, ***Geophys. Res. Lett.***, ***47*** (24), doi:10.1029/2020gl090831, 2020.

Sengupta, U., M. Amos, J.S. Hosking, C.E. Rasmussen, M. Juniper, and P.J. Young, Ensembling geophysical models with Bayesian neural networks, ***Adv. Neural Inf. Process. Syst.***, ***33***, 1205–1217, doi:10.48550/arXiv.2010.03561, 2020.

Serdyuchenko, A., V. Gorshelev, M. Weber, W. Chehade, and J.P. Burrows, High spectral resolution ozone absorption cross-sections – Part 2: Temperature dependence, ***Atmos. Meas. Tech.***, ***7***, 625–636, doi:10.5194/amt-7-625-2014, 2014.

Shangguan, M., W. Wang, and S. Jin, Variability of temperature and ozone in the upper troposphere and lower stratosphere from multi-satellite observations and reanalysis data, ***Atmos. Chem. Phys.***, ***19***, 6659–6679, doi:10.5194/acp-19-6659-2019, 2019.

Shepherd, T.G., D.A. Plummer, J.F. Scinocca, M.I. Hegglin, V.E. Fioletov, M.C. Reader, E. Remsberg, T. von Clarmann, and H.J. Wang, Reconciliation of halogen-induced ozone loss with the total-column ozone record, ***Nat. Geosci.***, ***7***, 443–449, doi:10.1038/ngeo2155, 2014.

Shin, N.-Y., J.-S. Kug, F.S. McCormack, and N.J. Holbrook, The double-peaked El Niño and its physical processes, ***J. Clim.***, ***34***, 1291–1303, doi:10.1175/JCLI-D-20-0402.1, 2021.

Simmons, A.J., P. Poli, D.P. Dee, P. Berrisford, H. Hersbach, S. Kobayashi, and C. Peubey, Estimating low-frequency variability and trends in atmospheric temperature using ERA-Interim, ***Quart. J. Roy. Meteor. Soc.***, ***140***, 329–353, doi:10.1002/qj.2317, 2014.

Sinnhuber, B.-M., and S. Meul, Simulating the impact of emissions of brominated very short lived substances on past stratospheric ozone trends, ***Geophys. Res. Lett.***, ***42***, 2449–2456, doi:10.1002/2014gl062975, 2015.

Smit, H.G.J., and A.M. Thompson, ***Ozonesonde measurement principles and best operational practices: ASOPOS 2.0 (Assessment of Standard Operating Procedures for Ozonesondes)***, World Meteorological Organization, GAW Report No. 268, 173 pp., Geneva, Switzerland, 2021.

Sofiev, M., R. Kouznetsov, R. Hänninen, and V.F. Sofieva, Technical note: Intermittent reduction of the stratospheric ozone over northern Europe caused by a storm in the Atlantic Ocean, ***Atmos. Chem. Phys.***, ***20***, 1839–1847, doi:10.5194/acp-20-1839-2020, 2020.

Sofieva, V.F., E. Kyrölä, M. Laine, J. Tamminen, D. Degenstein, A. Bourassa, C. Roth, D. Zawada, M. Weber, A. Rozanov, N. Rahpoe, G. Stiller, A. Laeng, T. von Clarmann, K.A. Walker, P. Sheese, D. Hubert, M. van Roozendael, C. Zehner, R. Damadeo, J. Zawodny, N. Kramarova, and P.K. Bhartia, Merged SAGE II, Ozone_cci and OMPS ozone profile dataset and evaluation of ozone trends in the stratosphere, ***Atmos. Chem. Phys.***, ***17***, 12,533–12,552, doi:10.5194/acp-17-12533-2017, 2017.

Sofieva, V.F., M. Szeląg, J. Tamminen, E. Kyrölä, D. Degenstein, C. Roth, D. Zawada, A. Rozanov, C. Arosio, J.P. Burrows, M. Weber, A. Laeng, G.P. Stiller, T. von Clarmann, L. Froidevaux, N. Livesey, M. van Roozendael, and C. Retscher, Measurement report: regional trends of stratospheric ozone evaluated using the MErged GRIdded Dataset of Ozone Profiles (MEGRIDOP), ***Atmos. Chem. Phys.***, ***21***, 6707–6720, doi:10.5194/acp-21-6707-2021, 2021.

Solomon, S., K. Dube, K. Stone, P. Yu, D. Kinnison, O.B. Toon, S.E. Strahan, K.H. Rosenlof, R. Portmann, S. Davis, W. Randel, P. Bernarth, C. Boone, C.G. Bardeen, A. Bourassa, D. Zawada, and D. Degenstein, On the stratospheric chemistry of mid-latitude wildfire smoke, ***Proc. Natl. Acad. Sci.***, ***118*** (10), doi:10.1073/pnas.2117325119, 2022.

Soukharev, B.E., and L.L. Hood, Solar cycle variation of stratospheric ozone: Multiple regression analysis of long-term satellite data sets and comparisons with models, ***J. Geophys. Res.***, ***111*** (D20), doi:10.1029/2006jd007107, 2006.

SPARC (Stratospheric Processes And their Role in Climate), ***SPARC CCMVal Report on the Evaluation of Chemistry-Climate Models***, edited by V. Eyring, T. Shepherd, and D. Waugh, SPARC Report No. 5, WCRP-30/2010, WMO/TD – No. 40, [available at: www.sparc-climate.org/publications/sparc-reports/], 2010.

SPARC/IO3C/GAW, ***SPARC/IO3C/GAW Report on Long-term Ozone Trends and Uncertainties in the Stratosphere***, edited by I. Petropavlovskikh, S. Godin-Beekmann, D. Hubert, R. Damadeo, B. Hassler, and V. Sofieva, SPARC Report No. 9, GAW Report No. 241, WCRP-17/2018, doi:10.17874/f899e57a20b, 2019.

SPARC (Stratospheric Processes And their Role in Climate), ***SPARC Reanalysis Intercomparison Project (S-RIP) Final Report***, edited by M. Fujiwara, G.L. Manney, L.J. Gray, and J.S. Wright, SPARC Report No. 10, WCRP-17/2020, doi:10.17874/800dee57d13, 2022.

Stauffer, R.M., A.M. Thompson, L.D. Oman, and S.E. Strahan, The effects of a 1998 observing system change on MERRA-2-based ozone profile simulations, ***J. Geophys. Res.***, ***124*** (13), 7429–7441 doi:10.1029/2019jd030257, 2019.

Stauffer, R.M., A.M. Thompson, D.E. Kollonige, J.C. Witte, D.W. Tarasick, J. Davies, H. Vömel, G.A. Morris, R. Van Malderen, B.J. Johnson, R.R. Querel, H.B. Selkirk, R. Stübi, and H.G.J. Smit, A post-2013 dropoff in total ozone at a third of global ozonesonde stations: Electrochemical concentration cell instrument artifacts?, ***Geophys. Res. Lett.***, ***47*** (11), doi:10.1029/2019gl086791, 2020.

Steinbrecht, W., U. Köhler, H. Claude, M. Weber, J.P. Burrows, and R.J. van der A, Very high ozone columns at northern mid-latitudes in 2010, ***Geophys. Res. Lett.***, ***38*** (6), doi:10.1029/2010gl046634, 2011.

Steinbrecht, W., L. Froidevaux, R. Fuller, R. Wang, J. Anderson, C. Roth, A. Bourassa, D. Degenstein, R. Damadeo, J. Zawodny, S. Frith, R. McPeters, P. Bhartia, J. Wild, C. Long, S. Davis, K. Rosenlof, V. Sofieva, K. Walker, N. Rahpoe, A. Rozanov, M. Weber, A. Laeng, T. von Clarmann, G. Stiller, N. Kramarova, S. Godin-Beekmann, T. Leblanc, R. Querel, D. Swart, I. Boyd, K. Hocke, N. Kämpfer, E. Maillard Barras, L. Moreira, G. Nedoluha, C. Vigouroux, T. Blumenstock, M. Schneider, O. García, N. Jones, E. Mahieu, D. Smale, M. Kotkamp, J. Robinson, I. Petropavlovskikh, N. Harris, B. Hassler, D. Hubert, and F. Tummon, An update on ozone profile trends for the period 2000 to 2016, ***Atmos. Chem. Phys.***, ***17***, 10,675–10,690, doi:10.5194/acp-17-10675-2017, 2017.

Steinbrecht, W., M.I. Hegglin, N. Harris, and M. Weber, Is global ozone recovering?, ***C. R. Geosci.***, ***350***, 368–375, doi:10.1016/j.crte.2018.07.012, 2018.

Sterl, A., On the (in) homogeneity of reanalysis products, ***J. Clim.***, ***17***, 3866–3873, doi:10.1175/1520-0442(2004)017<3866:OTIORP>2.0.CO;2, 2004.

Stevenson, D.S., P.J. Young, V. Naik, J.F. Lamarque, D.T. Shindell, A. Voulgarakis, R.B. Skeie, S.B. Dalsøren, G. Myhre, T.K. Berntsen, G.A. Folberth, S.T. Rumbold, W.J. Collins, I.A. MacKenzie, R.M. Doherty, G. Zeng, T.P.C. van Noije, A. Strunk, D. Bergmann, P. Cameron-Smith, D.A. Plummer, S.A. Strode, L. Horowitz, Y.H. Lee, S. Szopa, K. Sudo, T. Nagashima, B. Josse, I. Cionni, M. Righi, V. Eyring, A. Conley, K.W. Bowman, O. Wild, and A. Archibald, Tropospheric ozone changes, radiative forcing and attribution to emissions in the Atmospheric Chemistry and Climate Model Intercomparison Project (ACCMIP), ***Atmos. Chem. Phys.***, ***13*** (6), 3063–3085, doi:10.5194/acp-13-3063-2013, 2013.

Stohl, A., A 1-year Lagrangian "climatology" of airstreams in the Northern Hemisphere troposphere and lowermost stratosphere, ***J. Geophys. Res.***, ***106*** (D7), 7263–7279, doi:10.1029/2000jd900570, 2001.

Stone, K.A., S. Solomon, and D.E. Kinnison, On the identification of ozone recovery, ***Geophys. Res. Lett.***, ***45***, 5158–5165, doi:10.1029/2018gl077955, 2018.

Strahan, S. D. Smale, S. Solomon, G. Taha, M.R. Damonm S.D. Steerod, N. Jones, B. Liley, R. Querel, and J. Robinson, Unexpected repartitioning of stratospheric inorganic chlorine after the 2020 Australian wildfires, ***Geophys. Res. Lett.***, ***49*** (14), doi: 10.1029/2022GL098290, 2022.

Stübi, R., H. Schill, E. Maillard Barras, J. Klausen, and A. Haefele, Quality assessment of Dobson spectrophotometers for ozone column measurements before and after automation at Arosa and Davos, ***Atmos. Meas. Tech.***, ***14***, 4203–4217, doi:10.5194/amt-14-4203-2021, 2021.

Szatkowski, L.S., O.H. Bradley Jr, L.E. Mauldin III, M.B. Wusk, W.P. Chu, L.C. Farwell II, and P. Galeone, Stratospheric aerosol and gas experiment III (SAGE III) mission aboard the International Space Station, in ***Optical Spectroscopic Techniques and Instrumentation for Atmospheric and Space Research III***, ***3756,*** 164–171, doi:10.1117/12.366370, 1999.

Szeląg, M.E., V.F. Sofieva, D. Degenstein, C. Roth, S. Davis, and L. Froidevaux, Seasonal stratospheric ozone trends over 2000–2018 derived from several merged data sets, ***Atmos. Chem. Phys.***, ***20***, 7035–7047, doi:10.5194/acp-20-7035-2020, 2020.

Tarasick, D., I.E. Galbally, O.R. Cooper, M.G. Schultz, G. Ancellet, T. Leblanc, T.J. Wallington, J. Ziemke, X. Liu, M. Steinbacher, J. Staehelin, C. Vigouroux, J.W. Hannigan, O. García, G. Foret, P. Zanis, E. Weatherhead, I. Petropavlovskikh, H. Worden, M. Osman, J. Liu, K.-L. Chang, A. Gaudel, M. Lin, M. Granados-Muñoz, A.M. Thompson, S.J. Oltmans, J. Cuesta, G. Dufour, V. Thouret, B. Hassler, T. Trickl, and J.L. Neu, Tropospheric Ozone Assessment Report: Tropospheric ozone from 1877 to 2016, observed levels, trends and uncertainties, ***Elementa (Wash., DC)***, ***7***, 39, doi:10.1525/elementa.376, 2019.

Tarasick, D.W., H.G.J. Smit, A.M. Thompson, G.A. Morris, J.C. Witte, J. Davies, T. Nakano, R. Van Malderen, R.M. Stauffer, B.J. Johnson, R. Stübi, S.J. Oltmans, and H. Vömel, Improving ECC ozonesonde data quality: Assessment of current methods and outstanding issues, ***Earth Space Sci.***, ***8*** (3), doi:10.1029/2019ea000914, 2021.

Thomason, L.W., N. Ernest, L. Millán, L. Rieger, A. Bourassa, J.-P. Vernier, G. Manney, B. Luo, F. Arfeuille, and T. Peter, A global space-based stratospheric aerosol climatology: 1979–2016, ***Earth Syst. Sci. Data***, ***10***, 469–492, doi:10.5194/essd-10-469-2018, 2018.

Thompson, A.M., R.M. Stauffer, K. Wargan, J.C. Witte, D.E. Kollonige, and J.R. Ziemke, Regional and seasonal trends in tropical ozone from SHADOZ profiles: Reference for models and satellite products, ***J. Geophys. Res.***, ***126*** (22), doi:10.1029/2021jd034691, 2021.

Tung, K.K., and H. Yang, Global QBO in circulation and ozone. Part I: Reexamination of observational evidence, ***J. Atmos. Sci.***, ***51***, 2699–2707, doi:10.1175/1520-0469(1994)051<2699:GQICAO>2.0.CO;2, 1994.

Tweedy, O.V., N.A. Kramarova, S.E. Strahan, P.A. Newman, L. Coy, W.J. Randel, M. Park, D.W. Waugh, and S.M. Frith, Response of trace gases to the disrupted 2015–2016 quasi-biennial oscillation, ***Atmos. Chem. Phys.***, ***17***, 6813–6823, doi:10.5194/acp-17-6813-2017, 2017.

van der A, R.J., M.A.F. Allaart, and H.J. Eskes, Multi sensor reanalysis of total ozone, ***Atmos. Chem. Phys.***, ***10***, 11,277–11,294, doi:10.5194/acp-10-11277-2010, 2010.

van der A, R.J., M.A.F. Allaart, and H.J. Eskes, Extended and refined multi sensor reanalysis of total ozone for the period 1970–2012, ***Atmos. Meas. Tech.***, ***8***, 3021–3035, doi:10.5194/amt-8-3021-2015, 2015.

Veefkind, J.P., I. Aben, K. McMullan, H. Förster, J. de Vries, G. Otter, J. Claas, H.J. Eskes, J.F. de Haan, Q. Kleipool, M. van Weele, O. Hasekamp, R. Hoogeveen, J. Landgraf, R. Snel, P. Tol, P. Ingmann, R. Voors, B. Kruizinga, R. Vink, H. Visser, and P.F. Levelt, TROPOMI on the ESA Sentinel-5 Precursor: A GMES mission for global observations of the atmospheric composition for climate, air quality and ozone layer applications, ***Remote Sens. Environ.***, ***120***, 70–83, doi:10.1016/j.rse.2011.09.027, 2012.

Vigouroux, C., T. Blumenstock, M. Coffey, Q. Errera, O. García, N.B. Jones, J.W. Hannigan, F. Hase, B. Liley, E. Mahieu, J. Mellqvist, J. Notholt, M. Palm, G. Persson, M. Schneider, C. Servais, D. Smale, L. Thölix, and M. De Mazière, Trends of ozone total columns and vertical distribution from FTIR observations at eight NDACC stations around the globe, ***Atmos. Chem. Phys.***, ***15***, 2915–2933, doi:10.5194/acp-15-2915-2015, 2015.

von der Gathen, P., R. Kivi, I. Wohltmann, R.J. Salawitch, and M. Rex, Climate change favours large seasonal loss of Arctic ozone, ***Nat. Commun.***, ***12***, 3886, doi:10.1038/s41467-021-24089-6, 2021.

Voulgarakis, A., D.T. Shindell, and G. Faluvegi, Linkages between ozone-depleting substances, tropospheric oxidation and aerosols, ***Atmos. Chem. Phys.***, ***13*** (9), 4907–4916, doi:10.5194/acp-13-4907-2013, 2013.

Wallace, J.M., R. Lee Panetta, and J. Estberg, Representation of the equatorial stratospheric quasi-biennial oscillation in EOF phase space, ***J. Atmos. Sci.***, ***50***, 1751–1762, doi:10.1175/1520-0469(1993)050<1751:ROTESQ>2.0.CO;2, 1993.

Wang, H.J.R., R. Damadeo, D. Flittner, N. Kramarova, G. Taha, S. Davis, A.M. Thompson, S. Strahan, Y. Wang, L. Froidevaux, D. Degenstein, A. Bourassa, W. Steinbrecht, K.A. Walker, R. Querel, T. Leblanc, S. Godin-Beekmann, D. Hurst, and E. Hall, Validation of SAGE III/ISS solar occultation ozone products with correlative satellite and ground-based measurements, ***J. Geophys. Res.***, ***125***, doi:10.1029/2020jd032430, 2020.

Wargan, K., C. Orbe, S. Pawson, J.R. Ziemke, L.D. Oman, M.A. Olsen, L. Coy, and K.E. Knowland, Recent decline in extratropical lower stratospheric ozone attributed to circulation changes, ***Geophys. Res. Lett.***, ***45***, 5166–5176, doi:10.1029/2018GL077406, 2018.

Wargan, K., N. Kramarova, B. Weir, S. Pawson, and S.M. Davis, Toward a reanalysis of stratospheric ozone for trend studies: Assimilation of the aura microwave limb sounder and ozone mapping and profiler suite limb profiler data, ***J. Geophys. Res.***, ***125*** (4), doi:10.1029/2019jd031892, 2020.

Weber, M., M. Coldewey-Egbers, V.E. Fioletov, S.M. Frith, J.D. Wild, J.P. Burrows, C.S. Long, and D. Loyola, Total ozone trends from 1979 to 2016 derived from five merged observational datasets – the emergence into ozone recovery, ***Atmos. Chem. Phys.***, ***18***, 2097–2117, doi:10.5194/acp-18-2097-2018, 2018.

Weber, M., W. Steinbrecht, C. Arosio, R. van der A, S.M. Frith, J. Anderson, M. Coldewey-Egbers, S. Davis, D. Degenstein, V.E. Fioletov, L. Froidevaux, D. Hubert, C.S. Long, D. Loyola, A. Rozanov, C. Roth, V. Sofieva, K. Tourpali, R. Wang, and J.D. Wild, Stratospheric ozone, in [State of the Climate in 2019], ***Bull. Am. Met. Soc.***, ***101*** (8), S78–S81, doi:10.1175/BAMS-D-20-0104.1, 2020.

Weber, M., W. Steinbrecht, C. Arosio, R. van der A, S.M. Frith, J. Anderson, L. Castia, M. Coldewey-Egbers, S. Davis, D. Degenstein, V.E. Fioletov, L. Froidevaux, D. Hubert, D. Loyola, C. Roth, A. Rozanov, V. Sofieva, K. Tourpali, R. Wang, and J.D. Wild, Stratospheric ozone, [State of the Climate in 2020], ***Bull. Am. Met. Soc.***, ***102*** (8), S92–S95, doi:10.1175/2021BAMSStateoftheClimate.1, 2021.

Weber, M., C. Arosio, M. Coldewey-Egbers, V. Fioletov, S.M. Frith, J.D. Wild, K. Tourpali, J.P. Burrows, and D. Loyola, Global total ozone recovery trends derived from five merged ozone datasets, ***Atmos. Chem. Phys.***, ***22***, 6843–6859, doi:10.5194/acp-22-6843-2022, 2022.

Wild, J.D., S.-K. Yang, and C.S. Long, Ozone Profile Trends: An SBUV/2 Perspective (QOS2016-133), in ***Proceedings of the Quadrennial Ozone Symposium***, Edinburgh, Scotland, 2016.

Wild, O., A. Voulgarakis, F. O'Connor, J.-F. Lamarque, E.M. Ryan, and L. Lee, Global sensitivity analysis of chemistry–climate model budgets of tropospheric ozone and OH: exploring model diversity, ***Atmos. Chem. Phys.***, ***20***, 4047–4058, doi:10.5194/acp-20-4047-2020, 2020.

Wilks, D.S., On "field significance" and the false discovery rate, ***J. Appl. Meteorol. Climatol.***, ***45***, 1181–1189, doi:10.1175/JAM2404.1, 2006.

Williams, R.S., M.I. Hegglin, B.J. Kerridge, P. Jöckel, B.G. Latter, and D.A. Plummer, Characterising the seasonal and geographical variability in tropospheric ozone, stratospheric influence and recent changes, ***Atmos. Chem. Phys.***, ***19***, 3589–3620, doi:10.5194/acp-19-3589-2019, 2019.

Wing, R., W. Steinbrecht, S. Godin-Beekmann, T.J. McGee, J.T. Sullivan, G. Sumnicht, G. Ancellet, A. Hauchecorne, S. Khaykin, and P. Keckhut, Intercomparison and evaluation of ground- and satellite-based stratospheric ozone and temperature profiles above Observatoire de Haute-Provence during the Lidar Validation NDACC Experiment (LAVANDE), ***Atmos. Meas. Tech.***, ***13***, 5621–5642, doi:10.5194/amt-13-5621-2020, 2020.

Wing, R., S. Godin-Beekmann, W. Steinbrecht, T.J. McGee, J.T. Sullivan, S. Khaykin, G. Sumnicht, and L. Twigg, Evaluation of the new DWD ozone and temperature lidar during the Hohenpeißenberg Ozone Profiling Study (HOPS) and comparison of results with previous NDACC campaigns, ***Atmos. Meas. Tech.***, ***14***, 3773–3794, doi:10.5194/amt-14-3773-2021, 2021.

WMO (World Meteorological Organization), ***Scientific Assessment of Ozone Depletion: 2014***, Global Ozone Research and Monitoring Project–Report No. 55, 416 pp., Geneva, Switzerland, 2014.

WMO (World Meteorological Organization), ***Scientific Assessment of Ozone Depletion: 2018***, Global Ozone Research and Monitoring Project–Report No. 58, 588 pp., Geneva, Switzerland, 2018.

WMO (World Meteorological Organization), ***Report on the Unexpected Emissions of CFC-11***, Ozone Research and Monitoring, WMO-No. 1268, 84 pp., Geneva, Switzerland, 2021.

Wolter, K., and M.S. Timlin, Measuring the strength of ENSO events: How does 1997/98 rank?, ***Weather***, ***53*** (9), 315–324, doi:10.1002/j.1477-8696.1998.tb06408.x, 1998.

Yeo, K.L., N.A. Krivova, S.K. Solanki, and K.H. Glassmeier, Reconstruction of total and spectral solar irradiance from 1974 to 2013 based on KPVT, SoHO/MDI, and SDO/HMI observations, ***Astron. Astrophys. Suppl. Ser.***, ***570***, A85, doi:10.1051/0004-6361/201423628, 2014.

Yeung, L.Y., L.T. Murray, P. Martinerie, E. Witrant, H. Hu, A. Banerjee, A. Orsi, and J. Chappellaz, Isotopic constraint on the twentieth-century increase in tropospheric ozone, ***Nature***, ***570***, 224–227, doi:10.1038/s41586-019-1277-1, 2019.

Young, P.J., A.T. Archibald, K.W. Bowman, J.F. Lamarque, V. Naik, D.S. Stevenson, S. Tilmes, A. Voulgarakis, O. Wild, D. Bergmann, P. Cameron-Smith, I. Cionni, W.J. Collins, S.B. Dalsøren, R.M. Doherty, V. Eyring, G. Faluvegi, L.W. Horowitz, B. Josse, Y.H. Lee, I.A. MacKenzie, T. Nagashima, D.A. Plummer, M. Righi, S.T. Rumbold, R.B. Skeie, D.T. Shindell, S.A. Strode, K. Sudo, S. Szopa, and G. Zeng, Pre-industrial to end 21st century projections of tropospheric ozone from the Atmospheric Chemistry and Climate Model Intercomparison Project (ACCMIP), ***Atmos. Chem. Phys.***, ***13*** (4), 2063–2090, doi:10.5194/acp-13-2063-2013, 2013.

Young, P.J., V. Naik, A.M. Fiore, A. Gaudel, J. Guo, M.Y. Lin, J.L. Neu, D.D. Parrish, H.E. Rieder, J.L. Schnell, S. Tilmes, O. Wild, L. Zhang, J.R. Ziemke, J. Brandt, A. Delcloo, R.M. Doherty, C. Geels, M.I. Hegglin, L. Hu, U. Im, R. Kumar, A. Luhar, L. Murray, D. Plummer, J. Rodriguez, A. Saiz-Lopez, M.G. Schultz, M.T. Woodhouse, and G. Zeng, Tropospheric Ozone Assessment Report: Assessment of global-scale model performance for global and regional ozone distributions, variability, and trends, ***Elementa (Wash., DC)***, ***6***, 10, doi:10.1525/elementa.265, 2018.

Yu, P., O.B. Toon, C.G. Bardeen, Y. Zhu, K.H. Rosenlof, R.W. Portmann, T.D. Thornberry, R.-S. Gao, S.M. Davis, E.T. Wolf, J. de Gouw, D.A. Peterson, M.D. Fromm, and A. Robock, Black carbon lofts wildfire smoke high into the stratosphere to form a persistent plume, ***Science***, ***365***, 587–590, doi:10.1126/science.aax1748, 2019.

Yu, P., S.M. Davis, O.B. Toon, R.W. Portmann, C.G. Bardeen, J.E. Barnes, H. Telg, C. Maloney, and K.H. Rosenlof, Persistent stratospheric warming due to 2019–2020 Australian wildfire smoke, ***Geophys. Res. Lett.***, ***48*** (7), doi:10.1029/2021gl092609, 2021.

Zawodny, J.M., and M.P. McCormick, Stratospheric Aerosol and Gas Experiment II measurements of the quasi-biennial oscillations in ozone and nitrogen dioxide, ***J. Geophys. Res.***, ***96*** (D5), 9371–9377, doi:10.1029/91jd00517, 1991.

Zeng, G., O. Morgenstern, P. Braesicke, and J.A. Pyle, Impact of stratospheric ozone recovery on tropospheric ozone and its budget, ***Geophys. Res. Lett.***, ***37*** (9), L09805, doi:10.1029/2010GL042812, 2010.

Zeng, G., O. Morgenstern, J.H.T. Williams, F.M. O'Connor, P.T. Griffiths, J. Keeble, M. Deushi, L.W. Horowitz, V. Naik, L.K. Emmons, N.L. Abraham, A.T. Archibald, S.E. Bauer, B. Hassler, M. Michou, M.J. Mills, L.T. Murray, N. Oshima, L.T. Sentman, S. Tilmes, K. Tsigaridis, and P.J. Young, Attribution of stratospheric and tropospheric ozone changes between 1850 and 2014 in CMIP6 models, ***J. Geophys. Res.***, ***127*** (16), e2022JD036452, doi:10.1029/2022JD036452, 2022.

Zerefos, C., J. Kapsomenakis, K. Eleftheratos, K. Tourpali, I. Petropavlovskikh, D. Hubert, S. Godin-Beekmann, W. Steinbrecht, S. Frith, V. Sofieva, and B. Hassler, Representativeness of single lidar stations for zonally averaged ozone profiles, their trends and attribution to proxies, ***Atmos. Chem. Phys.***, ***18***, 6427–6440, doi:10.5194/acp-18-6427-2018, 2018.

Zhang, J., W. Tian, F. Xie, M.P. Chipperfield, W. Feng, S.-W. Son, N.L. Abraham, A.T. Archibald, S. Bekki, N. Butchart, M. Deushi, S. Dhomse, Y. Han, P. Jöckel, D. Kinnison, O. Kirner, M. Michou, O. Morgenstern, F.M. O'Connor, G. Pitari, D.A. Plummer, L.E. Revell, E. Rozanov, D. Visioni, W. Wang, and G. Zeng, Stratospheric ozone loss over the Eurasian continent induced by the polar vortex shift, ***Nat. Commun.***, ***9***, 206, doi:10.1038/s41467-017-02565-2, 2018.

Zhang, J., W. Tian, F. Xie, W. Sang, D. Guo, M. Chipperfield, W. Feng, and D. Hu, Zonally asymmetric trends of winter total column ozone in the northern middle latitudes, ***Clim. Dyn.***, ***52***, 4483–4500, doi:10.1007/s00382-018-4393-y, 2019.

Zhang, Y., O.R. Cooper, A. Gaudel, A.M. Thompson, P. Nédélec, S.-Y. Ogino, and J.J. West, Tropospheric ozone change from 1980 to 2010 dominated by equatorward redistribution of emissions, ***Nat. Geosci.***, ***9***, 875–879, doi:10.1038/ngeo2827, 2016.

Zhang, Y., J.J. West, L.K. Emmons, J. Flemming, J.E. Jonson, M.T. Lund, T. Sekiya, K. Sudo, A. Gaudel, K.-L. Chang, P. Nédélec, and V. Thouret, Contributions of world regions to the global tropospheric ozone burden change from 1980 to 2010, ***Geophys. Res. Lett.***, ***48*** (1), doi:10.1029/2020gl089184, 2021.

Zhao, X., V. Fioletov, M. Brohart, V. Savastiouk, I. Abboud, A. Ogyu, J. Davies, R. Sit, S.C. Lee, A. Cede, M. Tiefengraber, M. Müller, D. Griffin, and C. McLinden, The world Brewer reference triad – updated performance assessment and new double triad, ***Atmos. Meas. Tech.***, ***14***, 2261–2283, doi:10.5194/amt-14-2261-2021, 2021.

Ziemke, J.R., S. Chandra, L.D. Oman, and P.K. Bhartia, A new ENSO index derived from satellite measurements of column ozone, ***Atmos. Chem. Phys.***, ***10***, 3711–3721, doi:10.5194/acp-10-3711-2010, 2010.

Ziemke, J.R., L.D. Oman, S.A. Strode, A.R. Douglass, M.A. Olsen, R.D. McPeters, P.K. Bhartia, L. Froidevaux, G.J. Labow, J.C. Witte, A.M. Thompson, D.P. Haffner, N.A. Kramarova, S.M. Frith, L.-K. Huang, G.R. Jaross, C.J. Seftor, M.T. Deland, and S.L. Taylor, Trends in global tropospheric ozone inferred from a composite record of TOMS/OMI/MLS/OMPS satellite measurements and the MERRA-2 GMI simulation, ***Atmos. Chem. Phys.***, ***19***, 3257–3269, doi:10.5194/acp-19-3257-2019, 2019.